

## AN ABSTRACT OF THE DISSERTATION OF

Sungwon Shin for the degree of Doctor of Philosophy in Civil Engineering  
presented on September 23, 2005.

Title: Laboratory Observations and Numerical Modeling of Inner Surf and Swash  
Zone Hydrodynamics on a Steep Slope

Abstract approved:

Redacted for privacy

---

Daniel T. Cox

Laboratory data of free surface elevations and fluid velocities were obtained using a laser-Doppler velocimeter for the case of a periodic wave plunging over an impermeable, steep (1:10) slope with a fixed bottom roughness. The measurements were conducted over 15 cross-shore locations from the outer surf zone to the swash zone with approximately 10 vertical points at each location, including the bottom boundary layer and some points above the trough level. Various hydrodynamic quantities, including the ensemble averaged turbulent kinetic energy ( $\langle k \rangle$ ) and turbulence intensities ( $\langle u'^2 \rangle$  and  $\langle w'^2 \rangle$ ), were estimated to better understand inner surf and swash zone hydrodynamics induced by strongly plunging waves. In the surf zone, the ensemble averaged horizontal fluid velocity ( $\langle u \rangle$ ) near the bottom led in phase compared to  $\langle u \rangle$  in the upper layer, and  $\langle u \rangle$  at

the bore front exceeded the theoretical wave celerity. At the impinge point, a strong return flow occurred that was greater in magnitude than the onshore directed velocity. In the surf zone,  $\langle k \rangle$  was largest just below trough level with a forward shift in phase of the peak intensity. The turbulent energy was mostly dissipated after the passage of the crest at this location.  $\langle u \rangle$  near the bottom was leading in phase with a sharp vertical gradient in  $\langle u \rangle$  indicating that boundary layer processes may have been important. In the swash zone, the vertical gradient of  $\langle u \rangle$  was relatively small compared to the vertical gradient of  $\langle u \rangle$  in the surf zone and may be due to the effect that the strong downrush had on turbulent mixing. The time-averaged estimate of turbulent kinetic energy ( $\overline{\langle k \rangle}$ ) was vertically uniform over the inner surf and swash zone.

Numerical simulations of the inner surf and swash hydrodynamics were carried out using 1D (RBREAK2 and FUNWAVE1D), 2D (COBRAS) models. All of the models accurately predicted several hydrodynamic quantities, however, they predicted that the waves broke slightly seaward of the experimental impinge point. COBRAS overpredicted the  $\langle k \rangle$  by 2~3 times in the inner surf zone but the prediction improved in the swash zone. In this study COBRAS was the most suited model to predict the hydrodynamics at the impinge point.

© Copyright by Sungwon Shin

September 23, 2005

All Rights Reserved

Laboratory Observations and Numerical Modeling of Inner Surf and Swash Zone  
Hydrodynamics on a Steep Slope

by  
Sungwon Shin

A DISSERTATION

submitted to

Oregon State University

in partial fulfillment of  
the requirements for the  
degree of

Doctor of Philosophy

Presented September 23, 2005  
Commencement June 2006

Doctor of Philosophy dissertation of Sungwon Shin presented on September 23, 2005.

APPROVED:

Redacted for privacy

---

Major Professor, representing Civil Engineering

Redacted for privacy

---

Head of the Department of Civil, Construction, and Environmental Engineering

Redacted for privacy

---

Dean of the Graduate School

I understand that my dissertation will become part of the permanent collection of Oregon State University libraries. My signature below authorizes release of my dissertation to any reader upon request.

Redacted for privacy

---

Sungwon Shin, Author

## ACKNOWLEDGEMENTS

This work was sponsored by the National Science Foundation CAREER Award CTS-9734109. The Offshore Technology Research Center at Texas A&M University also donated the laser Doppler velocimeter used in this study.

I would like to express my sincere appreciation to Dr. Daniel Cox for providing me a great opportunity to study and work with him and his support and advice.

I am thankful to Dr. Solomon Yim, Dr. Merrick Haller, Dr. Tuba Ozkan-Haller, and Dr. Ben Lee for working, advising, and encouraging me as my committee. I would also like to thank Dr. Tom Hsu, Dr. Takayuki Suzuki, and Patricio Catalan for their great help and comments on the numerical modeling conducted as part of this study. I am grateful for the help, guidance, and encouragement given to me by the staff and students at O. H. Hinsdale Wave Research Laboratory: Chris Scott, special thanks for his prayers, Tim Maddux, Linda Fayler, and Nathan Potter.

I wish to thank my grandmother, mother, and mother-in-law for their prayers. I deeply appreciate my wife, Nanjoo Lee, son, Joseph Shin, and daughter, Jamie Shin for their sacrifice, prayers, and support.

I must also thank all of my colleagues, Sangsoo Ryu, Joel Darnell, Charles Bisgard, Shingo Ichikawa, Joe Long, Wenwen Li, Jason Magalen, Gang Cao, Dongjun Yuk, Chris Chickadel, Jamie Lescinski, Eileen Crawford, Brady Richmond, Edward Wieland, and Dave Michalsen for their help and friendship through the years. I would also like to thank my friends in both Korea and United States for their love, encouragement, and prayers.

Finally, I would like to thank my Heavenly Father for always giving me love, peace, and vision. All of my work is for the glory of the Lord.

## CONTRIBUTION OF AUTHORS

Dr. Daniel T. Cox contributed to all chapters in this dissertation including the results, conclusions, and discussion. Ashok Sukumaran and Nungsoo Kim, who were the graduate students at Texas A&M University, contributed to the experimental measurements.

## TABLE OF CONTENTS

	<u>Page</u>
1 General Introduction .....	1
1.1 Literature Review.....	2
1.2 Outline of Dissertation.....	7
2 Laboratory Experiments.....	10
2.1 Experimental Setup.....	10
3 Data Analysis .....	17
3.1 Data Reduction and Ensemble Averaging .....	17
4 Turbulence in the inner surf and swash zone.....	35
4.1 Time Averaged Turbulence .....	35
4.2 Ensemble Averaged Turbulence .....	39
4.3 Discussion.....	46
5 Numerical Comparisons.....	49
5.1 One-Dimensional Model I: RBREAK2 .....	50
5.2 One-Dimensional Model II: FUNWAVE1D .....	61
5.3 Two-Dimensional Model: COBRAS .....	70
5.4 Modified Input Conditions.....	88
5.5 Discussion.....	96
6 Conclusions.....	98
Bibliography .....	101
Appedix A. Summary of LDV measurement .....	109
Appedix B. The vertical profile of the ensemble averaged free surface elevations and the fluid velocities.....	110
Appedix C. A contour plot of ensemble averaged turbulent kinetic energy and wave induced horizontal velocities .....	120
Appedix D. Three-Dimensional Model: Large Eddy Simulation.....	127
Appedix E. Numerical model inputs.....	130

## LIST OF FIGURES

<u>Figure</u>	<u>Page</u>
2.1 Sketch of wave flume and experimental setup: (a) side view; (b) plan view. WG = wave gage. LDV = Laser Doppler Velocimeter.....	11
2.2 Free surface and velocity measurements using wave gage and LDV. The upper picture shows the instrumentation and beach setup for measurement area. The lower picture shows the measurement of fluid particle velocity using LDV.....	16
3.1 Spatial variation of free surface elevation (solid line) and envelope of one standard deviation (dashed line).....	20
3.2 Cross-shore variation of wave characteristics and measurement locations: (a) mean water levels ( $\bar{\eta}$ ), crest levels ( $\eta_c$ ), and trough levels ( $\eta_t$ ). The arrow shows the first impinge point at F; (b) time averaged horizontal fluid velocities ( $\bar{u}$ ), the maximum ( $\langle u \rangle_{\max}$ ) and minimum ( $\langle u \rangle_{\min}$ ) ensemble averaged velocities near the bottom ( $z' = 0.00 - 0.40$ cm); (c) coordinate system and measurement locations of the wave gage and LDV.....	21
3.3 The spectra of free surface elevation at all cross-shore locations.....	22
3.4 Example of measured velocity and calculated turbulent quantities at E ( $z' = 1.6$ cm). Bold lines are the ensemble averaged quantities and thin lines are the instantaneous quantities.....	27
3.5 The vertical profile of the ensemble averaged horizontal and vertical fluid particle velocities ( $\langle u \rangle$ and $\langle w \rangle$ ) at A. Solid lines are $\langle u \rangle$ and dashed lines are $\langle w \rangle$ .....	29

LIST OF FIGURES (Continued)

<u>Figure</u>	<u>Page</u>
3.6 The vertical profile of the ensemble averaged horizontal and vertical fluid particle velocities ( $\langle u \rangle$ and $\langle w \rangle$ ) at E. Solid lines are $\langle u \rangle$ and dashed lines are $\langle w \rangle$ .....	30
3.7 The vertical profile of the ensemble averaged horizontal and vertical fluid particle velocities ( $\langle u \rangle$ and $\langle w \rangle$ ) at I2. Solid lines are $\langle u \rangle$ and dashed lines are $\langle w \rangle$ .....	31
3.8 Contour plots of ensemble averaged wave induced horizontal velocities (cm/s) and free surface elevations (envelopes) at E, F, and G. $z^*$ is normalized water depth ( $z^* = z' / h$ ).....	33
3.9 Contour plots of ensemble averaged wave induced horizontal velocities (cm/s) and free surface elevations (envelopes) at H, H2, and I. $z^*$ is normalized water depth ( $z^* = z' / h$ ).....	34
4.1 The vertical structure of the ratio of $\overline{u'^2}$ to $\overline{w'^2}$ along the cross-shore measurement locations. At E, $\overline{u'^2} / \overline{w'^2}$ is 1.69 at $z' = 1.60$ cm and 1.30 at $z' = 3.60$ cm.....	37
4.2 The vertical structures of $\overline{\langle k \rangle}$ in the inner surf and swash zone.....	38
4.3 A contour plot of ensemble averaged turbulent kinetic energy $\langle k \rangle$ in $\text{cm}^2/\text{s}^2$ (a) and wave induced horizontal velocities $\langle u \rangle$ (b) at E. In (b), solid line is the wave velocity at $z' = 0.10$ cm ( $z^* = 0.013$ , shown by the heavy solid line in (a)) and dashed line is at $z' = 1.60$ cm ( $z^* = 0.202$ , shown by the heavy dashed line in (a)).....	43

LIST OF FIGURES (Continued)

<u>Figure</u>	<u>Page</u>
<p>4.4 A contour plot of ensemble averaged turbulent kinetic energy <math>\langle k \rangle</math> in <math>\text{cm}^2/\text{s}^2</math> (a) and wave induced horizontal velocities <math>\langle u \rangle</math> (b) at I2. In (b), solid line is the wave velocity at <math>z' = 0.05</math> cm (<math>z^* = 0.023</math>, shown by the heavy solid line in (a)) and dashed line is at <math>z' = 0.40</math> cm (<math>z^* = 0.187</math>, shown by the heavy dashed line in (a)).....</p>	44
<p>4.5 Cross-shore variations of hydrodynamic quantities near the bottom (averaged 0 – 0.4 cm). (a) <math>H</math> (<math>\bullet</math>) and <math>\bar{\eta}</math> (<math>\square</math>); (b) time averaged horizontal velocity, i.e. undertow (<math>\langle \bar{u} \rangle</math>, cm/s) near the bottom; (c) skewness of <math>\langle u \rangle</math> (<math>\Delta</math>) and <math>\eta</math> (<math>\blacktriangle</math>); (d) asymmetry of <math>\langle u \rangle</math> (<math>\Delta</math>) and <math>\eta</math> (<math>\blacktriangle</math>); (e) <math>\langle \bar{k} \rangle</math> near the bottom (<math>z' &lt; 4</math> mm). Open circles were specified in the text.....</p>	45
<p>5.1 Comparisons of the free surface elevations calculated using RBREAK2 with the measured data from A to G. Solid lines are the measured data. Dashed lines are the simulated data.....</p>	54
<p>5.2 Comparisons of the free surface elevations calculated using RBREAK2 with the measured data from H to M. Solid lines are the measured data. Dashed lines are the simulated data.....</p>	55
<p>5.3 Comparisons of the free surface elevation spectra calculated using RBREAK2 with the experimental data. Solid lines are the spectra estimated from the experiments. Dashed lines are the spectra estimated from the RBREAK2.....</p>	56

## LIST OF FIGURES (Continued)

<u>Figure</u>	<u>Page</u>
<p>5.4 Comparisons of the wave height variation (circles) and setup (triangles) (a) and undertow (<math>\langle u \rangle_{\text{mean}}</math>) near the bottom (squares) and depth-averaged undertow (triangles, below the trough level) (b). Solid symbols are the measured data. Open symbols are the RBREAK2 results.....</p>	57
<p>5.5 Comparisons of the mean, maximum, and minimum ensemble averaged horizontal fluid velocities calculated using RBREAK2 with the experimental data at each cross-shore location. Open symbols are the measured data. Solid symbols are the RBREAK2 results. Dashed line represents the trough level.....</p>	59
<p>5.6 Comparison of the skewness and asymmetry of the free surface elevation and ensemble averaged horizontal fluid velocities near the bottom computed using RBREAK2 with the experimental data. Solid symbols are the measured data. Open symbols are the RBREAK2 results. S( ) denotes skewness and A( ) denotes asymmetry.....</p>	60
<p>5.7 Comparison of the free surface elevations calculated by FUNWAVE1D with the measured data from A to G. Solid lines are the measured data. Dashed lines are the simulated data.....</p>	64
<p>5.8 Comparison of the free surface elevations calculated by FUNWAVE1D with the measured data from H to L. Solid lines are the measured data. Dashed lines are the simulated data.....</p>	65
<p>5.9 Comparison of the free surface elevation spectra with the experimental data. Solid lines are the spectra estimated from the experiment. Dashed lines are the FUNWAVE1D results.....</p>	66

## LIST OF FIGURES (Continued)

<u>Figure</u>	<u>Page</u>
5.10 Comparison of the wave height variation (circles) and setup (triangles) (a), and undertow near the bottom (squares) and depth-averaged undertow (triangles, below the trough level) (b). Black colored symbols are the measured data. Solid symbols are the measured data. Open symbols are the FUNWAVE1D results.....	67
5.11 Comparison of the mean, maximum, and minimum ensemble averaged horizontal fluid velocities with the experimental data at each cross-shore location. Open symbols are the measured data. Solid symbols are the FUNWAVE1D results.....	68
5.12 Comparison of the skewness and asymmetry of the free surface elevation and ensemble averaged horizontal fluid velocities near the bottom. Solid symbols are the measured data. Open symbols are the FUNWAVE1D results. $S( )$ denotes skewness and $A( )$ denotes asymmetry.....	69
5.13 Simulation of vector field and TKE contour using COBRAS with the nonlinear eddy viscosity model at several time steps.....	74
5.14 Comparison of the free surface elevations calculated using COBRAS (nonlinear eddy viscosity model) with the measured data from A to G. Solid lines are the measured data. Dashed lines are the simulated data.....	75
5.15 Comparison of the free surface elevations calculated using COBRAS (nonlinear eddy viscosity model) with the measured data from H to L. Solid lines are the measured data. Dashed lines are the simulated data.....	76
5.16 Comparison of the free surface elevations calculated using COBRAS (RNG model) with the measured data from A to G. Solid lines are the measured data. Dashed lines are the simulated data.....	77

## LIST OF FIGURES (Continued)

<u>Figure</u>	<u>Page</u>
5.17 Comparison of the free surface elevations calculated using COBRAS (RNG model) with the measured data from H to L. Solid lines are the measured data. Dashed lines are the simulated data.....	78
5.18 Comparison of the free surface elevation spectra with the experimental data. Solid lines are the spectra estimated from the experiment. Dashed lines are the COBRAS results using the nonlinear eddy viscosity model. Dash-dot lines are the COBRAS results using the RNG model.....	79
5.19 Comparison of the variation of the wave height (solid) (a) and setup (open) (b), and undertow (solid circles: the experimental data; open squares: nonlinear eddy viscosity model; open triangle: RNG model) near the bottom (c) calculated using COBRAS with the measured data. Circles are the experimental data. Squares are from the nonlinear eddy viscosity model. Triangles are from the RNG model.....	80
5.20 Comparison of the skewness and asymmetry of the free surface elevation and ensemble averaged horizontal fluid velocities near the bottom. Solid symbols are the measured data. Open symbols are the COBRAS results. S( ) denotes skewness and A( ) denotes asymmetry. Circles are the experimental results. Squares are from the nonlinear eddy viscosity model. Triangles are from the RNG model.....	84
5.21 Comparison of the mean, maximum, and minimum ensemble averaged horizontal fluid velocities with the experimental data at each cross-shore location. Open symbols are the measured data. Solid and dashed lines are the COBREAS using the nonlinear eddy viscosity model results.....	85

## LIST OF FIGURES (Continued)

<u>Figure</u>	<u>Page</u>
5.22 Comparison of the mean, maximum, and minimum ensemble averaged horizontal fluid velocities with the experimental data at each cross-shore location. Open symbols are the measured data. Solid and dashed lines are the COBREAS using the RNG model results.....	86
5.23 The cross-shore variation of the turbulent kinetic energy. Filled circles are the experimental data. Squares are the results with nonlinear eddy viscosity model). Triangles are the results with the RNG model.....	87
5.24 Wave reflection coefficients for slopes, beaches, and rubble-mound breakwaters as a function of the surf similarity parameter (Shore Protection Manual, 2-118). $H_i$ is the incident wave height. $L_0$ is the deep water wave length. The y axis is the reflection coefficient.....	90
5.25 Sketch of the modified input conditions.....	91
5.26 Comparison of the wave height variation (a), and setup (b), and undertow near the bottom (c) using the modified input conditions. Filled circles are the experimental data. Open squares are the RBREAK2 results. Triangles are the FUNWAVE1D results. Inverse triangles are the COBRAS results with the RNG model. Asterisks are the COBRAS results with the nonlinear eddy viscosity model.....	93
5.27 Comparison of the skewness and asymmetry of the free surface elevation and ensemble averaged horizontal fluid velocities near the bottom. Filled circles are the experimental data. Open squares are the RBREAK2 results. Triangles are the FUNWAVE1D results. Inverse triangles are the COBRAS results with the RNG model. Asterisks are the COBRAS results with the nonlinear eddy viscosity model. $S()$ denotes skewness and $A()$ denotes asymmetry.....	94

## LIST OF FIGURES (Continued)

<u>Figure</u>	<u>Page</u>
5.28 The cross-shore variation of the turbulent kinetic energy. Solid circles are the experimental data. Squares are the results from COBRAS using the nonlinear eddy viscosity model. Triangles are the results from COBRAS using the RNG model.....	95
B.1 The vertical profile of the ensemble averaged horizontal and vertical fluid particle velocities ( $\langle u \rangle$ and $\langle w \rangle$ ) at B. Solid lines are $\langle u \rangle$ and dashed lines are $\langle w \rangle$ .....	110
B.2 The vertical profile of the ensemble averaged horizontal and vertical fluid particle velocities ( $\langle u \rangle$ and $\langle w \rangle$ ) at C. Solid lines are $\langle u \rangle$ and dashed lines are $\langle w \rangle$ .....	111
B.3 The vertical profile of the ensemble averaged horizontal and vertical fluid particle velocities ( $\langle u \rangle$ and $\langle w \rangle$ ) at D. Solid lines are $\langle u \rangle$ and dashed lines are $\langle w \rangle$ .....	112
B.4 The vertical profile of the ensemble averaged horizontal and vertical fluid particle velocities ( $\langle u \rangle$ and $\langle w \rangle$ ) at F. Solid lines are $\langle u \rangle$ and dashed lines are $\langle w \rangle$ .....	113
B.5 The vertical profile of the ensemble averaged horizontal and vertical fluid particle velocities ( $\langle u \rangle$ and $\langle w \rangle$ ) at G. Solid lines are $\langle u \rangle$ and dashed lines are $\langle w \rangle$ .....	114
B.6 The vertical profile of the ensemble averaged horizontal and vertical fluid particle velocities ( $\langle u \rangle$ and $\langle w \rangle$ ) at H. Solid lines are $\langle u \rangle$ and dashed lines are $\langle w \rangle$ .....	115

LIST OF FIGURES (Continued)

<u>Figure</u>	<u>Page</u>
B.7 The vertical profile of the ensemble averaged horizontal and vertical fluid particle velocities ( $\langle u \rangle$ and $\langle w \rangle$ ) at H2. Solid lines are $\langle u \rangle$ and dashed lines are $\langle w \rangle$ .....	116
B.8 The vertical profile of the ensemble averaged horizontal and vertical fluid particle velocities ( $\langle u \rangle$ and $\langle w \rangle$ ) at I. Solid lines are $\langle u \rangle$ and dashed lines are $\langle w \rangle$ .....	117
B.9 The vertical profile of the ensemble averaged horizontal and vertical fluid particle velocities ( $\langle u \rangle$ and $\langle w \rangle$ ) at K. Solid lines are $\langle u \rangle$ and dashed lines are $\langle w \rangle$ .....	118
B.10 The vertical profile of the ensemble averaged horizontal and vertical fluid particle velocities ( $\langle u \rangle$ and $\langle w \rangle$ ) at D. Solid lines are $\langle u \rangle$ and dashed lines are $\langle w \rangle$ .....	119
C.1 A contour plot of ensemble averaged turbulent kinetic energy $\langle k \rangle$ in $\text{cm}^2/\text{s}^2$ (a) and wave induced horizontal velocities $\langle u \rangle$ (b) at C. In (b), solid line is the wave velocity at $z' = 0.10$ cm, shown by the heavy solid line in (a), and dashed line is at $z' = 1.60$ cm, shown by the heavy dashed line in (a).....	120
C.2 A contour plot of ensemble averaged turbulent kinetic energy $\langle k \rangle$ in $\text{cm}^2/\text{s}^2$ (a) and wave induced horizontal velocities $\langle u \rangle$ (b) at D. In (b), solid line is the wave velocity at $z' = 0.10$ cm, shown by the heavy solid line in (a), and dashed line is at $z' = 1.60$ cm, shown by the heavy dashed line in (a).....	121

LIST OF FIGURES (Continued)

<u>Figure</u>	<u>Page</u>
C.3 A contour plot of ensemble averaged turbulent kinetic energy $\langle k \rangle$ in $\text{cm}^2/\text{s}^2$ (a) and wave induced horizontal velocities $\langle u \rangle$ (b) at F. In (b), solid line is the wave velocity at $z' = 0.10$ cm, shown by the heavy solid line in (a), and dashed line is at $z' = 1.60$ cm, shown by the heavy dashed line in (a).....	122
C.4 A contour plot of ensemble averaged turbulent kinetic energy $\langle k \rangle$ in $\text{cm}^2/\text{s}^2$ (a) and wave induced horizontal velocities $\langle u \rangle$ (b) at G. In (b), solid line is the wave velocity at $z' = 0.10$ cm, shown by the heavy solid line in (a), and dashed line is at $z' = 1.60$ cm, shown by the heavy dashed line in (a).....	123
C.5 A contour plot of ensemble averaged turbulent kinetic energy $\langle k \rangle$ in $\text{cm}^2/\text{s}^2$ (a) and wave induced horizontal velocities $\langle u \rangle$ (b) at H. In (b), solid line is the wave velocity at $z' = 0.10$ cm, shown by the heavy solid line in (a), and dashed line is at $z' = 0.40$ cm, shown by the heavy dashed line in (a).....	124
C.6 A contour plot of ensemble averaged turbulent kinetic energy $\langle k \rangle$ in $\text{cm}^2/\text{s}^2$ (a) and wave induced horizontal velocities $\langle u \rangle$ (b) at H2. In (b), solid line is the wave velocity at $z' = 0.10$ cm, shown by the heavy solid line in (a), and dashed line is at $z' = 0.40$ cm, shown by the heavy dashed line in (a).....	125
C.7 A contour plot of ensemble averaged turbulent kinetic energy $\langle k \rangle$ in $\text{cm}^2/\text{s}^2$ (a) and wave induced horizontal velocities $\langle u \rangle$ (b) at I. In (b), solid line is the wave velocity at $z' = 0.10$ cm, shown by the heavy solid line in (a), and dashed line is at $z' = 0.40$ cm, shown by the heavy dashed line in (a).....	126
D.1 Vector field simulated using the LES model (Yokohama Univ.) at several time steps.....	129

## LIST OF TABLES

<u>Table</u>	<u>Page</u>
1.1 The comparison between the present study and the previous field and laboratory studies. $\eta$ is free surface elevation. $u$ , $v$ , and $w$ is horizontal and vertical fluid particle velocities. $\tau_b$ is bottom shear stress. SSC is the suspended sediment concentration. TKE is turbulent kinetic energy. $\varepsilon$ is turbulent dissipation rate.....	9
2.1 Characteristic wave conditions. $H_{ref}$ is the reference wave height observed on the flat bottom; $H_0$ is deep water wave height; $H_b$ is breaking wave height; $h_b$ is the water depth of wave breaking; $X_s$ is surf zone width; $\xi_b$ is surf similarity parameter. ....	13
3.1 Free surface elevation and near bottom velocity measurements at each location. $u$ is reported considering only near bottom elevations ( $z' = 0.00 - 0.40$ cm). $C$ is estimated $C = \sqrt{g(h + \eta_c)}$ .....	19
4.1 Relative turbulent intensities of $\overline{u'^2}$ and $\overline{w'^2}$ normalized by $2\overline{k}$ , and their ratio (Svendsen, 1987).....	36
5.1 $r^2$ values between the experimental results and the numerical model results. ....	83
A.1 Summary of elevations (cm from the bottom) for LV measurements (Sukumaran, 2000).....	109

# Laboratory Observations and Numerical Modeling of Inner Surf and Swash Zone Hydrodynamics on a Steep Slope

## 1 General Introduction

The swash zone is defined as the area of the nearshore that is wet and dry due to wave runup and rundown. The swash zone is important because it is the land-sea boundary where coastal erosion and accretion occur. The dominant physical processes in the swash zone include infiltration-exfiltration (Turner and Masselink, 1998; Butt *et al.*, 2001), hydraulic jump (Osborne and Rooker, 1999), and bore generated turbulence (Puleo *et al.*, 2000). Moreover, the fluid velocities and sediment concentrations can be higher in the inner surf and swash zone than seaward of this region. Additionally, the sediment concentrations in the swash zone are several orders of magnitude larger than those in the inner surf zone (Osborne and Rooker, 1999; Beach and Sterberg, 1991). The sediment dynamics and transport in this region are governed by swash hydrodynamics (Elfrink and Baldock, 2002).

It has been proposed that bore generated turbulence is dominant during the uprush phase and boundary generated turbulence is dominant during the downrush phase (Puleo *et al.*, 2000; Petti and Longo, 2001; Cowen *et al.*, 2003). Puleo *et al.* (2000) suggested that bore generated turbulence cannot be ignored in the study of

swash zone sediment transport. Butt *et al.* (2004) found that bore generated turbulence may affect on sediment transport mechanisms, especially the relationship between turbulent kinetic energy (TKE) and the suspended sediment concentration. Sediment transport mechanisms in the swash zone have received less attention compared to those in the surf zone, due to the difficulties in both field observations and laboratory measurements. The transient nature of the flow, thinness of the runup tongue, and the entrainment of air and sediment are some of factors that increase measurement difficulties (e.g., Raubenheimer *et al.*, 2004).

## 1.1 Literature Review

Several field studies of swash zone hydrodynamics have been performed. Butt and Russell (1999) measured cross-shore fluid velocities and sediment concentrations and showed that onshore and offshore sediment transport mechanisms are related to the velocity skewness and asymmetry. Similarly, using cross-shore velocity and water depth to determine a relationship between bore generated turbulent energy dissipation and sediment transport, Puleo *et al.* (2000) suggested that in the swash zone, bore generated turbulent motions reach the bottom there by effecting sediment suspension. Holland *et al.* (2001) developed a particle image velocimetry (PIV) system to observe the structure of swash flow in plan view using the bore image intensity. Raubenheimer (2002) observed cross-

shore fluid velocities, at Scripps Beach, a gently sloping, sandy beach and modeled this with the nonlinear shallow water equations. Using these data, Raubenheimer *et al.* (2004) estimated turbulence production, dissipation, and bottom friction coefficients. Butt *et al.* (2004) measured cross-shore fluid velocities and sediment concentrations using 3-dimensional acoustic-Doppler velocimeters and optical backscatterer sensors on a steep beach. The bore front had high suspended sediment concentrations and high TKE values, suggesting the importance of bore-generated turbulence in the suspension of sediment in the swash zone.

Laboratory measurements of swash zone hydrodynamics have also been conducted (e.g., Cox *et al.*, 2001; Petti and Longo, 2001; Archetti and Brocchini, 2002; Cowen *et al.*, 2003). Cox *et al.* (2001) used a laser-Doppler velocimeter (LDV) to measure the fluid velocities, including turbulence, within the boundary layer. They estimated the bottom friction coefficient and the bed stress at the rough, fixed bottom for a random wave case in the inner surf and swash zone. The results showed that the averaged absolute value of the bed stress was largest below the still water shoreline and was larger above the still water shoreline than in the surf zone. Petti and Longo (2001) measured fluid velocities using an LDV and estimated the bore generated turbulence and bottom friction coefficients in the swash zone. Alternately, Cowen *et al.* (2003) measured swash zone fluid velocity fields using a PIV technique to estimate bore generated turbulence and bottom friction. The laboratory studies of Petti and Longo (2001) and Cowen *et al.* (2003)

showed that the vertical structure of cross-shore wave induced velocities had a logarithmic boundary layer with friction coefficients ranging from 0.02 to 0.05. Cowen *et al.* (2003) found two distinct inertial subranges of the velocity spectra similar to the results of Petti and Longo (2001) and hypothesized that those two subranges were from the bore generated turbulence during uprush and the boundary generated turbulence during downrush. Unfortunately, these results have not been confirmed through field measurements. Butt and Russell (1999) were only able to conclude that bore-generated turbulence was dominant during uprush. Raubenheimer *et al.* (2004) observed only a single inertial subrange unlike the laboratory studies of Petti and Longo (2001) and Cowen *et al.* (2003).

The previously described laboratory studies were typically conducted using fairly mild slopes with spilling breakers. This was necessary in some cases to minimize effects of air entrainment on the imaging techniques. Table 1.1 compares the present study with the previous laboratory and field studies mentioned above.

The modeling of hydrodynamics and sediment transport in the inner surf and swash zone has been challenging. The energetic basis models proposed by Bagnold (1963, 1966), which consider the free stream velocity, bottom slope, sediment characteristics and bottom friction factor, have been further developed (Hughes *et al.*, 1997; Masselink and Hughes, 1998; Puleo *et al.*, 2000).

The numerical model RBREAK, developed by Wurjanto and Kobayashi (1991), is based on the depth-averaged nonlinear shallow water equations with bottom friction on the impermeable structures and beaches. Raubenheimer (2002) used this model to compare numerical data to field data observed at Scripps Beach. The model predicted orbital velocities and nonlinear characteristics well but overpredicted swash zone velocity skewness, sea swell asymmetry, and the ratio of maximum uprush velocity to maximum downwash velocity. Cox *et al.* (1994) used RBREAK2, an expanded version of RBREAK, to compare predicted free surface elevations in the surf and swash zone to those observed on the sandy beach during the SUPERTANK laboratory data collection project.

Since the models based on the nonlinear shallow water equations do not allow frequency dispersion, these models are restricted to the shallow water, i.e. inner surf and swash zone. In contrast to the nonlinear shallow water equations, the models based on the Boussinesq equations include frequency dispersion and can be applied to non-breaking waves. However, due to the lack of dissipation by wave breaking and bottom friction, the original Boussinesq equations are not valid for the surf zone. Therefore, the models based on the Boussinesq equations have been modified to cover the surf zone by including an eddy viscosity term in the depth-integrated momentum equation to consider the energy dissipation due to wave breaking. FUNWAVE developed by Kirby *et al.* (1998) uses this eddy viscosity approach. Schäffer *et al.* (1993) adopted a different approach including a surface

roller effect to consider excess mass transport, which is balanced by the undertow. Long *et al.* (2004) extended FUNWAVE based on the approach proposed by Schäffer *et al.* (1993) to investigate cross-shore sediment transport. The model simulated well an onshore sand bar migration event observed during the DUCK94 field experiment.

Computational Fluid Dynamics (CFD) techniques have been also used to model the surf and swash zone (2D and 3D simulations). Lin and Liu (1998a,b) and Bradford (2000) applied two-dimensional Reynolds Averaged Navier-Stokes (RANS) equations with a  $k - \varepsilon$  turbulence closure to predict these surf zone hydrodynamics. These  $k - \varepsilon$  turbulence models overpredicted turbulent properties by two or three times when compared to measured data in the surf zone. Bradford (2000) applied the Renormalized Group (RNG) extension of  $k - \varepsilon$  model and slightly reduced the degree of the overestimation of turbulence compared with conventional  $k - \varepsilon$  model. Puleo *et al.* (2002) used RIPPLE, which is based on RANS equations, and RBREAK2 to compare the swash hydrodynamic quantities with those measured in the Large-Scale Sediment Transport Facility at the Army Corps of Engineers Coastal Hydraulics Laboratory. Both models accurately predicted the free surface elevation across the inner surf zone but overpredicted velocities during the passage of bore. They suggested that the 2D model (RIPPLE) may improve the prediction of the boundary layer structure and bottom shear stress.

Other work that applied CFD techniques to the swash zone was based on Navier-Stokes Solvers. Using this approach, Christensen and Deigaard (2001) developed a three-dimensional large eddy simulation (LES) model to resolve the characteristics of hydrodynamics and sediment transport in the surf and swash zone. The model simulates large turbulent structures directly and uses a subgrid scale model (SGS) for small scale turbulence. However, the model requires a very long computational time and a fine grid to predict the details of swash zone hydrodynamics.

## 1.2 Outline of Dissertation

In the present study, laboratory measurements of the free surface elevation and cross-shore and vertical fluid velocities were conducted from the outer surf zone to the swash zone using wave gages and an LDV, respectively. In this study the wave height and bottom slope were increased, resulting in a strongly plunging breaker when compared to previous studies. The objectives of the present study are to provide a synoptic, precise data set of horizontal and vertical velocities including measurements in the bottom boundary layer ( $\Delta z = O(\text{mm})$ ) under controlled conditions to estimate the vertical and cross-shore structure of turbulent intensity and kinetic energy. We also investigate the phase lag on the rough bottom in a turbulent boundary layer with a stronger plunging breaker than previous laboratory studies (Petti and Longo, 2001; Cowen, 2003). This work has been

submitted for publication (Shin and Cox, 2005). This data set is also useful to estimate the bottom shear stress using the friction velocity, turbulence production and dissipation, and to calibrate friction coefficients for numerical models (to be presented in future work) similar to the work of Cox *et al.* (2001). This dissertation focused on the measurements and numerical modeling of the free surface and fluid velocities, and the estimates of turbulent intensity and kinetic energy with fine vertical structure at each cross-shore location. The estimates of bottom shear stress and model calibration is to be in the future work. Chapter 2 shows the experimental setup, which includes wave generation and instrumentation for free surface elevation and fluid velocity measurements. Chapter 3 describes the data reduction followed by the experimental results presented in Chapter 4. Chapter 5 discusses the simulation of the experimental results using numerical models. Finally, Chapter 6 presents the summary and the main conclusion of the present study and the possible future work.

Table 1.1 The comparison between the present study and the previous field and laboratory studies.  $\eta$  is free surface elevation.  $u$ ,  $v$ , and  $w$  is horizontal and vertical fluid particle velocities.  $\tau_b$  is bottom shear stress. SSC is the suspended sediment concentration. TKE is turbulent kinetic energy.  $\varepsilon$  is turbulent dissipation rate.

	Lab /Field	Condition	$\xi_0 (\xi_b)$	Measurements
Cox <i>et al.</i> , 2000	Lab	Plunging breaker, Random waves, $d_{50} = 6.3$ mm	1.59 (1.49)	$\eta$ , $u$ , $w$ , $\tau_b$
Puleo <i>et al.</i> , 2000	Field	Random waves	0.79	$\eta$ , $u$ , SSC
Petti and Longo, 2001	Lab	Plunging breaker, Smooth bottom	1.32~1.72	$\eta$ , $u$ , turbulent energy flux, macro & micro scale TKE
Raubenheimer, 2002 & Raubenheimer, <i>et al.</i> , 2004	Field	Random waves $d_{mean} = 0.2$ mm	0.29	$\eta$ , $u$ , $v$ , $w$ , TKE, $\tau_b$ , production and $\varepsilon$
Cowen, <i>et al.</i> , 2003	Lab	Spilling & plunging breaker, Smooth bottom	0.82	$\eta$ , $u$ , $w$ , TKE, $\tau_b$ , production & $\varepsilon$
Butt <i>et al.</i> , 2004	Field	Random waves	0.82 (0.75)	$\eta$ , $u$ , $v$ , $w$ , TKE, SSC
Shin & Cox, 2005	Lab	Plunging breaker, $d_{50} = 2.2$ mm	0.72 (0.63)	$\eta$ , $u$ , $w$ , TKE

## 2 Laboratory Experiments

### 2.1 Experimental Setup

The experiment was conducted in the Civil Engineering Laboratory at Texas A&M University in a 35 m long, 0.90 m wide and 1.2 m high glass-walled wave flume by Sukumaran as a part of his Master's thesis (2000). The wave flume is equipped with a flap-type wavemaker, controlled by a personal computer, with the ability to generate repeatable regular and irregular waves.

The beach profile consisted of a 1:35 slope, which started 11.58 m from the wavemaker (preceded by a constant depth offshore) followed by a slope break and steepened foreshore (1:10 slope). The 1:10 slope began 24.42 m from the wavemaker (12.84 m from the start of the 1:35 slope) as shown in Figure 2.1. The flume was filled with fresh water, and the water depth in the flat bottom section was 0.60 m. The still water shoreline was observed to be 26.71 m from the wavemaker.

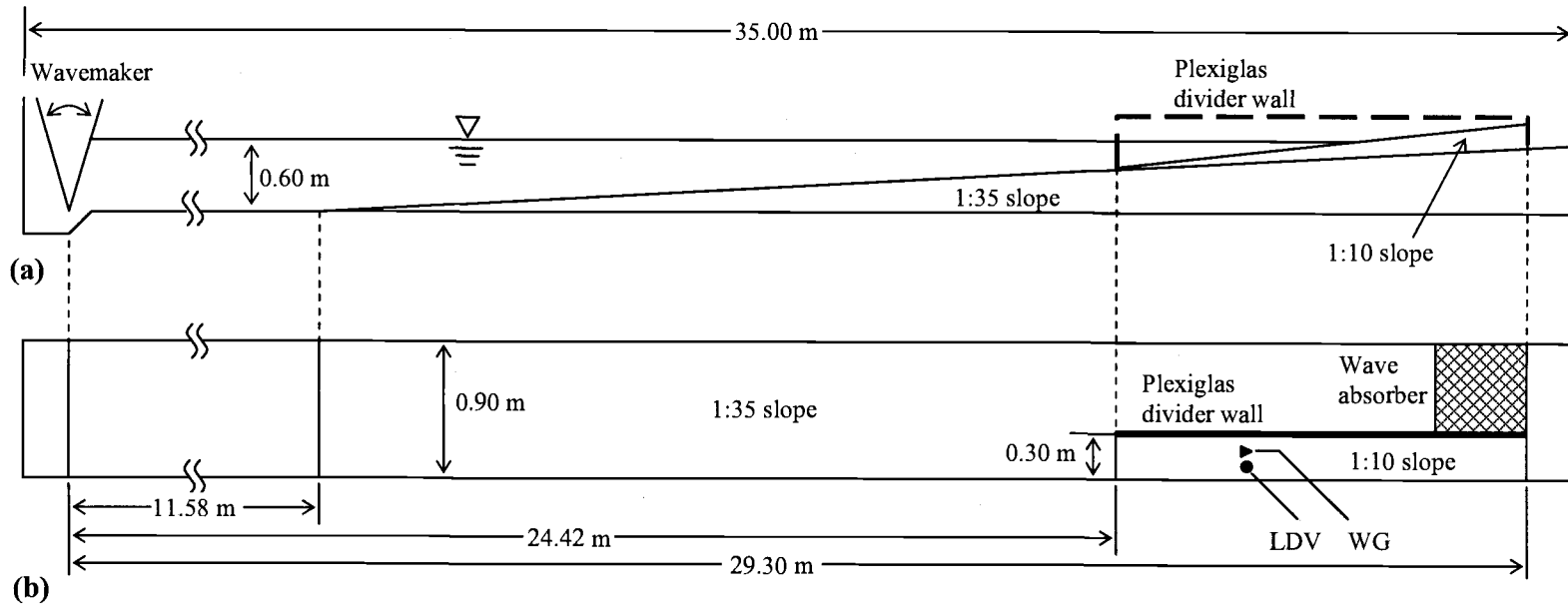


Figure 2.1 Sketch of wave flume and experimental setup: (a) side view; (b) plan view. WG = wave gage. LDV = Laser Doppler Velocimeter.

A divider wall made of Plexiglas was installed at the start of the 1:10 slope to constrain the area of study to 0.30 m of the flume width. This was done to reduce material requirements for the model beach. A fixed slope was constructed using sand grains attached to one-eighth inch Plexiglas sheets using a marine epoxy resin similar to the work of Cox *et al.* (1996). The thickness of the physical roughness above the Plexiglas was the height of one grain with a nominal diameter of 2.2 mm. This roughened bed was designed to provide a boundary layer larger than that produced over a smooth slope for the purpose of studying bottom friction. This work is to be covered elsewhere, and the present paper focuses on the hydrodynamics in the inner surf and swash zone. Horsehair was used for wave absorption at the end of the slope to minimize the effect of reflected waves from the end of the tank. Figure 2.1 shows the side and plan view of the experimental design and the measurement locations.

A time series of regular waves with 2.0 second period was generated in this study. The reference wave height was 11.38 cm at 11.32 m (flat bottom) from the wavemaker. The wave time series was repeated and measurements of free surface elevations and horizontal and vertical velocities were made at different locations along the beach profile. Table 2.1 shows the wave characteristics including surf similarity parameter, (e.g., Battjes, 1974)

$$\xi_b = \frac{\tan \alpha_b}{\sqrt{H_b/L_0}} \quad (2.1)$$

where  $\tan \alpha_b$  is the bottom slope at breaking,  $H_b$  is the breaking wave height, and  $L_0$  the deepwater wavelength as defined by linear wave theory. In this study,  $\xi_b$  was 0.63, consistent with a plunging wave breaker type.

The total length of the time series was 1800 s, and the waves were run for 300 s prior to the collection of any data. There was a waiting time of 600 s between runs to allow quasi-steady state conditions to be attained in the wave flume before measurements were made.

Table 2.1 Characteristic wave conditions.  $H_{ref}$  is the reference wave height observed on the flat bottom;  $H_0$  is deep water wave height;  $H_b$  is breaking wave height;  $h_b$  is the water depth of wave breaking;  $X_s$  is surf zone width;  $\xi_b$  is surf similarity parameter.

$T$ (s)	$H_{ref}$ (cm)	$H_0$ (cm)	$H_b$ (cm)	$h_b$ (cm)	$X_s$ (m)	$\xi_b$
2.00	11.38	12.16	15.67	12.10	1.21	0.63

### 2.3 Procedure

Measurements of the free surface elevation along the 1:10 slope were performed using a wire resistance wave gage with a 50 Hz sampling rate. A gage was placed at approximately 20 cm intervals along the 1:10 slope and at other locations where there were sharp gradients in the wave height due to breaking. The coordinate system was  $x$  positive onshore, with  $x = 0$  at the wavemaker and  $z$  positive up with  $z = 0$  at the still water level (SWL). The toe of the 1:35 slope began at  $x = 11.58$  m at a depth of  $z = -0.60$  m, and the toe of the 1:10 slope began at  $x = 24.42$  m, and at a depth of  $z = -0.17$  m. A rotated coordinate system was used for the measuring elevations on the steepened foreshore denoted by  $x'$  and  $z'$  with the origin at the toe of the 1:10 slope, to be shown in Figure 3.2 (c). The vertical coordinate  $z'$  is positive upward, normal to the 1:10 slope, with  $z' = 0$  defined as the bed level (on the Plexiglas sheet). The coordinate  $x'$  denotes the plane orthogonal to  $z'$ , positive up the 1:10 slope, with  $x' = 0$  defined as the toe of the 1:10 slope at  $x = 24.42$  m.

Figure 2.2 shows the instrumentation and beach setup for the present study. The bottom velocities inside the swash zone were measured accurately using a laser-Doppler velocimeter (LDV). The two-component, fiber optic LDV was used to measure the instantaneous vertical and horizontal velocities near the impermeable bed.

Due to the difficulty of obtaining measurements of near bottom velocities, high precision was required to position the measuring volume of the laser beams in the boundary layer. The LDV was mounted on a 3-D traverse mechanism with a rated precision of  $\pm 12.5 \mu\text{m}$ . The entire traverse was tilted by 5.7 degrees from the horizontal so that the lateral movement of the traverse would be along the 1:10 slope and the vertical movement normal to the slope. The LDV lens was also rotated 45 degrees in the  $x' - z'$  plane to measure velocities along the rotated plane. This setup was required for better positioning of the laser measuring the volume at the surface of the roughness layer. As the traverse was moved up the slope, care was taken throughout the tests to ensure that the measuring volume remained approximately 0.08 to 0.10 m from the flume wall. This was about halfway to the location of the free surface measurements, which were taken along the centerline of the 1:10 slope ( $\sim 0.15$  m).

Measurements of horizontal and vertical velocities were taken at various points in the water column for each cross-shore location along the impermeable beach, as shown in Figure 3.2 and Table 3.1. No LDV measurements were made at cross-shore location J because the LDV was obstructed by the steel frame support of the wave flume. The velocities were measured at elevations of  $z' = 0.0, 0.5, 1.0, 2.0, 4.0, 8.0, 16.0$  mm at all cross-shore locations. The flow was seeded using silver hollow spheres to increase backscattering signal intensity.

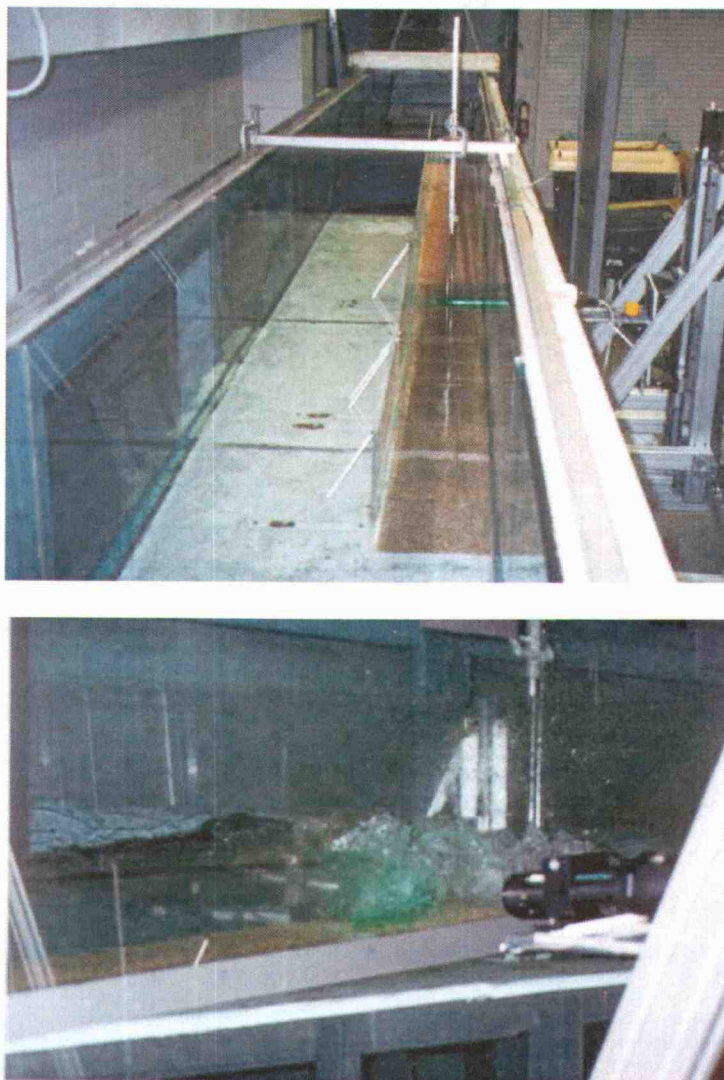


Figure 2.2 Free surface and velocity measurements using wave gage and LDV. The upper picture shows the instrumentation and beach setup for measurement area. The lower picture shows the measurement of fluid particle velocity using LDV.

### 3 Data Analysis

#### 3.1 Data Reduction and Ensemble Averaging

An ensemble averaging method was used for the reduction of the experimental free surface elevation records. This method is commonly employed for the data from repeatable, regular waves. Approximately 100 waves were averaged at each of the 14 cross-shore locations. Figure 3.1 shows the cross-shore variation of the ensemble averaged free surface elevation  $\langle \eta \rangle$  and the envelope of the standard deviation. In this figure, one can clearly see the two impinge locations at F and at H, H2. In Figure 3.1, it is also possible to note the crest of the seaward propagating reflected wave at E ( $t \approx 0.6$  s), D ( $t \approx 0.9$  s) and C ( $t \approx 1.2$  s).

Figure 3.2 (a) shows the cross-shore variation of the wave crest and corresponding trough level and setup and setdown (also seen in Table 3.1). Figure 3.2 (b) shows the time averaged horizontal fluid velocities, the maximum and minimum values of ensemble averaged horizontal fluid velocities near the bottom ( $z' = 0.00 - 0.40$  cm). The measurement locations for both free surface elevations and velocity are shown in Figure 3.2 (c). The waves were observed to plunge on the 1:10 slope, as anticipated. As seen in Figure 3.2 (a), the wave begins breaking at cross-shore location C and impinges at F, reforms at G, and breaks again at

location H. During this process, the flows by the strongly plunging waves reached the bottom. In Figure 3.2 (b), the magnitudes of the minimum ensemble averaged horizontal fluid velocities (i.e., offshore direction) are larger than the maximum ensemble averaged horizontal fluid velocities (i.e., onshore direction) from F to I2 except at G. The time averaged horizontal fluid velocities also increase in the offshore direction. In Figure 3.3, the low frequency motion was observed to be small based on the spectrum of free surface elevation. Therefore, the ensemble averaging method was employed and will allow for comparison with previous studies (e.g., Cowen *et al.*, 2003).

Table 3.1 Free surface elevation and near bottom velocity measurements at each location.  $u$  is reported considering only near bottom elevations ( $z' = 0.00 - 0.40$  cm).  $C$  is estimated  $C = \sqrt{g(h + \eta_c)}$

Location	$X$ (m)	$d$ (cm)	$\eta_t$ (cm)	$\eta_c$ (cm)	$\bar{\eta}$ (cm)	$h$ (cm)	$\bar{u}$ (cm/s)	$\langle u \rangle_{\max}$ (cm/s)	$\langle u \rangle_{\min}$ (cm/s)	$C$ (cm/s)
A	24.85	19.00	-2.69	12.88	-0.17	18.83	-3.51	45.18	-20.10	176.37
B	25.33	14.20	-2.66	11.53	-0.17	14.03	-3.53	50.20	-21.85	158.35
C	25.54	12.10	-3.52	12.15	-0.21	11.89	-3.72	61.39	-23.18	153.57
D	25.71	10.40	-3.17	9.87	-0.35	10.05	-5.00	66.68	-34.12	139.79
E	25.91	8.40	-3.19	7.35	-0.48	7.92	-7.58	73.43	-44.54	122.39
F	26.13	6.20	-2.04	2.05	-0.21	5.99	-20.02	40.09	-50.98	88.81
G	26.27	4.80	-1.42	5.71	1.04	5.84	-9.49	44.65	-38.74	106.45
H	26.46	2.90	-0.24	4.22	1.66	4.56	-16.49	38.04	-45.48	92.81
H2	26.55	2.00	0.61	4.09	2.10	4.10	-18.80	42.56	-54.14	89.63
I	26.68	0.70	0.66	5.28	2.57	3.27	-17.93	34.64	-51.67	91.58
I2	26.86	-1.10	-	-	-	-	-16.51	30.12	-45.43	-
J	26.90	-1.50	0.88	4.35	2.22	2.22	-	-	-	-
K	27.03	-2.80	0.29	2.53	1.26	1.26	-	-	-	-
L	27.22	-4.70	0.02	1.25	0.62	0.62	-	-	-	-
M	27.39	-6.40	0.03	0.68	0.30	0.30	-	-	-	-

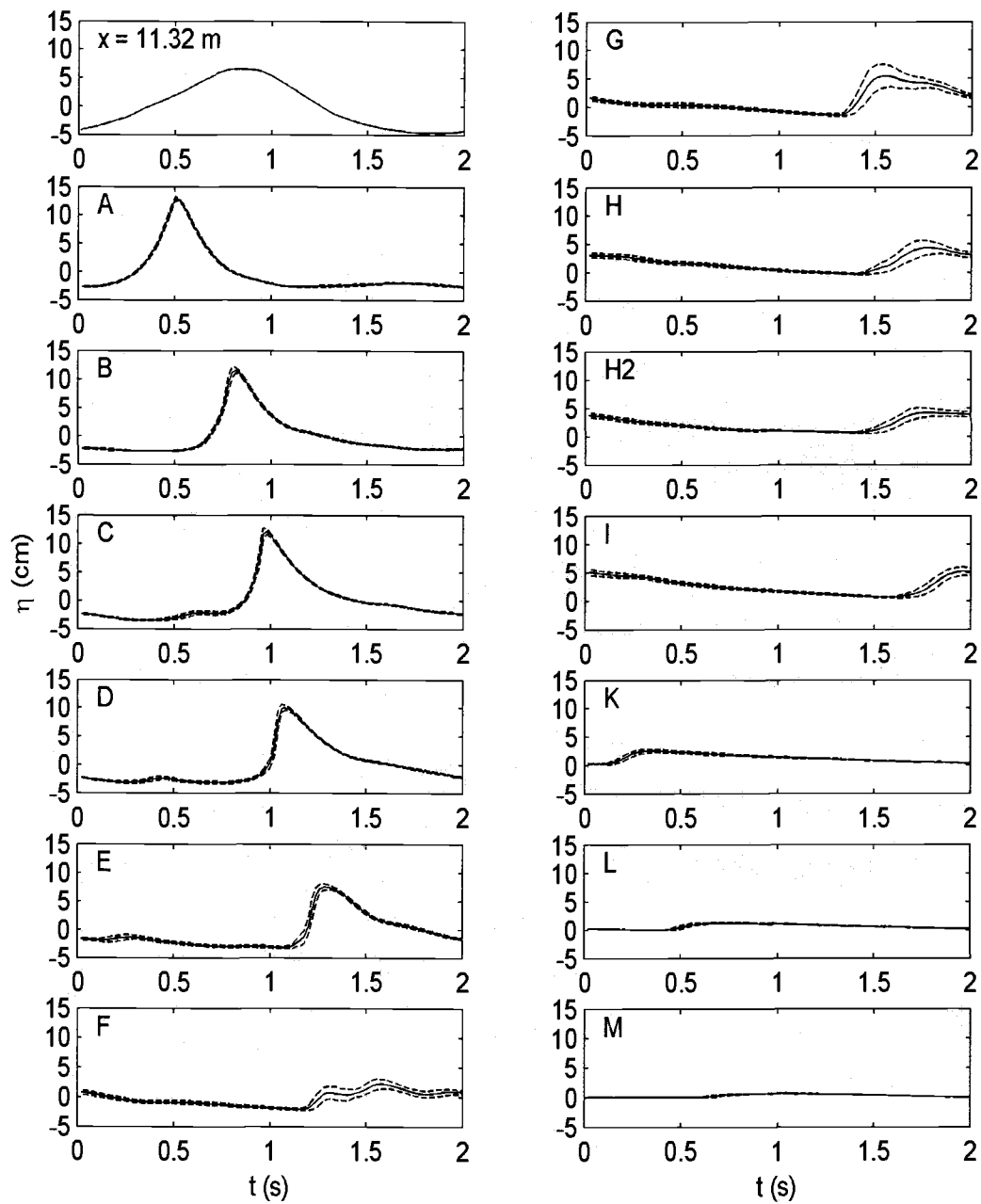


Figure 3.1 Spatial variation of free surface elevation (solid line) and envelope of one standard deviation (dashed line).

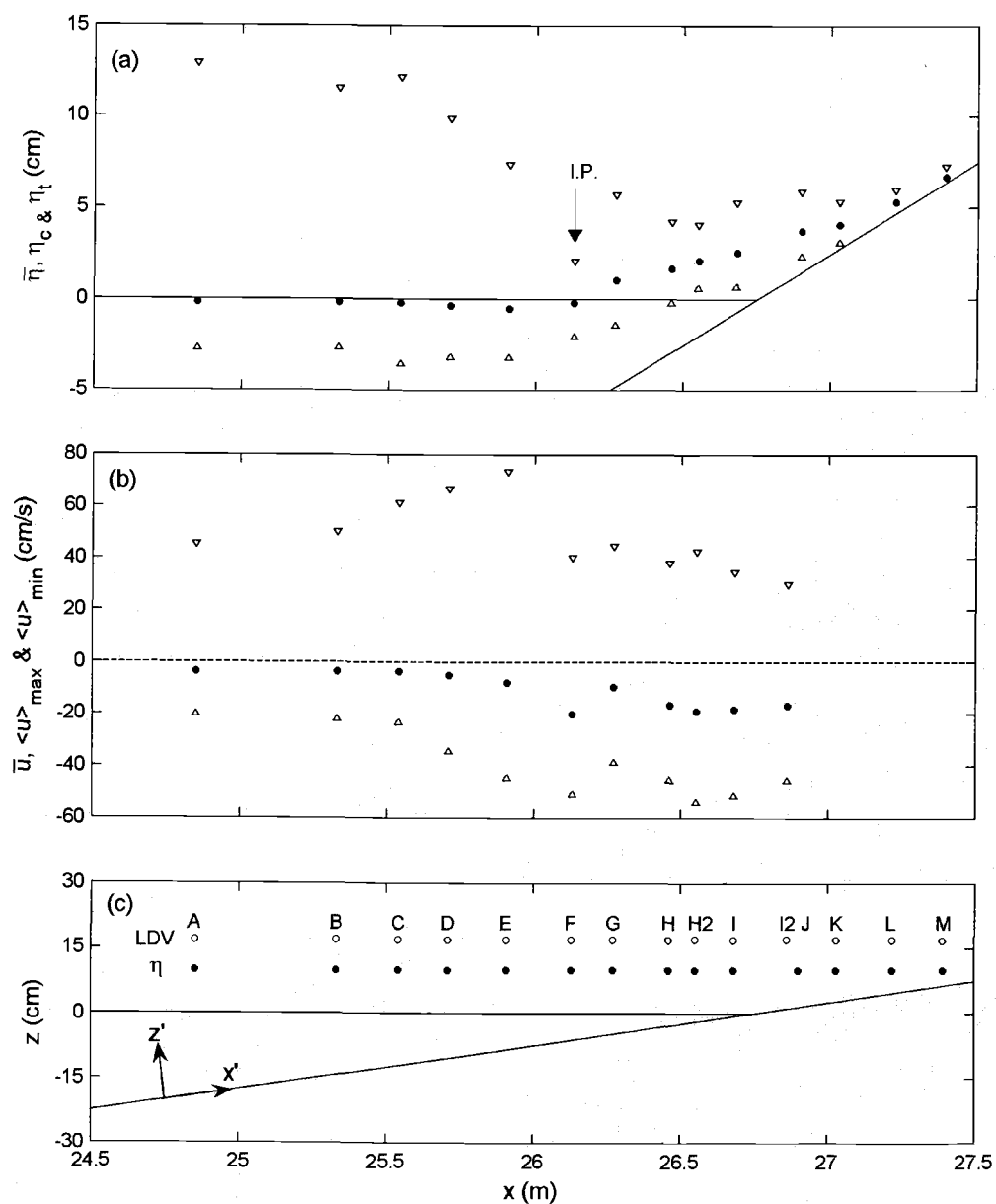


Figure 3.2 Cross-shore variation of wave characteristics and measurement locations: (a) mean water levels ( $\bar{\eta}$ ), crest levels ( $\eta_c$ ), and trough levels ( $\eta_t$ ). The arrow shows the first impinge point at F; (b) time averaged horizontal fluid velocities ( $\bar{u}$ ), the maximum ( $\langle u \rangle_{\max}$ ) and minimum ( $\langle u \rangle_{\min}$ ) ensemble averaged velocities near the bottom ( $z' = 0.00 - 0.40$  cm); (c) coordinate system and measurement locations of the wave gage and LDV.

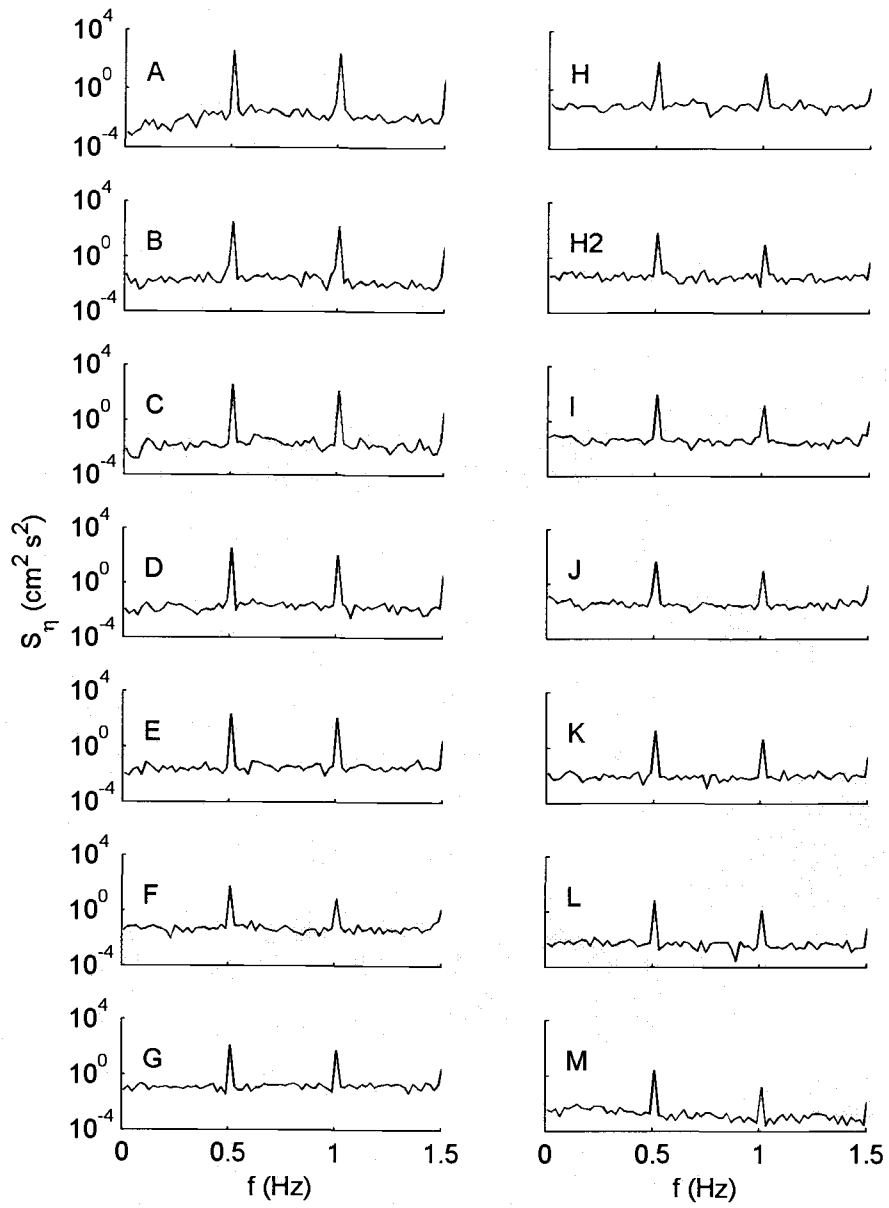


Figure 3.3 The spectra of free surface elevation at all cross-shore locations.

Due to the transient nature of the flow, the seeding material needed to be introduced continuously during each run, and this led to an effective sampling rate that varied from 100 to 1000 Hz. To analyze the data, it was first necessary to bin average the records to a constant rate of 100 Hz. This bin size was chosen based on previous studies of surf zone turbulence conducted in small-scale laboratory flumes (e.g., Cox, 1995; Ting and Kirby, 1994). During the bin averaging process, when a particular bin had no data due to air bubbles or probe exposure to air (above trough level), the interval was considered to have a signal drop out. In particular, large numbers of signal dropouts occurred at the first impinge point, F, and second impinge points, H and H2.

The measured instantaneous velocity  $u$  can be considered to consist of a steady component ( $\bar{u}$ ), an organized or irrotational component ( $\tilde{u}$ ), and a turbulent component ( $u'$ ):

$$u = \bar{u} + \tilde{u} + u' \quad (3.1)$$

For the case of periodic waves, it is possible to use ensemble averaging techniques to estimate the wave component, denoted as  $\langle u \rangle$ . In this study, we assume that  $\tilde{u}$  and  $\langle u \rangle$  are the same and that the turbulent component can be estimated by:

$$u' = u - (\bar{u} + \langle u \rangle) \quad (3.2)$$

Using these instantaneous turbulent velocities extracted from both cross-shore and vertical velocities, the instantaneous turbulent kinetic energy ( $k$ ) can be defined as

$$k = \frac{1.33}{2} (u'^2 + w'^2) \quad (3.3)$$

where  $w'$  is vertical component of turbulent velocity. Additional discussion of TKE is provided in Chapter 4.

In using the ensemble averaging method, we acknowledge two limitations. First, any motion that is rotational but repeatable (as is likely the case with an overturning jet) will be considered part of the organized wave motion and would therefore lead to an underestimation of the turbulent intensity. Second, any large deviations due to irregularities in wave breaking will lead to additional “psuedo-turbulence” and would cause an overestimation of the turbulent intensity. An additional discussion can be found in Nadaoka *et al.* (1989).

Petti and Longo (2001) suggested that if a well-identified trigger is available the Variable Interval Time Average (VITA), proposed by Blackwelder

and Kaplan (1976), can produce a more correct and unbiased result to reduce long wave components compared to other methods (e.g., phase-average, moving average). In this study, the VITA technique could not be applied since no hardware trigger was used in the experimental set-up, nor could this be done in post processing due to the signal dropouts near the zero up-crossing points.

Consistent with the treatment for free surface measurements, 103 waves were used to calculate the ensemble averaged horizontal and vertical velocity. This number was chosen based on previous studies (e.g., Nadaoka *et al.*, 1989; Okayasu *et al.*, 1988; Ting and Kirby, 1994). Ting and Kirby (1994) used 102 waves and checked the sensitivity of ensemble averaged statistics to the number of waves used. They showed that ensemble averaged statistics for  $\bar{u}$  and turbulent intensities for both horizontal ( $\overline{u'^2}$ ) and vertical ( $\overline{w'^2}$ ) components were stable (relative deviation  $< \pm 5\%$ ) if the number of waves was greater than 40 (Fig. 2. in their paper). In our study, visual inspection showed that fewer points were needed for  $\langle u \rangle$  (5-10). Values of  $u'$  and  $w'$ , however, are reported here only when there were 40 or more observations at that phase.

Figure 3.4 shows the temporal variation of the free surface elevation and horizontal and vertical velocity for a portion of the measurements at location E at an elevation of  $z' = 1.6$  cm above the bottom. Figure 3.4 (a) and (c) show the

horizontal and vertical velocities, respectively, including both the instantaneous velocity and the ensemble averaged velocity repeated at each wave period. Figure 3.4 (b) and (d) show the corresponding instantaneous turbulent velocities.

Due to the nature of the LDV signal processing, dropouts occur in  $u$  and  $w$  simultaneously. Figure 3.4 (e) and (f) show the instantaneous Reynolds stress ( $u'w'$ ) and TKE ( $k$ ). Comparison of these panels shows that both  $u'w'$  and  $k$  are strongly phase-dependent, where intense, short-lived events coincide with the arrival of the wave crest. The motion is fairly periodic and occurs with the passage of most waves. These results are similar to the boundary layer turbulence observed by Cox and Kobayashi (2000) under non-breaking regular waves. However, it contradicts to their observations of an intermittent signal in the surf zone that did not repeat with each wave. Because the large events are observed to occur with the passing of nearly each wave in the present study, it is reasonable to present the ensemble averaged values of  $k$  as representative of the turbulent variation over one wave period.

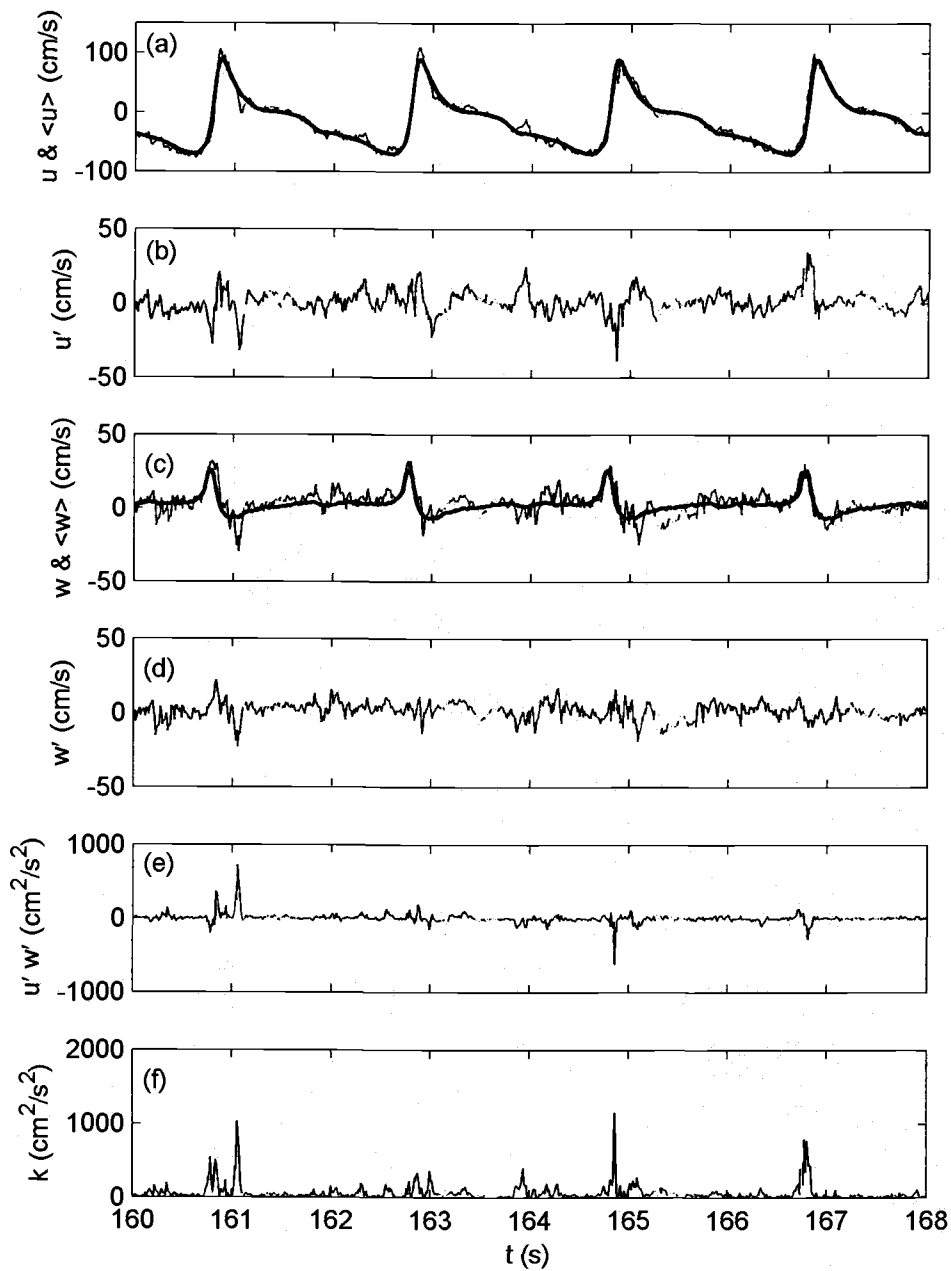


Figure 3.4 Example of measured velocity and calculated turbulent quantities at E ( $z' = 1.6$  cm). Bold lines are the ensemble averaged quantities and thin lines are the instantaneous quantities.

Figure 3.5 to Figure 3.7 show the vertical profile of the ensemble averaged horizontal and vertical fluid particle velocities ( $\langle u \rangle$  and  $\langle w \rangle$ ) at three cross-shore locations (A, E, and I2). The figures at the rest of cross-shore location are shown in Appendix B. In Figure 3.5,  $\langle u \rangle$  in the wave boundary layer (less than 1 cm from the bottom in this figure) lead in phase compared with upper layer, which is typically seen in laminar flow. This phase lead continues to the surf zone (at E in Figure 3.6).

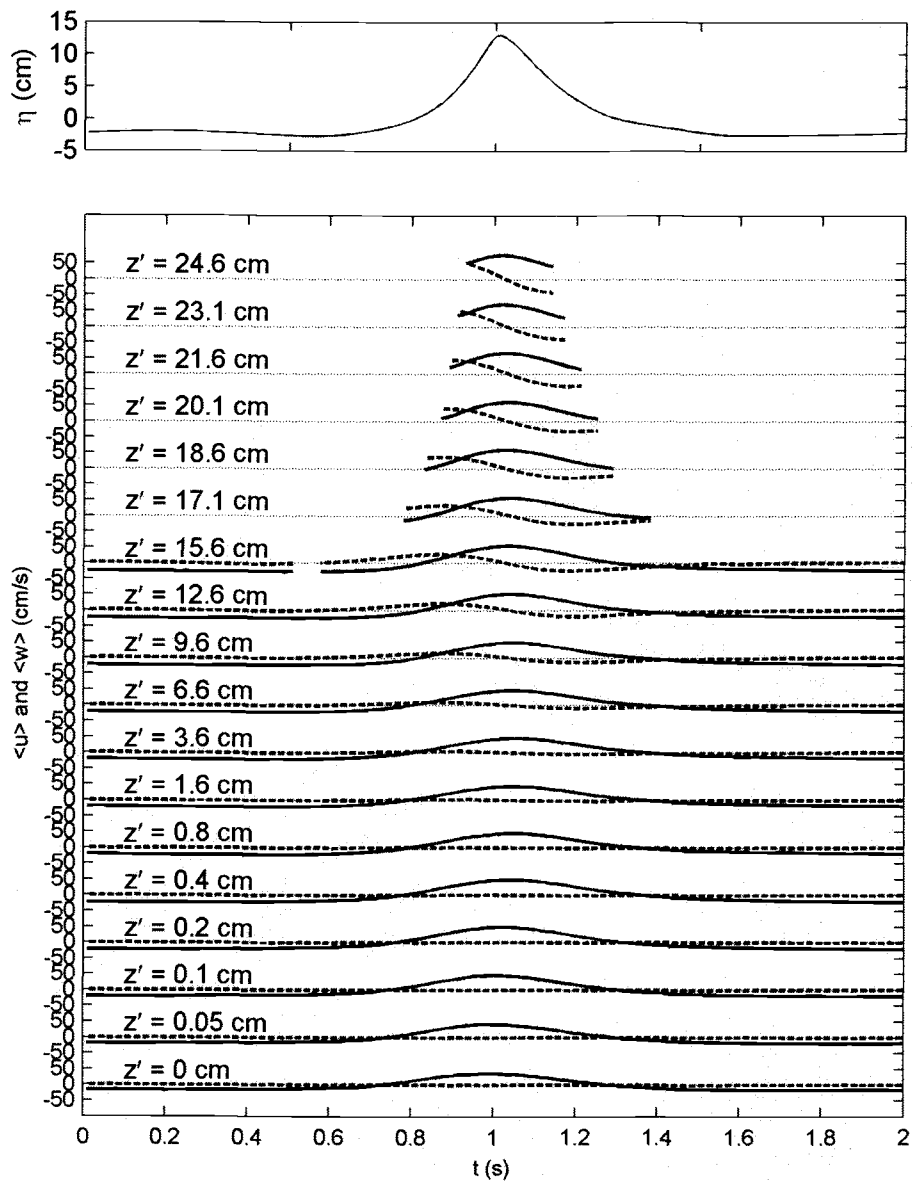


Figure 3.5 The vertical profile of the ensemble averaged horizontal and vertical fluid particle velocities ( $\langle u \rangle$  and  $\langle w \rangle$ ) at A. Solid lines are  $\langle u \rangle$  and dashed lines are  $\langle w \rangle$ .

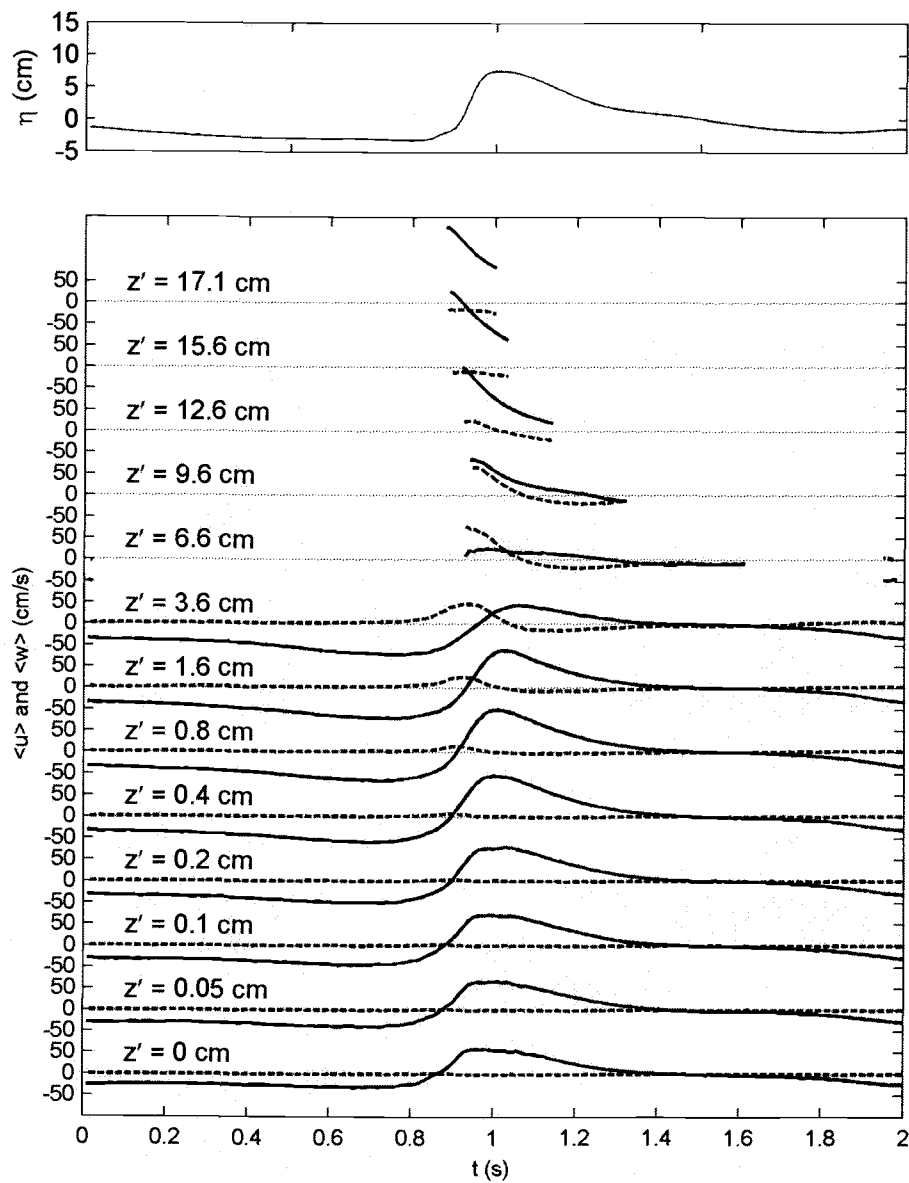


Figure 3.6 The vertical profile of the ensemble averaged horizontal and vertical fluid particle velocities ( $\langle u \rangle$  and  $\langle w \rangle$ ) at E. Solid lines are  $\langle u \rangle$  and dashed lines are  $\langle w \rangle$ .

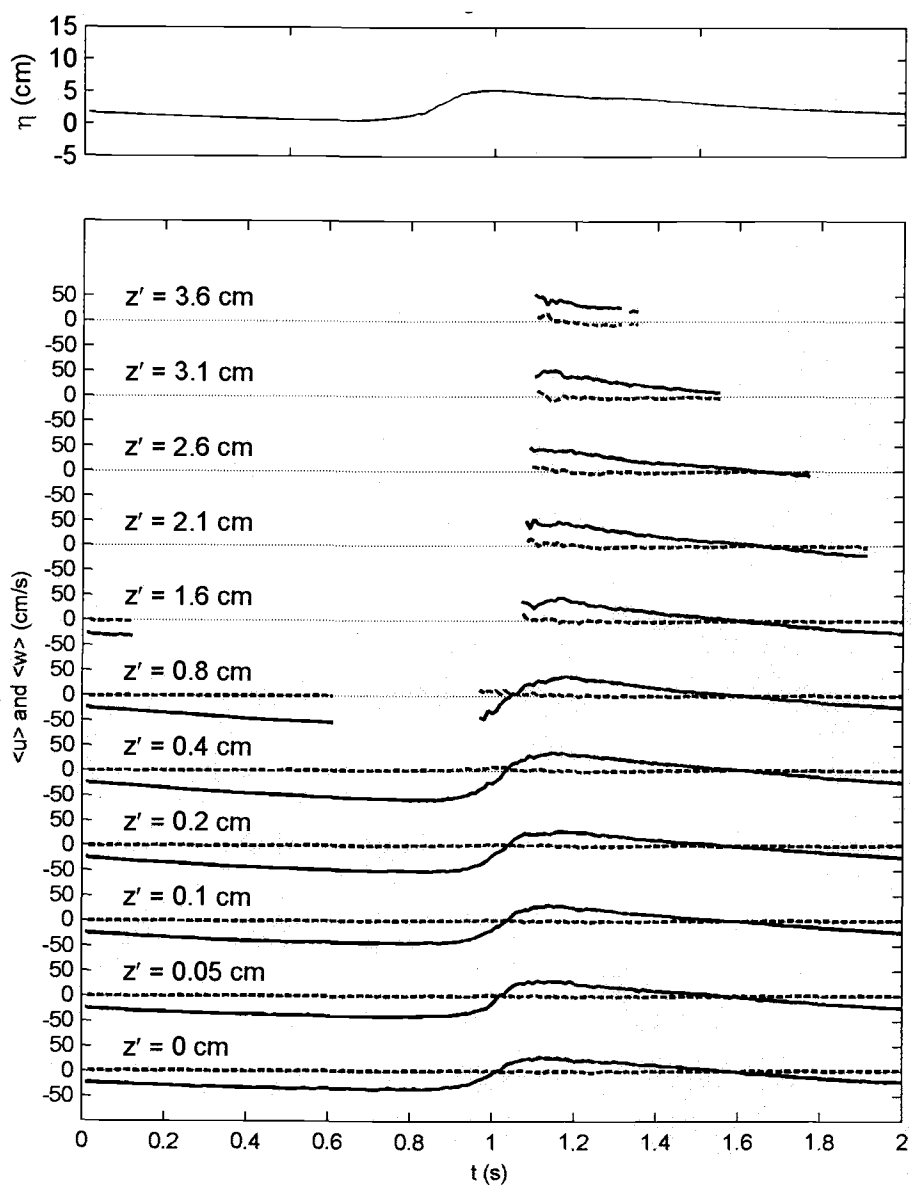


Figure 3.7 The vertical profile of the ensemble averaged horizontal and vertical fluid particle velocities ( $\langle u \rangle$  and  $\langle w \rangle$ ) at I2. Solid lines are  $\langle u \rangle$  and dashed lines are  $\langle w \rangle$ .

Figure 3.8 shows contour plots of the ensemble averaged wave induced horizontal velocity  $\langle u \rangle$  at E, F, and G. At E,  $\langle u \rangle$  near the bottom leads in phase compared to the upper layer. At F, the free surface wave shape is irregular and the instantaneous velocity could not be measured easily throughout the water column for approximately  $0.35 < t/T < 0.50$  due to air entrainment. In Figure 3.8, we plot only those values of  $\langle u \rangle$  for which the number of waves exceed 40 at a given phase to highlight the extent of the aerated flow. In addition, the largest measured speed occurs during the return flow ( $u_{\min} = -50.98$  cm/s) compared to the forward motion ( $u_{\max} = 40.09$  cm/s), contrary to the maximum and minimum values observed at E and G (see also Table 3.1 and Figure 3.2 (b)). At G, the wave reforms and the wave height increases accordingly. The entrained air, seen as dropouts in Figure 3.8 (c), remains in the upper water column and is advected past the crest ( $t/T \approx 0.55$ ), making it possible to obtain measurements for all phases near the bottom. The second impinging points (location H and H2) indicate a phenomenon similar to F in Figure 3.9.

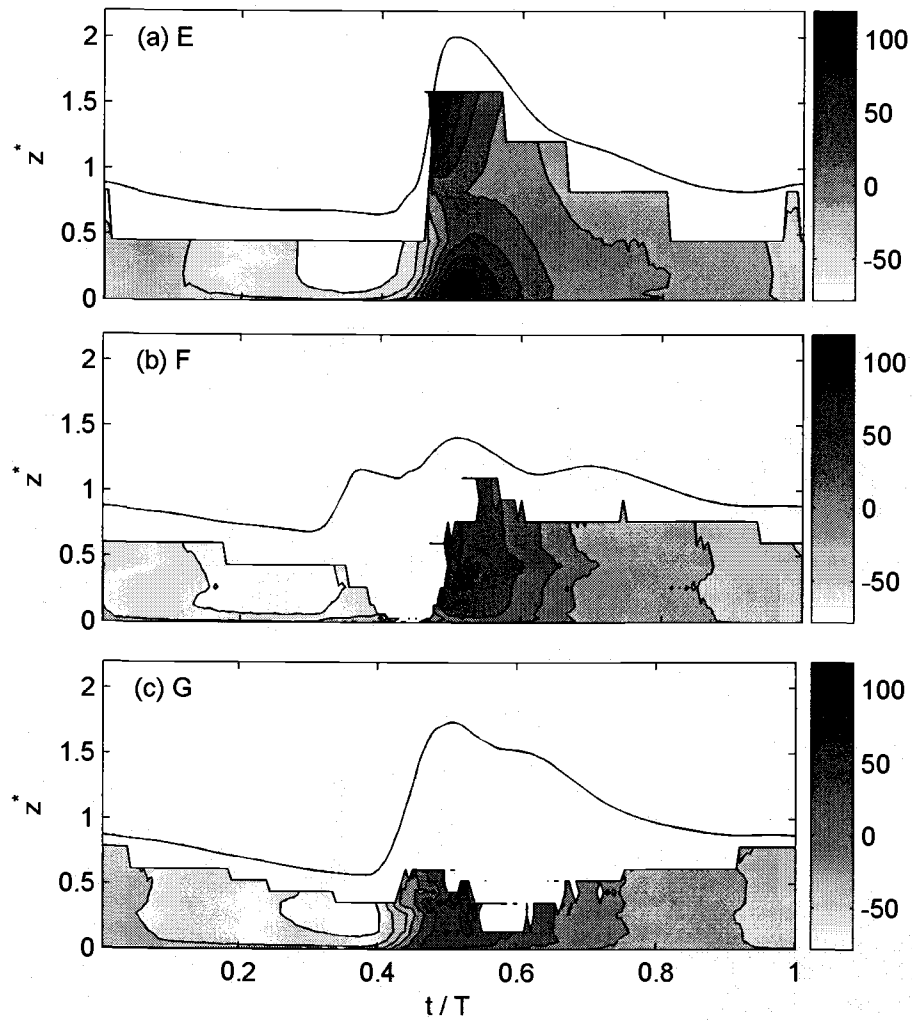


Figure 3.8 Contour plots of ensemble averaged wave induced horizontal velocities (cm/s) and free surface elevations (envelopes) at E, F, and G.  $z^*$  is normalized water depth ( $z^* = z' / h$ ).

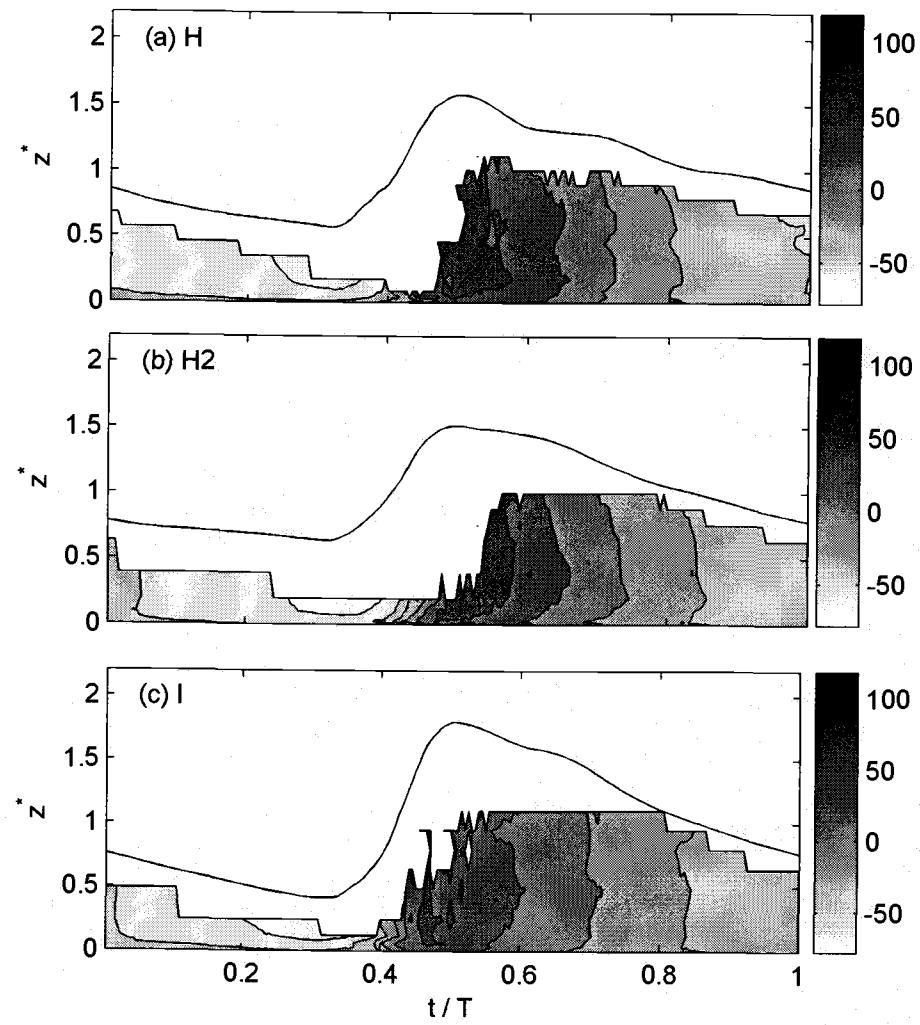


Figure 3.9 Contour plots of ensemble averaged wave induced horizontal velocities (cm/s) and free surface elevations (envelopes) at H, H2, and I.  $z^*$  is normalized water depth ( $z^* = z' / h$ ).

## 4 Turbulence in the inner surf and swash zone

### 4.1 Time Averaged Turbulence

The turbulent kinetic energy per unit mass is typically defined as

$$\bar{k} = \frac{1}{2}(\overline{u'^2} + \overline{v'^2} + \overline{w'^2}) \quad (4.1)$$

where  $u'$ ,  $v'$ ,  $w'$  are the turbulent velocity components in cross-shore, alongshore, and vertical directions, respectively, and the overbar refers to the turbulent intensity averaged over the entire time series. LDV velocity measurements typically include only  $u$  and  $w$ . To circumvent this limitation an alternative equation based on the assumption of plane wake turbulence was suggested by Svendsen (1987) for surf zone flows as

$$\bar{k} = \frac{1.33}{2}(\overline{u'^2} + \overline{w'^2}) \quad (4.2)$$

To assess the validity of the coefficient (=1.33) in Eq. (4.2), we now look at the ratio of  $\overline{u'^2}$  to  $\overline{w'^2}$  at a variety of vertical and cross-shore locations extending from the surf zone to swash zone. Svendsen (1987) tabulated the relative strength of the three turbulent velocity components and the ratio of  $\bar{k}$  to  $\bar{k}'$ , for different

flow types, where  $\bar{k}' = (1/2)(\overline{u'^2} + \overline{w'^2})$ , (Table 4.1). They showed that the range of  $\overline{u'^2} / \overline{w'^2}$  varies from 1.00 for homogeneous, isotropic turbulence to 6.20 for the inner region of the boundary layer. The range in variation of  $\bar{k} / \bar{k}'$  is much smaller and varies from 1.27 for near bottom open channel flow to 1.50 for homogeneous, isotropic turbulence.

Table 4.1 Relative turbulent intensities of  $\overline{u'^2}$  and  $\overline{w'^2}$  normalized by  $2\bar{k}$ , and their ratio (Svendsen, 1987).

Flow type	$\overline{u'^2}$	$\overline{w'^2}$	$\bar{k} / \bar{k}'$	$\overline{u'^2} / \overline{w'^2}$
Plane wake	0.42	0.32	1.33	1.31
Plane mixing layer	0.47	0.27	1.36	1.75
Boundary layer				
Inner region	0.62	0.10	1.39	6.20
Outer region	0.45	0.23	1.47	1.96
Plane jet	0.42	0.30	1.40	1.40
Open channel				
Midstream	0.58	0.20	1.28	2.90
Near bottom	0.62	0.17	1.27	3.65
Homogeneous, isotropic	0.33	0.33	1.50	1.00

Figure 4.1 shows the vertical and cross shore variation of  $\overline{u'^2} / \overline{w'^2}$  for location E, G, H2, I and I2. At E, the range of  $\overline{u'^2} / \overline{w'^2}$  is 1.50 for the two points for which  $z' > 1$  cm (1.69 and 1.30 at  $z' = 1.60$  cm and 3.60 cm, respectively) and agrees well with the case of plane wake turbulence ( $\overline{u'^2} / \overline{w'^2} = 1.31$ ). For  $z' < 1$

cm at E and at the other locations in Figure 4.1,  $\overline{u'^2}/\overline{w'^2}$  is larger and on average 5.91, which is closer to flows typified by the inner region of a boundary layer ( $\overline{u'^2}/\overline{w'^2} = 6.20$ ). Considering all the data in Figure 4.1, there appears to be a difference in  $\overline{u'^2}/\overline{w'^2}$  with respect to elevation, but there seems to be little variation between the surf and swash zones. Given this fact and that the variation in  $\overline{k}/\overline{k'}$  is less than  $\overline{u'^2}/\overline{w'^2}$  for flows listed in Table 4.1, it seems reasonable to assume a constant value for  $\overline{k}/\overline{k'}$ . For this paper, we assume  $\overline{k}/\overline{k'} = 1.33$  (Eq. 4.1), which is consistent with the works of others (e.g., Ting and Kirby, 1995; Cowen *et al.*, 2003).

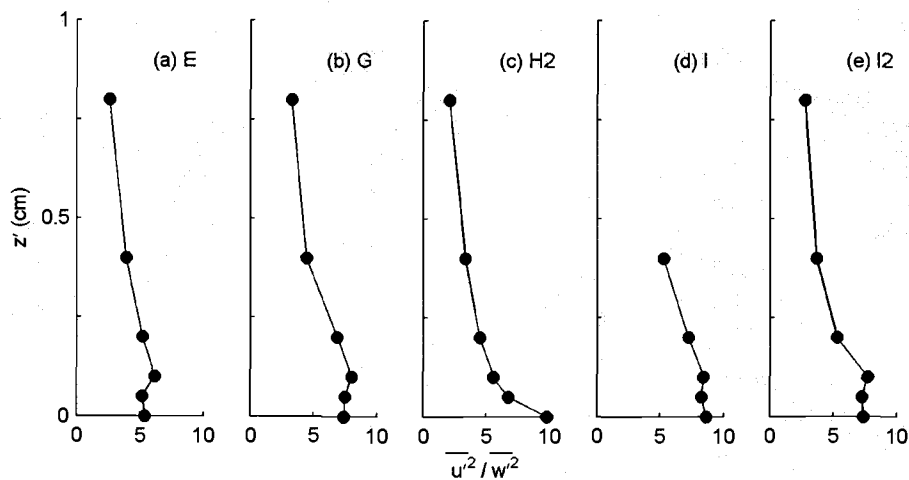


Figure 4.1 The vertical structure of the ratio of  $\overline{u'^2}$  to  $\overline{w'^2}$  along the cross-shore measurement locations. At E,  $\overline{u'^2}/\overline{w'^2}$  is 1.69 at  $z'=1.60$  cm and 1.30 at  $z'=3.60$  cm.

Figure 4.2 shows the vertical variation of a time-averaged estimate of  $\langle k \rangle$  for the five cross-shore locations shown in Figure 4.1. The time-average was taken only over that portion of the record for which data exists over all phases as seen in Figure 4.3 and Figure 4.4. At F and H, no estimates are reported because air entrainment precluded estimates of  $\langle k \rangle$  at the most important phases but are likely to be higher than G. As expected, the variation in  $\overline{\langle k \rangle}$  is fairly uniform over the vertical.

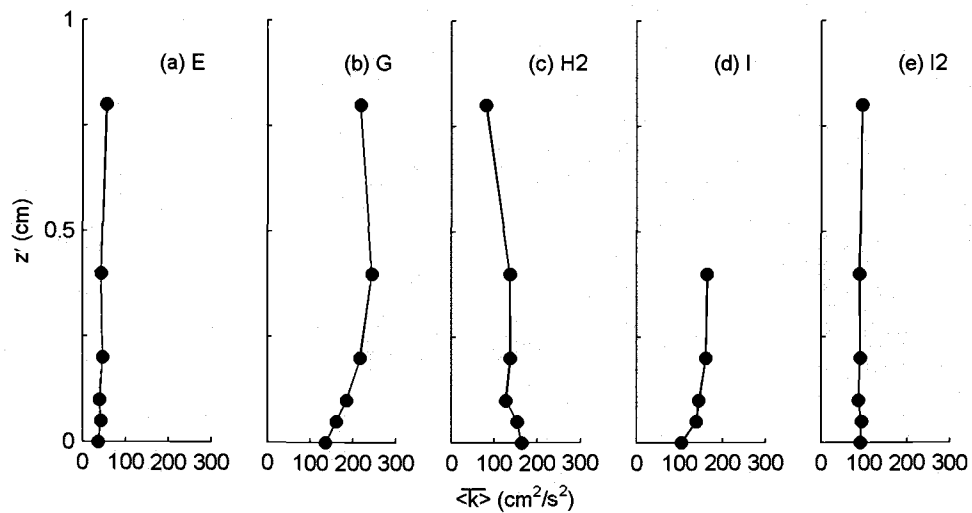


Figure 4.2 The vertical structures of  $\overline{\langle k \rangle}$  in the inner surf and swash zone.

## 4.2 Ensemble Averaged Turbulence

Figure 4.3 shows the contour plot of the temporal variation of  $\langle k \rangle$  with depth, computed using ensemble averaged estimates of the turbulence intensity and the coefficient of 1.33:

$$\langle k \rangle = \frac{1.33}{2} (\langle u'^2 \rangle + \langle w'^2 \rangle) \quad (4.3)$$

$z^*$  is the dimensionless vertical coordinate ( $z^* = z'/h$ ) in these figures. In Figure 4.3, the lower panel (b) shows the temporal variation of  $\langle u \rangle$  for two elevations at E, one near the bed ( $z' = 0.10$  cm;  $z^* = 0.013$ ) and the other above the wave boundary layer ( $z' = 1.60$  cm;  $z^* = 0.202$ ). The upper panel shows that  $\langle k \rangle$  has a peak just below trough level ( $z' = 3.96$  cm;  $z^* = 0.5$ ) in phase with the wave crest ( $t/T = 0.5$ ) and that the energy is mostly dissipated after the passage of the crest. Also, there is a shift in phase of the peak intensity with depth. Comparison of the upper and lower panels shows that the peak in  $\langle u \rangle$  at  $z' = 1.6$  cm is in phase with both the free surface and  $\langle k \rangle$  just below trough level. At  $z' = 0.1$  cm, however,  $\langle u \rangle$  is leading in phase, and there appears to be a sharp vertical gradient of horizontal velocity, particularly for the reverse flow for  $0.2 < t/T < 0.4$ , suggesting that boundary layer processes may be important. Note that for  $0.6 < t/T < 1.0$ , the

curves for  $\langle u \rangle$  are the same at both elevations, presumably the result of turbulent mixing due to wave breaking.

Figure 4.4 is similar to Figure 4.3 measured at I2 after the impinge point. Figure 4.4 shows that  $\langle k \rangle$  appears to be better mixed in the vertical compared to location E. The large value of  $\langle k \rangle$  near the bottom just prior to arrival of the wave crest is evident, suggesting that the turbulence generated near the still water shore line is a combination of the return flow from the preceding wave and the uprushing bore.

In an initial attempt to suggest some relation among the mean, wave, and turbulent components, it is instructive to look at the cross-shore variation of bulk parameters commonly used to model sediment transport in the surf and swash zone. Figure 4.5 shows the cross-shore variation of  $H$ ,  $\overline{\langle \eta \rangle}$ ,  $\overline{\langle u \rangle}$ , the skewness and asymmetry based on  $\langle u \rangle$  measured near the bottom and  $\eta$ , and estimates of  $\overline{\langle k \rangle}$  averaged over the four bottom points at each cross-shore location. As has been discussed, air entrainment was an important process at the impinge point and caused large dropouts in the LDV signal. At F for  $0.35 < t/T < 0.50$ , for example, there were a number of phases for which number of waves with reliable data was less than 40. At F and H (open circles without error bar),  $\overline{\langle k \rangle}$  was unreliable for

10% of the wave phase and was replaced by linear interpolation so that the measured data could be compared to the numerical results as shown in Chapter 5. However, reasonable estimates of  $\langle u \rangle$  were possible with a number as small as 10, and therefore, it was possible to get an estimate of  $\overline{\langle u \rangle}$  even in the highly aerated region using cubic spline interpolation. In Figure 4.5, the estimated error bars of  $H$  and  $\overline{\langle u \rangle}$  were included and the error bars of  $\overline{\langle \eta \rangle}$  are not plotted due to the small error ranges (0.4 – 1.7 mm). The error bars of each quantity were calculated using the standard deviation of the undertow computed on a wave-by-wave using the zero-upcrossing method. Comparison of Figure 4.5 (a) and (b) shows that the undertow increases ( $\overline{\langle u \rangle}$  decreases) as the wave height decreases from B to F and then decreases during the wave rebound at G, consistent with an increase in wave height. This variation is not reflected in the wave induced setup  $\overline{\langle \eta \rangle}$ . The large negative value of  $\overline{\langle u \rangle}$  at F compared to E and G is consistent with the large negative velocity observed in Figure 3.8. Short periods of strong downward flow (negative  $\langle w \rangle$ ) were also observed at some phases at G, suggesting a flow divergence at the impinging point. Figure 4.5 (c) compares the cross-shore variation of skewness computed using  $\langle \eta \rangle$  and using  $\langle u \rangle$  for the bottom four measurements. While both skewness estimates exhibit a similar trend of decreasing shoreward, the values are significantly different for A and B which are

both seaward of breaking. At the most landward observations of  $\langle u \rangle$  (H2, I, and I2) however, the values are similar. Figure 4.5 (d) shows a general trend of wave asymmetry increasing shoreward. Similar to (c), the agreement between asymmetry calculated from  $\langle \eta \rangle$  and  $\langle u \rangle$  is better near the still water shoreline than at breaking. Figure 4.5 (e) shows the cross shore variation of  $\overline{\langle k \rangle}$  based on the average of the five observations deepest in the water column. Since  $\overline{\langle k \rangle}$  at F and H were obtained using interpolation, there is large uncertainties at these points although it is likely that  $\overline{\langle k \rangle}$  exhibits a maximum value at the impinge point (F) based on visual observations. These data will be compared with the numerical model results in next chapter. In this figure, the higher order statistical quantities, skewness and asymmetry, were employed. These represent wave shoaling and nonlinearity.

Skewness is defined as:

$$S(x) = \frac{\overline{(x-m)^3}}{[\overline{(x-m)^2}]^{3/2}} \quad (4.3)$$

Asymmetry is defined as:

$$A(x) = \frac{H[\overline{(x-m)^3}]}{[\overline{(x-m)^2}]^{3/2}} \quad (4.4)$$

where  $x$  is variable,  $m$  is mean value of  $x$ . The overbar denotes a time average.  $H$  is the Hilbert transform. The equation (4.3) and (4.4) were defined by Elgar and Guza (1985).

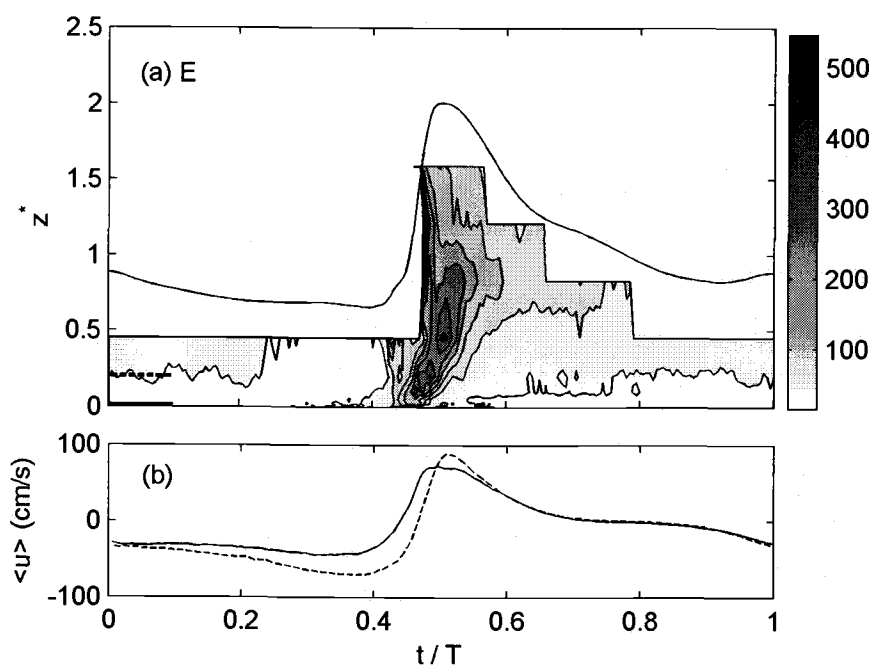


Figure 4.3 A contour plot of ensemble averaged turbulent kinetic energy  $\langle k \rangle$  in  $\text{cm}^2/\text{s}^2$  (a) and wave induced horizontal velocities  $\langle u \rangle$  (b) at E. In (b), solid line is the wave velocity at  $z' = 0.10 \text{ cm}$  ( $z^* = 0.013$ , shown by the heavy solid line in (a)) and dashed line is at  $z' = 1.60 \text{ cm}$  ( $z^* = 0.202$ , shown by the heavy dashed line in (a)).

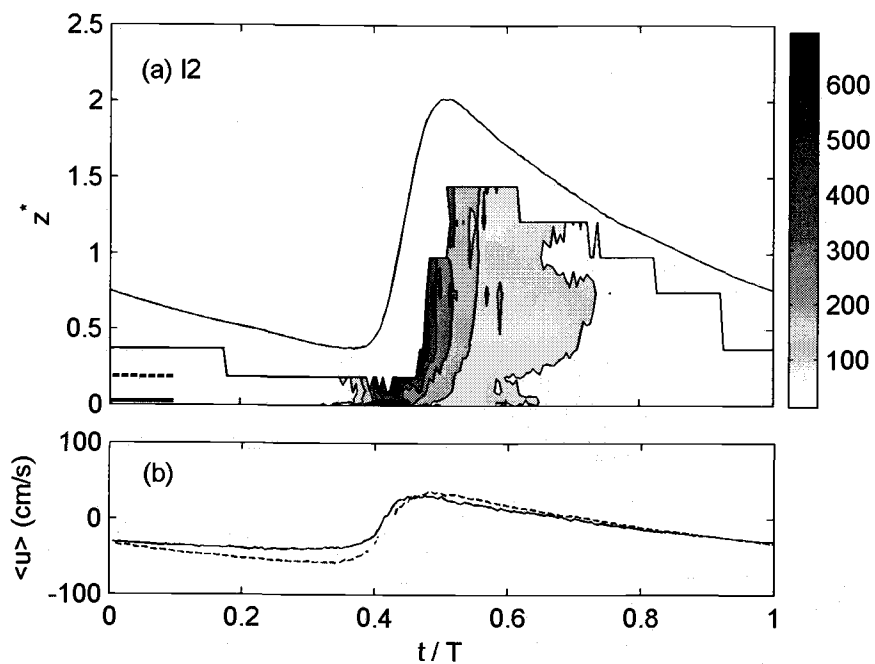


Figure 4.4 A contour plot of ensemble averaged turbulent kinetic energy  $\langle k \rangle$  in  $\text{cm}^2/\text{s}^2$  (a) and wave induced horizontal velocities  $\langle u \rangle$  (b) at I2. In (b), solid line is the wave velocity at  $z' = 0.05 \text{ cm}$  ( $z^* = 0.023$ , shown by the heavy solid line in (a)) and dashed line is at  $z' = 0.40 \text{ cm}$  ( $z^* = 0.187$ , shown by the heavy dashed line in (a)).

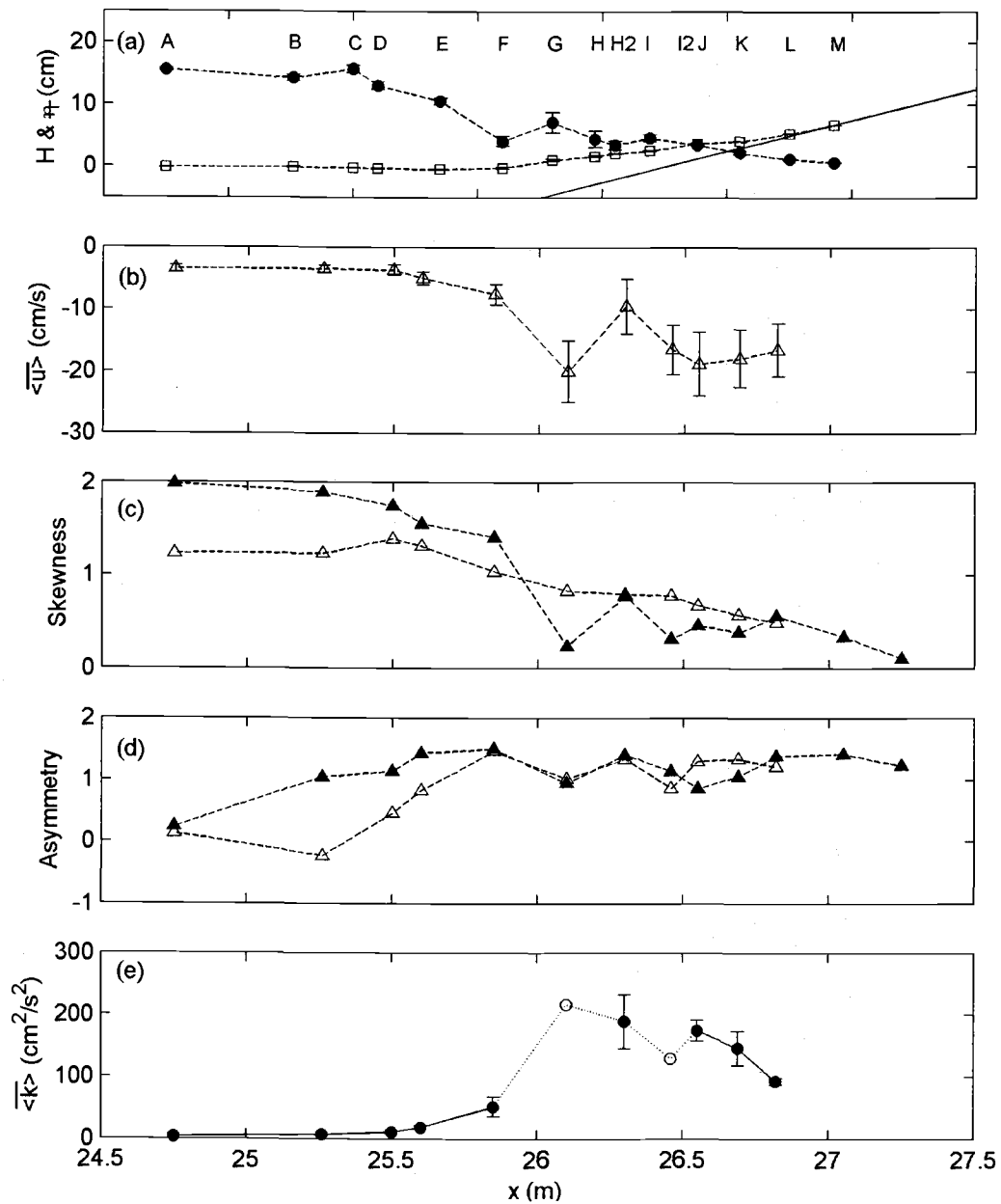


Figure 4.5 Cross-shore variations of hydrodynamic quantities near the bottom (averaged  $0 - 0.4$  cm). (a)  $H$  (●) and  $\bar{\eta}$  (□); (b) time averaged horizontal velocity, i.e. undertow ( $\langle \bar{u} \rangle$ , cm/s) near the bottom; (c) skewness of  $\langle u \rangle$  (△) and  $\eta$  (▲); (d) asymmetry of  $\langle u \rangle$  (△) and  $\eta$  (▲); (e)  $\langle k \rangle$  near the bottom ( $z' < 4$  mm). Open circles were specified in the text.

### 4.3 Discussion

In Figure 3.8, at E (surf zone),  $\langle u \rangle$  near the bottom leads in phase compared to  $\langle u \rangle$  to the upper layer. This result is similar to the ensemble averaged velocity vector in the surf zone presented by Nadaoka et al. (1989) in their Fig.13. They showed that even though their experiment was conducted for a smooth bottom roughness, the bottom-originated velocity affected the vertical profiles near the bottom. Cowen et al. (2003) obtained similar results from their laboratory experiment with a smooth bed. In this study, the effect of the rough bottom on the vertical velocity structure is larger than previous studies. This phase lead in the boundary layer (especially at E) also appears in the vertical structure of TKE. This shows that  $\langle u \rangle$  in the turbulent boundary layer may be important when considering rough bottom conditions. In the upper water column, the velocity at the bore front is high and exceeds the theoretical wave celerity ( $\langle u \rangle_{\max} / \sqrt{g(h + \eta_c)} = 1.09$ , where,  $\eta_c$  is wave crest height) in this region. This is relevant, for example, in modeling the surface roller (e.g., Schäffer et al., 1993) where  $u$  at the bore is equal to equal to 1.3 or 1.5 times wave celerity in the numerical models. In addition, the largest measured speed occurs during the return flow ( $u_{\min} = -50.98$  cm/s) compared to the forward motion ( $u_{\max} = 40.09$  cm/s), contrary to the maximum and minimum values observed at E and G (see also Table 3.1 and Figure 3.2 (b)).

As seen in the free surface elevation, location F is an impinge point, thus strong return flow near the bottom may have occurred. Petti and Longo (2001) showed the frame sequenced picture near the breaking region and the impinge point like F.

In Figure 4.3 and Figure 4.4, in the surf zone, there is a shift in phase of the peak intensity of  $\langle k \rangle$  with depth.  $\langle k \rangle$  inside the boundary layer leads in phase to the upper layer and there is a strong vertical gradient in both  $\langle u \rangle$  and  $\langle k \rangle$ . This seems to be closely related to the structure of  $\langle u \rangle$ . These results, however, do not appear to correspond with existing field observations. Butt et al. (2004) suggested that, where the bore is propagating in the upper layer, the previous downrush is in lower layer. This is consistent with these laboratory observations for locations outside the boundary, however, inside the boundary layer (approximately  $< 1$  cm from the bottom),  $\langle u \rangle$  leads in phase compared to the upper layer. Alternately, in the swash zone the vertical structure of  $\langle k \rangle$  is observed to be well mixed. The vertical gradient of  $\langle u \rangle$  is relatively small in comparison to the surf zone results. It can be explained that, in the swash zone, there is a stronger downrush than in the surf zone which can effect turbulent mixing. Finally, both figures indicate that the boundary layer effect on turbulence for rough bottom conditions and the bore generated turbulence in the inner surf and swash zones may play important roles in nearshore processes.

In Figure 4.5, taken as a whole, the lack of clear relationships between, for example,  $H$ ,  $\bar{\eta}$  and  $\bar{u}$  or skewness and asymmetry and corresponding changes in  $\langle \bar{u} \rangle$  or  $\langle \bar{k} \rangle$  would indicate that simple models of the cross-shore sediment transport in the swash zone on steep beaches may not accurately represent the physical hydrodynamic processes, even in a time-averaged sense.

In the present study, the fluid velocities were measured using a LDV. The measurements were carried out precisely and with a fine vertical resolution. The primary difficulty in this measurement was air entrainment in the broken wave region, especially at the impinge point. Here, the air bubbles caused the laser beam to scatter, resulting in a signal dropout. Particle Image Velocimetry (PIV) techniques also fail the measurement in the highly aerated bubbly flow due to the scattering of the laser sheet. Alternatively, Cox and Shin (2003) used a Void Fraction Meter (VFM) in the bore region of the surf zone. The results showed that the void fraction is highly correlated with the horizontal turbulent intensities above the trough level in the transition region. Another possible technique, Bubble Image Velocimetry (BIV), was proposed by Ryu et al. (2005). They succeeded to track the particle movement of a plunging wave with high bubble density. This technique may also be utilized to measure the fluid velocity in the inner surf and swash zone, due to the high bubble concentration there.

## 5 Numerical Comparisons

In this chapter, numerical model comparisons with measured data are carried out in terms of free surface elevations, fluid particle velocities, and turbulent quantities (two-dimensional model). In the previous chapters, the experimental results were the plunging breaker case with strong impinge points. The main objective of the numerical modeling in this chapter is to investigate the model capability to predict the hydrodynamics at the impinge points, which may be important for the sediment suspension and transport. In other words, this chapter aims to understand what level of model complexity is required to predict a given hydrodynamic variable. For example, a one-dimensional model may predict setup or skewness well, but may fail to predict the time-averaged horizontal velocity (undertow) or asymmetry. In addition, a more sophisticated and computationally more intense RANS model may not give a better description of overall wave height variation across the surf and swash zone relative to a one-dimensional model, but it may provide a better description of fluid velocities in the area of wave breaking.

Section 5.1 describes the one-dimensional model (RBREAK2) based on the nonlinear shallow water equations and shows the results of the comparisons. Section 5.2 includes a brief description of another one-dimensional model (FUNWAVE1D) based on the fully nonlinear Boussinesq equation and similar

comparisons. The two-dimensional model (COBRAS), based on the Reynolds Averaged Navier-Stokes Equations, is described and compared to the measured free surface elevation, fluid particle velocities, and turbulent kinetic energy in Section 5.3. In Section 5.4, the input bathymetry and free surface elevation was modified to initiate all three models with the same conditions. Additionally, a three-dimensional numerical model based on Large Eddy Simulation was run as a preliminary test in Appendix D.

## 5.1 One-Dimensional Model I: RBREAK2

Wurjanto and Kobayashi (1991) developed RBREAK and expanded it to RBREAK2 by adding the ability to input variable bottom friction factors and the total free surface oscillation at the seaward boundary. This model is based on the one-dimensional depth-averaged nonlinear shallow water equations with quadratic bottom friction,

$$\frac{\partial h'}{\partial t'} + \frac{\partial}{\partial x'}(h'u') = 0 \quad (5.1)$$

$$\frac{\partial}{\partial t'}(h'u') + \frac{\partial}{\partial x'}(h'u'^2) = -gh' \frac{\partial \eta'}{\partial x'} - \frac{1}{2} f' |u'|u' \quad (5.2)$$

where  $t'$  is time,  $u'$  is the depth-averaged horizontal velocity,  $g$  is the gravitational acceleration,  $x'$  is the horizontal distance from the seaward boundary,  $h'$  is the total water depth ( $h + \eta$ ),  $\eta'$  is the free surface elevation, and  $f'$  is the constant bottom friction factor. The following dimensionless variables are utilized to normalize (5.1) and (5.2):

$$t = \frac{t'}{T_r'} ; \quad x = \frac{x'}{T_r' \sqrt{gH_r'}} ; \quad u = \frac{u'}{\sqrt{gH_r'}} \quad (5.3)$$

$$z = \frac{z'}{H_r'} ; \quad h = \frac{h'}{H_r'} ; \quad \eta = \frac{\eta'}{H_r'} ; \quad d_t = \frac{d_t'}{H_r'} \quad (5.4)$$

$$\sigma = T_r' \sqrt{\frac{g}{H_r'}} ; \quad \theta = \sigma \tan \theta' ; \quad f = \frac{1}{2} \sigma f' \quad (5.5)$$

where,  $T_r'$  is the reference wave period,  $H_r'$  is the reference wave height,  $\sigma$  is the ratio between the horizontal and vertical length scales,  $\theta'$  is the normalized gradient of the local slope, and  $f$  is the normalized bottom friction factor.

Assuming that  $\sigma^2 \gg 1$  and  $(\cot \theta')^2 \gg 1$  (Kobayashi *et al.*, 1987; Kobayashi and Wurjanto, 1992), substitution of (5.3), (5.4), and (5.5) into (5.1) and (5.2) yields

$$\frac{\partial h}{\partial t} + \frac{\partial}{\partial x}(hu) = 0 \quad (5.6)$$

$$\frac{\partial}{\partial t}(hu) + \frac{\partial}{\partial x}(hu^2) = -\theta h - f|u|u \quad (5.7)$$

(5.6) and (5.7) are solved numerically in the time domain to obtain  $h$  and  $u$ .

The model was initiated with the free surface elevation data measured at A ( $H = 15.56$  cm). Fifty waves were used to compare the numerical results with the measured data 150 s after the initial wave generation to avoid transitional effect by inspecting the wave runup computed by the model. Water depth at the seaward boundary was 0.19 m. In this case, the friction factor was 0.01, which was estimated based on the friction velocity determined from the measured data. The horizontal grid spacing ( $dx$ ) was approximately 7 mm.

Figure 5.1 and Figure 5.2 show the temporal variation of the measured and simulated instantaneous free surface elevations. At most of the cross-shore locations, the model results agree well with the measured free surface elevations. From B to H2, the wave shape computed by RBREAK2 was more like a saw-tooth wave than the measured data since the waves broke earlier (at B) in the model than in the experiment. In the swash zone (I – M), the model estimated the wave shapes and phases well. However, in Figure 5.3, low frequency components of the spectra by RBREAK2 are larger than those of the measured spectra. In this case, RBREAK2 overpredicted low frequency motion as waves go from the inner surf zone to the swash zone.

Figure 5.4 (a) shows the cross-shore variation of the wave height and setup for both the measured and the simulated results. The RBREAK2 results agree with the measured variations in the wave height and setup but did not predict the impinge point successfully in the case of a strong plunging breaker. In Figure 5.4 (b), the predicted undertow for non breaking region and transition region is far from the undertow near the bottom because one-dimensional model can not simulate near bottom velocity well in this region. Therefore, the depth-averaged undertow (from the bottom to the trough level) was estimated from the experimental data (triangles in Figure 5.4 (b)) to be compared with RBREAK2. These values were shown from A to D because the estimates of the depth-averaged undertow were not available due to the large amount of signal drop-outs in the inner surf and swash zone above  $z' > 1$  cm. However, in the inner surf and swash zone, the difference between depth-averaged undertow and undertow near the bottom is expected to be small. The undertow computed using RBREAK2 somewhat overpredicts the depth-averaged undertow from the experimental data from A to E (prior to the impinge point). In the inner surf and swash zone, the model results for the depth-averaged undertow give a good agreement with the undertow near the bottom estimated from the experiment shoreward of H. But, the model can not simulate the cross-shore variation of the mean horizontal velocity at the impinge point (from F to H).

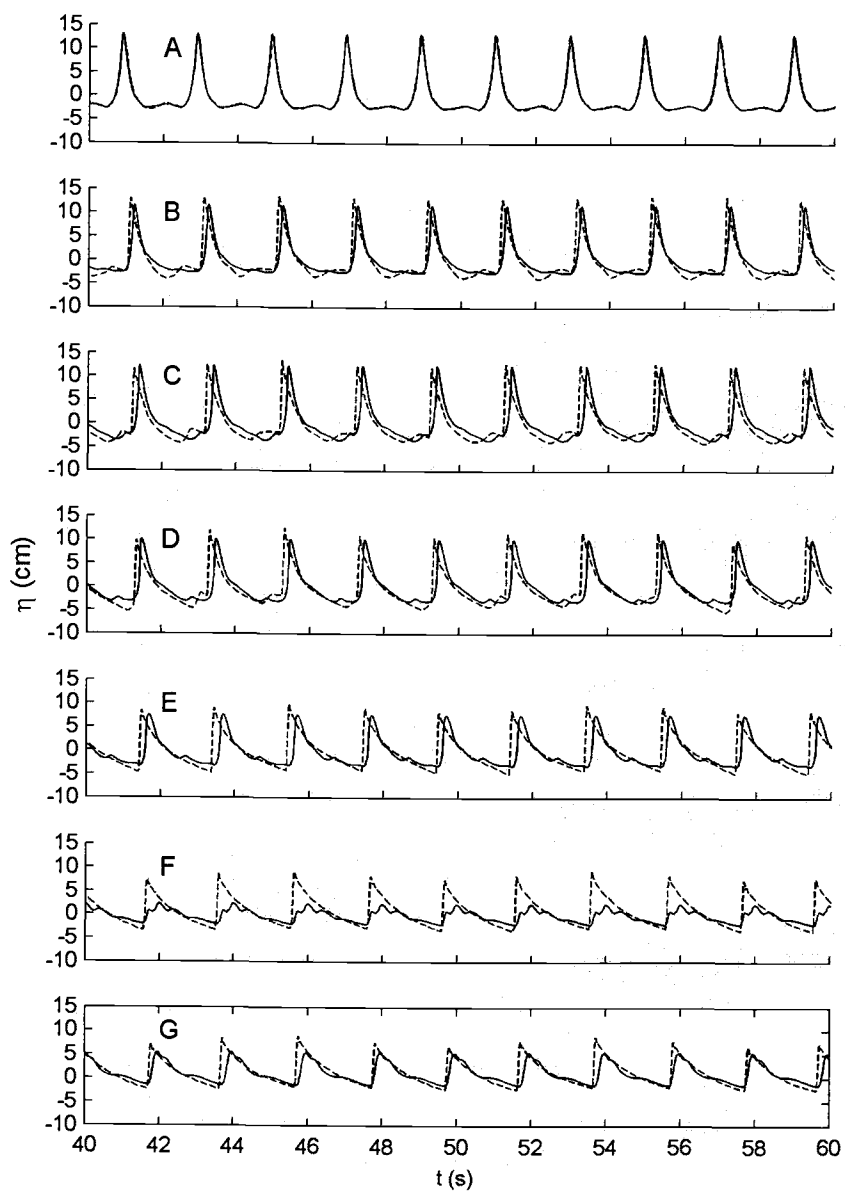


Figure 5.1 Comparisons of the free surface elevations calculated using RBREAK2 with the measured data from A to G. Solid lines are the measured data. Dashed lines are the simulated data.

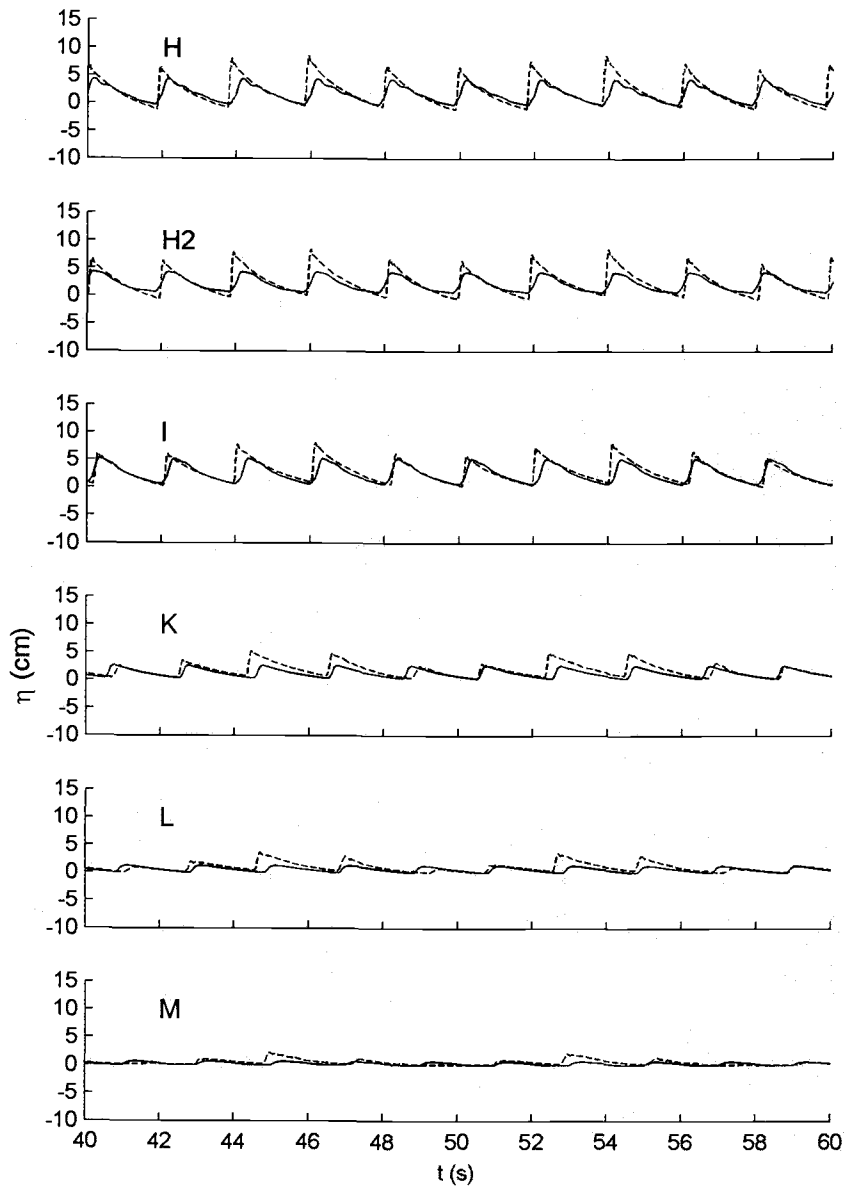


Figure 5.2 Comparisons of the free surface elevations calculated using RBREAK2 with the measured data from H to M. Solid lines are the measured data. Dashed lines are the simulated data.

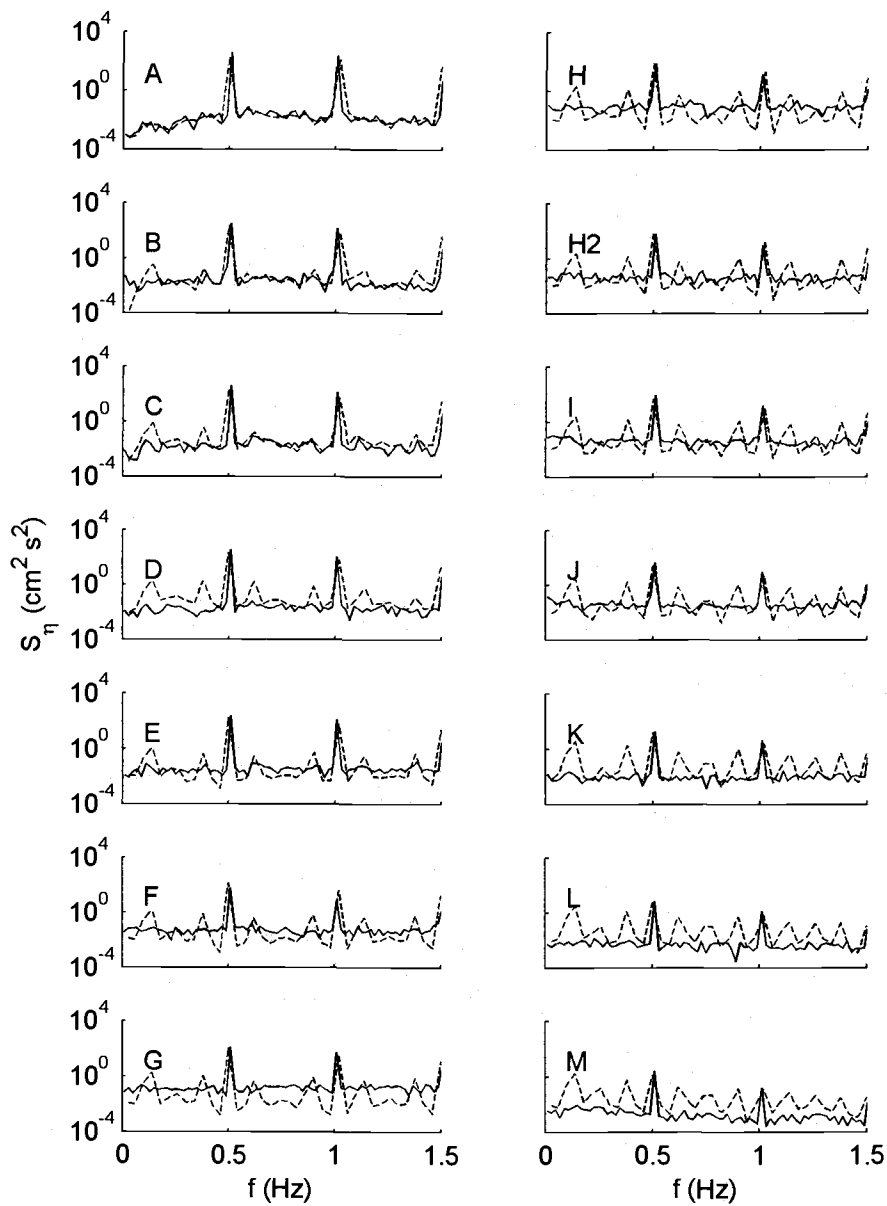


Figure 5.3 Comparisons of the free surface elevation spectra calculated using RBREAK2 with the experimental data. Solid lines are the spectra estimated from the experiments. Dashed lines are the spectra estimated from the RBREAK2.

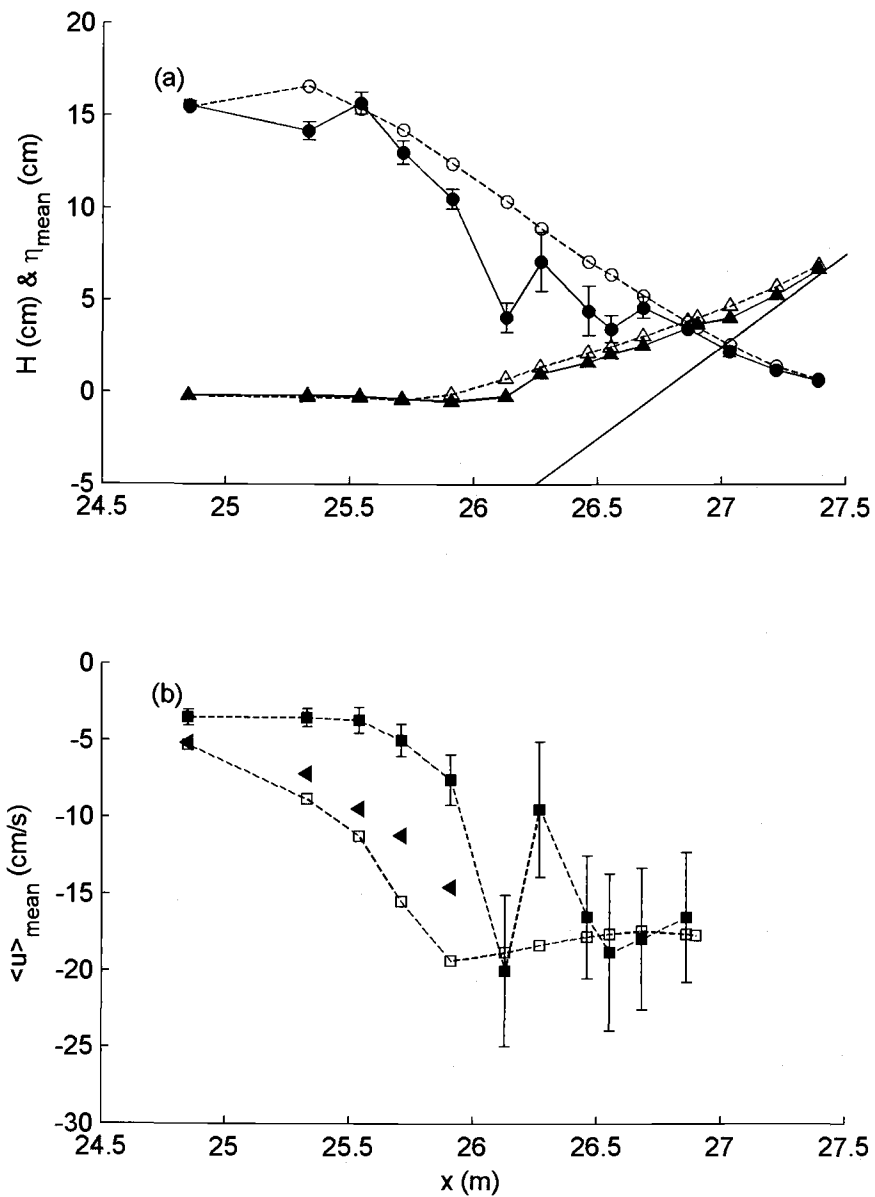


Figure 5.4 Comparisons of the wave height variation (circles) and setup (triangles) (a) and undertow ( $\langle u \rangle_{\text{mean}}$ ) near the bottom (squares) and depth-averaged undertow below the trough level (triangles) (b). Solid symbols are the measured data. Open symbols are the RBREAK2 results.

Figure 5.5 shows the model comparisons of the maximum, minimum, and mean ensemble averaged horizontal fluid velocities ( $\langle u \rangle_{\max}$ ,  $\langle u \rangle_{\min}$ , and  $\langle u \rangle_{\text{mean}}$ ) with those measured above the wave boundary layer at each cross-shore location. This figure shows that  $\langle u \rangle_{\max}$ ,  $\langle u \rangle_{\min}$ , and  $\langle u \rangle_{\text{mean}}$  were well predicted by RBREAK2 in the inner surf and swash zone, especially, in the swash zone where the turbulent bore was fully developed. Offshore of the surf zone (A and B),  $\langle u \rangle_{\max}$  was overpredicted by RBREAK2.

The skewness and asymmetry of the free surface elevation and horizontal fluid velocities near the bottom predicted by RBREAK2 were compared with those estimated from the measured data in Figure 5.6. In this figure, the skewness of the free surface elevation and ensemble averaged horizontal fluid velocities (wave velocity) were qualitatively predicted well. However, the asymmetry of the free surface elevation and the ensemble averaged horizontal fluid velocities was overpredicted in the surf and swash zone. This is because the shape of the free surface and the ensemble averaged horizontal fluid velocities computed using RBREAK2 were more like a saw-tooth wave than the measured data.

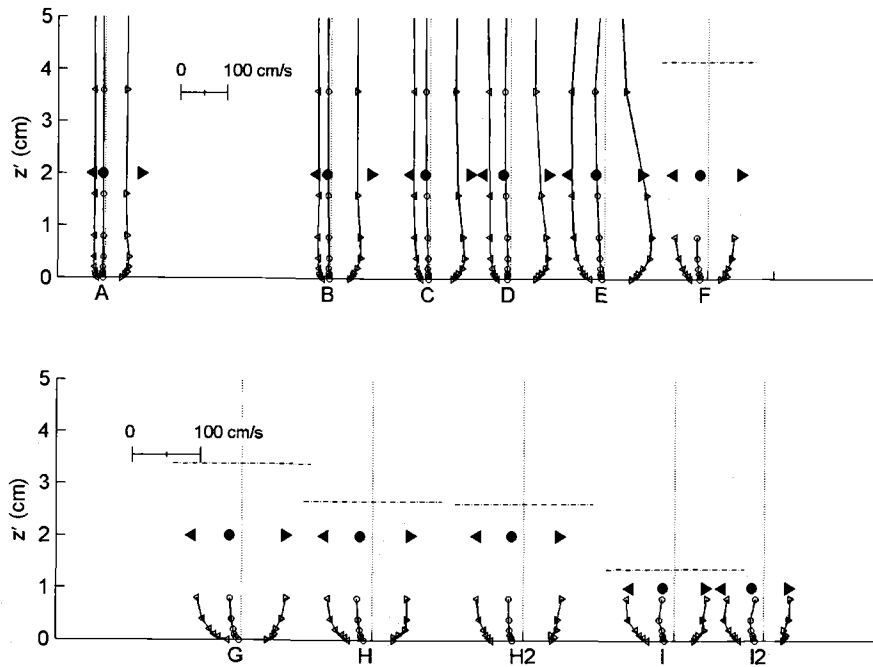


Figure 5.5 Comparisons of the mean, maximum, and minimum ensemble averaged horizontal fluid velocities calculated using RBREAK2 with the experimental data at each cross-shore location. Open symbols are the measured data. Solid symbols are the RBREAK2 results. Dashed line represents the trough level.

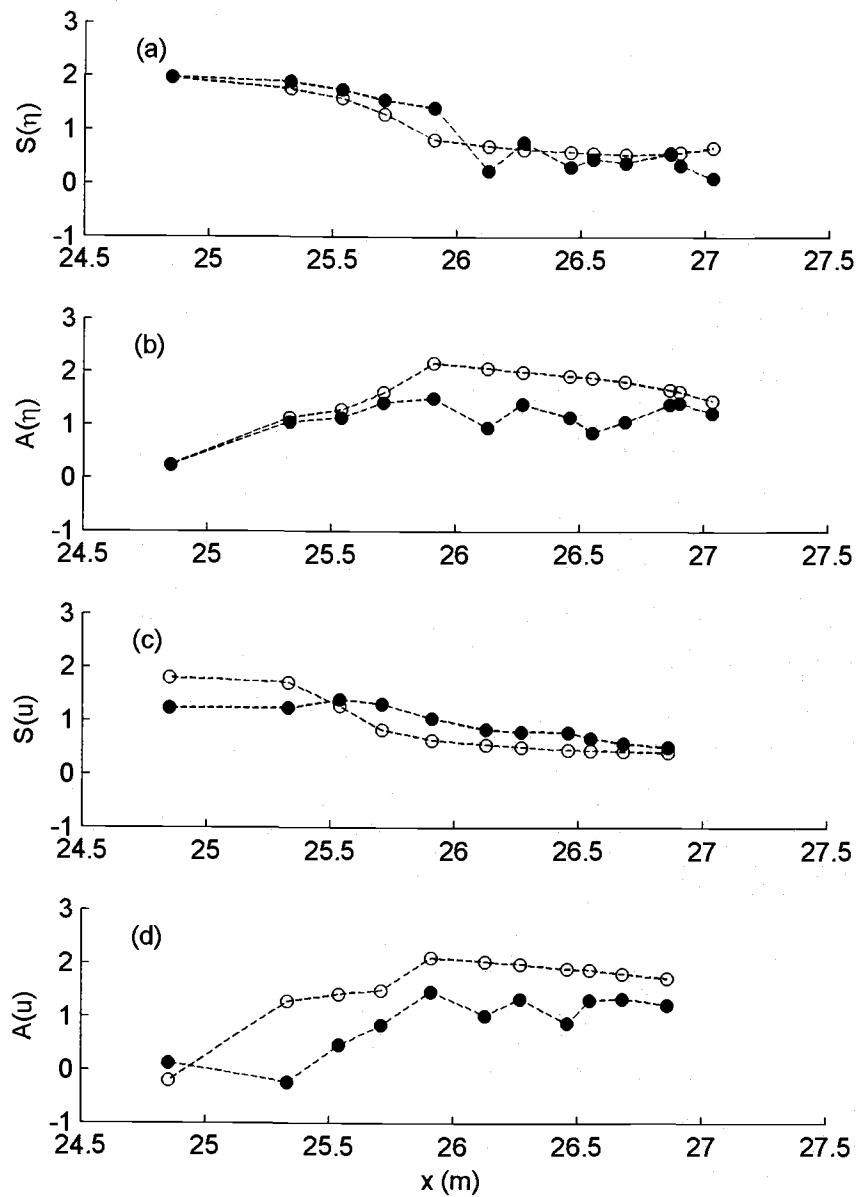


Figure 5.6 Comparison of the skewness and asymmetry of the free surface elevation and ensemble averaged horizontal fluid velocities near the bottom computed using RBREAK2 with the experimental data. Solid symbols are the measured data. Open symbols are the RBREAK2 results.  $S( )$  denotes skewness and  $A( )$  denotes asymmetry.

## 5.2 One-Dimensional Model II: FUNWAVE1D

FUNWAVE1D was developed by Kirby *et al.* (1998) and is based on the fully nonlinear Boussinesq equations derived by Wei *et al.* (1995). This model includes an eddy viscosity term to simulate energy dissipation due to wave breaking. Long and Kirby (2004) extended FUNWAVE1D and used the excess mass flux due to roller to predict undertow. The detail of roller geometry was suggested by Schäffer *et al.* (1993). The results gave good agreement with the field data. In the present study, the original FUNWAVE1D was employed to simulate the experimental data since extended FUNWAVE1D is not completely developed yet. The fully nonlinear Boussinesq equations are as follows:

$$\eta_t + \nabla \cdot \left\{ (h + \eta) \left[ u_\alpha + \left( z_\alpha + \frac{1}{2}(h + \eta) \nabla(\nabla \cdot (hu_\alpha)) \right) \right. \right. \\ \left. \left. + \left( \frac{1}{2}z_\alpha^2 - \frac{1}{6}(h^2 - h\eta + \eta^2) \right) \nabla(\nabla \cdot u_\alpha) \right] \right\} = 0 \quad (5.8)$$

$$u_{\alpha t} + (u_\alpha \cdot \nabla)u_\alpha + g\nabla\eta + z_\alpha \left\{ \frac{1}{2}z_\alpha \nabla(\nabla \cdot u_{\alpha t}) + \nabla(\nabla \cdot (hu_{\alpha t})) \right\} \\ + \nabla \left\{ \frac{1}{2}(z_\alpha^2 - \eta^2)(u_\alpha \cdot \nabla)(\nabla \cdot u_\alpha) + \frac{1}{2}[\nabla \cdot (hu_\alpha) + \eta \nabla \cdot u_\alpha]^2 \right\} \\ + \nabla \left\{ (z_\alpha - \eta)(u_\alpha \cdot \nabla)(\nabla \cdot (hu_\alpha)) - \eta \left[ \frac{1}{2}\eta \nabla \cdot u_{\alpha t} + \nabla \cdot (hu_{\alpha t}) \right]^2 \right\} = 0 \quad (5.9)$$

where  $u_\alpha$  is the horizontal velocity at reference elevation at  $z_\alpha$ .

FUNWAVE1D was initiated at the toe of the 1:35 slope using the measured data from the most offshore wave gage ( $x = 11.32$  m at the flat bottom), unlike the input condition used for RBREAK2. This was done because the wave generation did not work well using the free surface elevation measured at location A, which was too shallow and nonlinear. The bottom friction factor was set to 0.01, which was the same as the RBREAK2 input. Since waves broke further offshore in the model than in the experiment, the coefficient for the wave breaking scheme,  $cbkv$ , was adjusted to 0.55 empirically. This allowed wave breaking to be slightly delayed in the model. The manual suggested that the upper limit of the coefficient (0.65) gives optimal agreement for wave breaking on the planar beaches.

Figure 5.7 and Figure 5.8 show the FUNWAVE1D results for the free surface elevations along with the experimental data at each cross-shore location. The model slightly underpredicted the free surface elevation at A and overpredicted it at F, but agreed well in terms of the wave shape. This model also seemed to be unable to predict wave impinging at F. In the model, waves did not reach location L and M. Compared with the RBREAK2 results, the low frequency oscillation predicted by FUNWVAE1D was negligible (Figure 5.9).

The cross-shore variation of the wave height and setup is shown in Figure 5.10 (a). The model results agreed well in both cases even though wave breaking occurred slightly offshore and affected the setup. Figure 5.10 (b) shows the

undertow computed using the depth averaged horizontal fluid velocity from the original FUNWAVE1D. The comparison shows that FUNWAVE1D predicts the undertow well seaward of breaking (A to C). Agreement worsens through the breaking region (D to H), and FUNWAVE1D fails to capture the cross-shore variation of the undertow landward of the second impinge point and through the swash region (H2 to M). The model gives poor agreement in the swash zone, indicating the limitation of the slot technique to provide realistic mean velocities in this region. It is noted that an ad hoc roller model (e.g. Long *et al.*, 2004) may improve the comparisons somewhat, although this data set is for a strong plunging breaker rather than a mildly spilling wave with a well-established surf zone. Figure 5.11 shows that the prediction of ensemble averaged horizontal fluid velocities was good for both non breaking and breaking waves, from locations A to D. However, for broken waves in the inner surf and swash zone (E – K), the model did not estimate these quantities well when compared with the experimental data.

The cross-shore variation of the skewness and asymmetry of the free surface elevations and horizontal fluid velocities modeled by FUNWAVE1D were compared with the measured data in Figure 5.12. The results show that the model results agree well with those estimated from the experimental data. The skewness of the free surface elevation was underpredicted from locations A to C, but predicted well in the inner surf and swash zone.

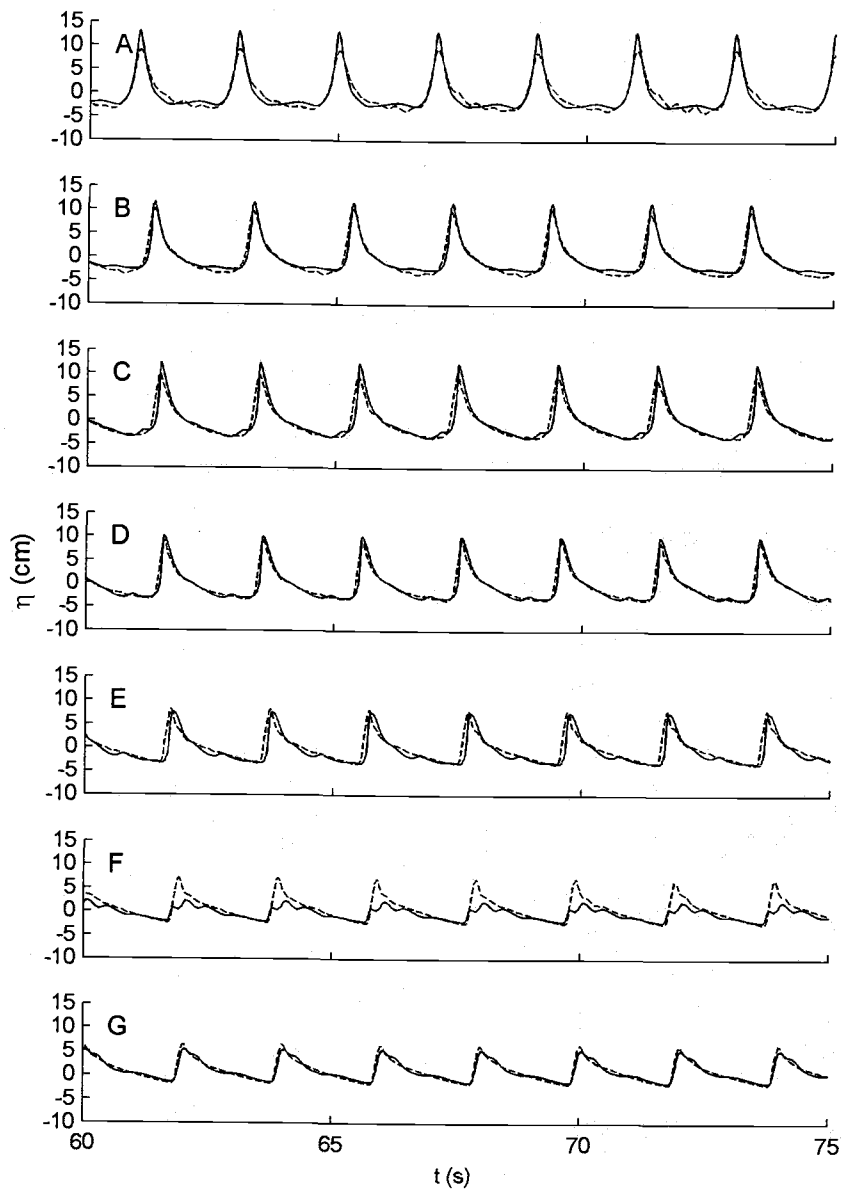


Figure 5.7 Comparison of the free surface elevations calculated by FUNWAVE1D with the measured data from A to G. Solid lines are the measured data. Dashed lines are the simulated data.

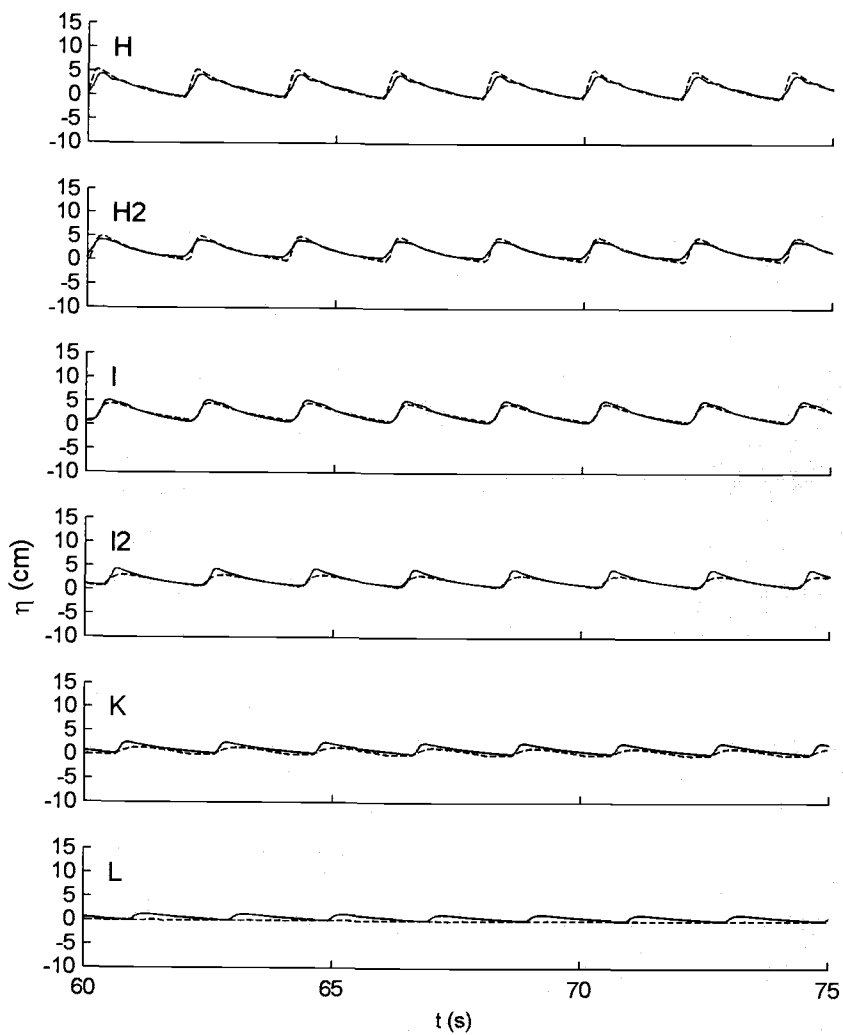


Figure 5.8 Comparison of the free surface elevations calculated by FUNWAVE1D with the measured data from H to L. Solid lines are the measured data. Dashed lines are the simulated data.

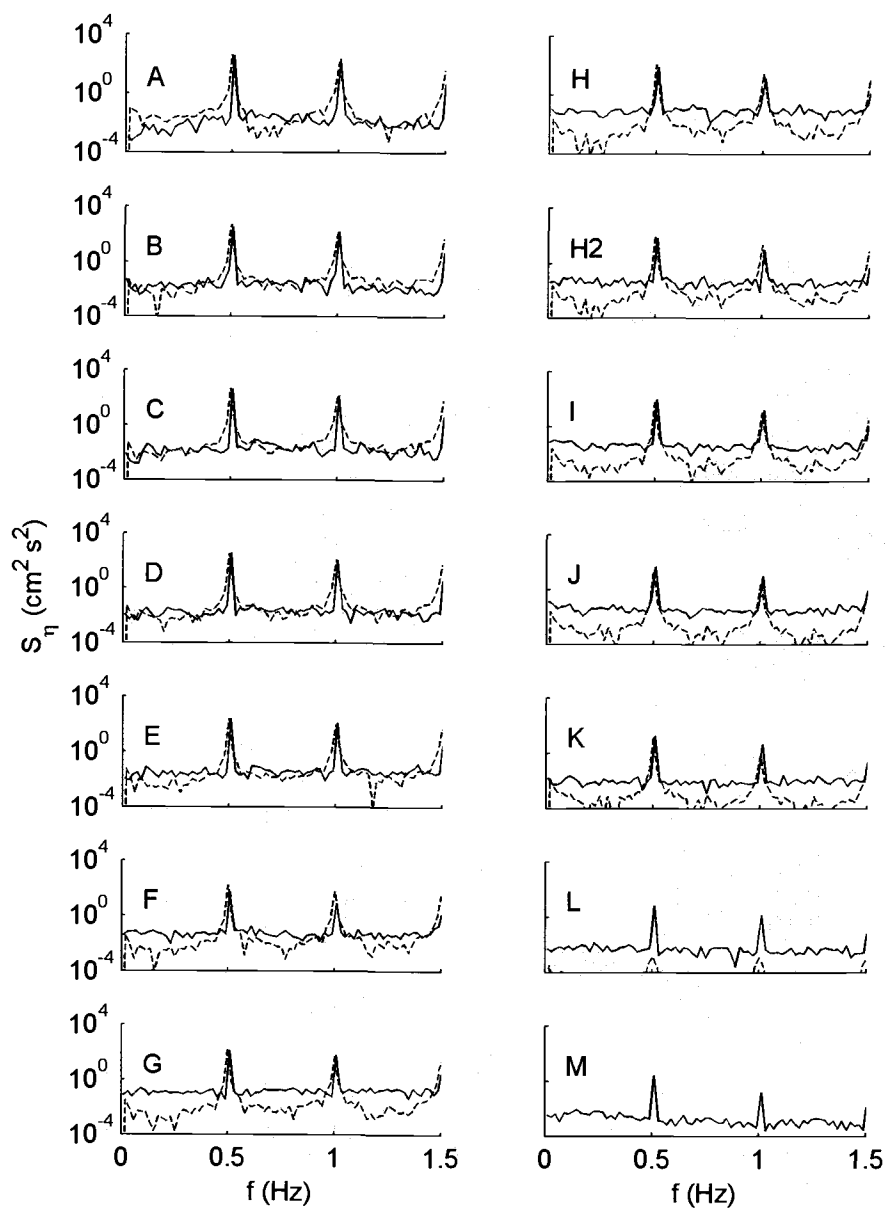


Figure 5.9 Comparison of the free surface elevation spectra with the experimental data. Solid lines are the spectra estimated from the experiment. Dashed lines are the FUNWAVE1D results.

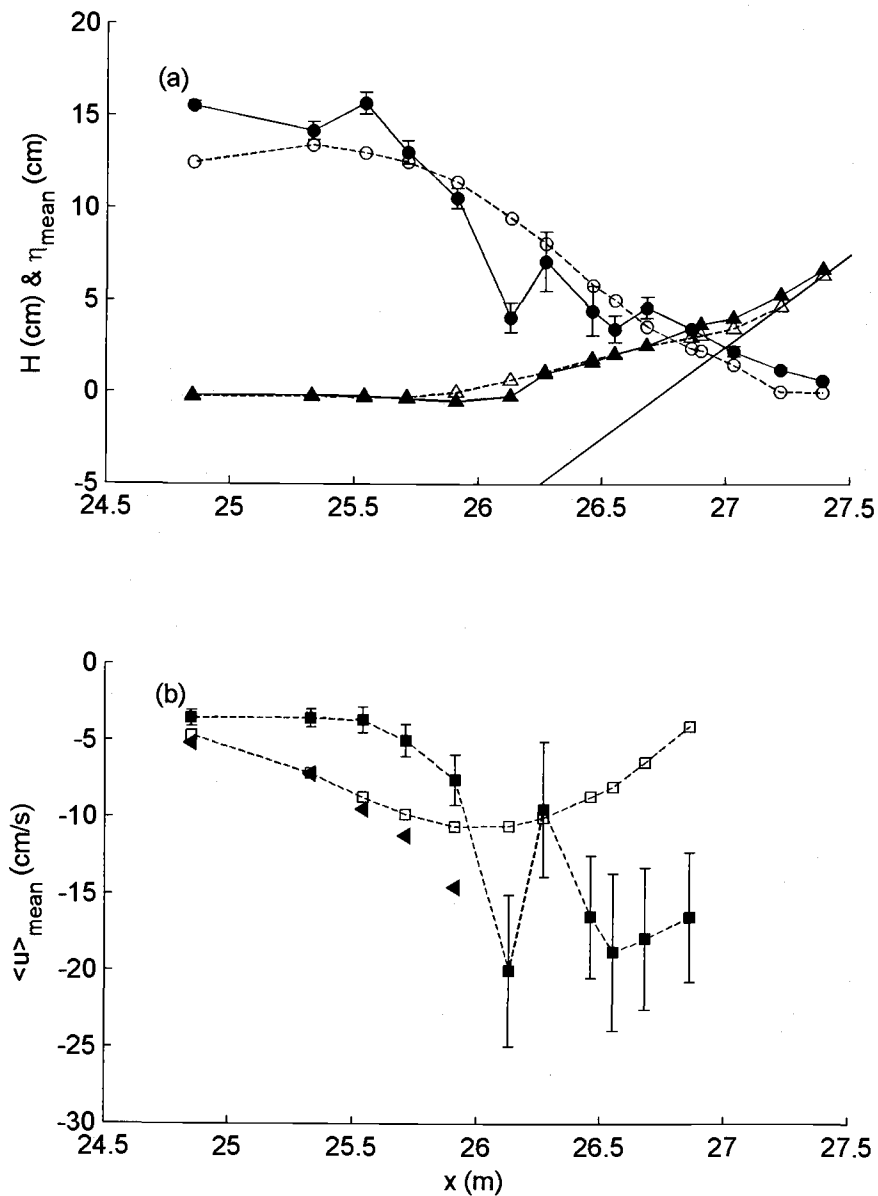


Figure 5.10 Comparison of the wave height variation (circles) and setup (triangles) (a), and undertow near the bottom (squares) and depth-averaged undertow (triangles, below the trough level) (b). Black colored symbols are the measured data. Solid symbols are the measured data. Open symbols are the FUNWAVE1D results.

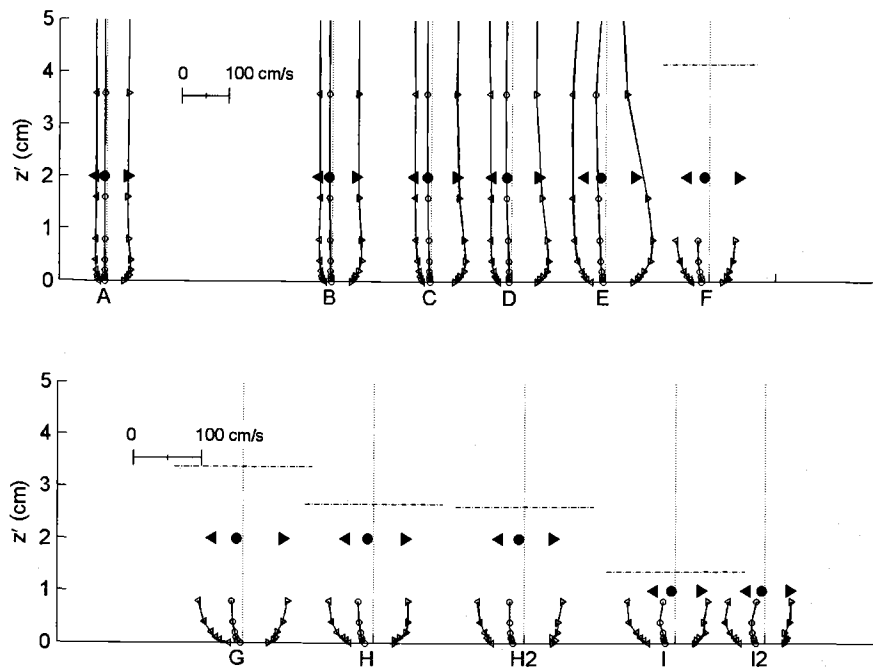


Figure 5.11 Comparison of the mean, maximum, and minimum ensemble averaged horizontal fluid velocities with the experimental data at each cross-shore location. Open symbols are the measured data. Solid symbols are the FUNWAVE1D results.

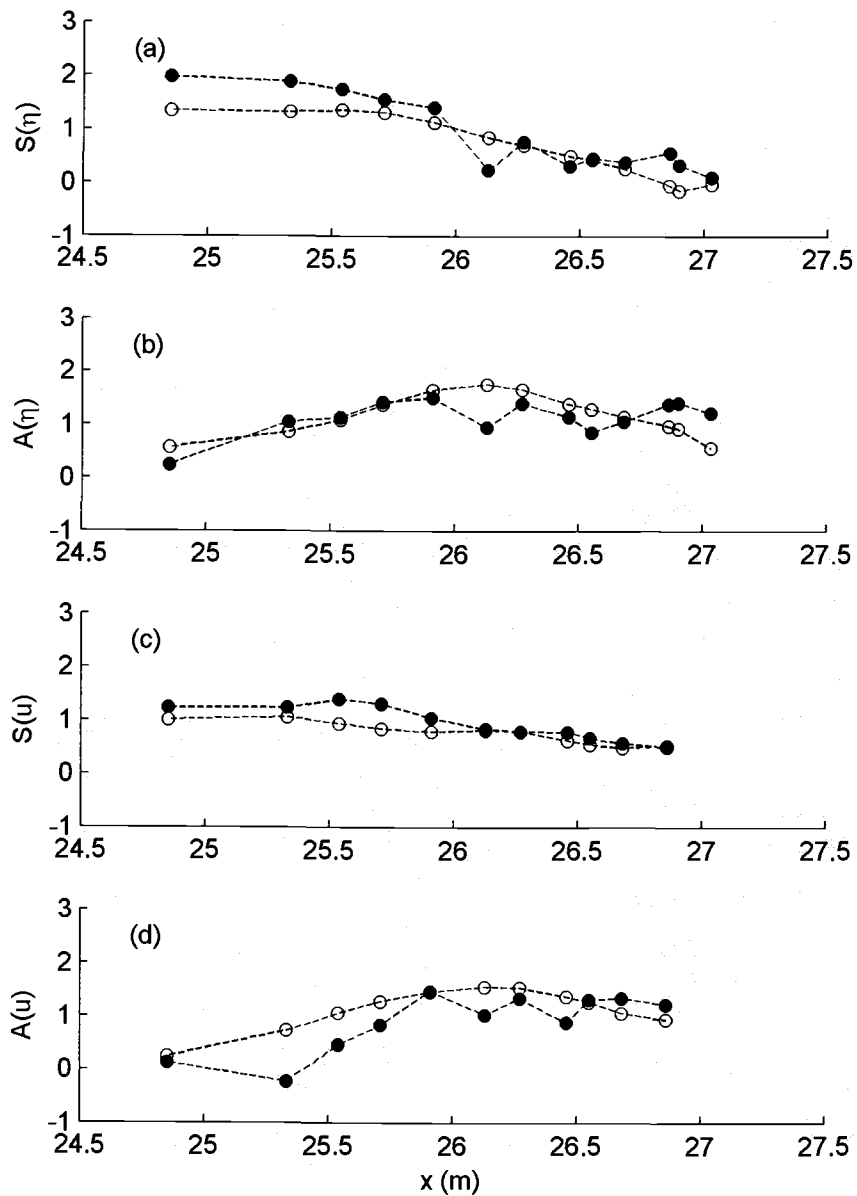


Figure 5.12 Comparison of the skewness and asymmetry of the free surface elevation and ensemble averaged horizontal fluid velocities near the bottom. Solid symbols are the measured data. Open symbols are the FUNWAVE1D results.  $S()$  denotes skewness and  $A()$  denotes asymmetry.

### 5.3 Two-Dimensional Model: COBRAS

COBRAS (Cornell BReAking Wave and Structure) was developed by Lin and Liu (1998) and is based on the Reynolds Averaged Navier-Stokes (RANS) equations with a modified  $k-\varepsilon$  model for turbulent flows. Since this is a two-dimensional numerical model, it has been tested to simulate turbulence and vorticity for breaking wave cases such as the surf zone.

The RANS equations are introduced as follows:

$$\frac{\partial \langle u_i \rangle}{\partial x_i} = 0 \quad (5.10)$$

$$\frac{\partial \langle u_i \rangle}{\partial t} + \langle u_j \rangle \frac{\partial \langle u_i \rangle}{\partial x_j} = -\frac{1}{\langle \rho \rangle} \frac{\partial \langle p \rangle}{\partial x_i} + g_i + \frac{1}{\langle \rho \rangle} \frac{\partial \langle \tau_{ij} \rangle}{\partial x_j} - \frac{\partial \langle u'_i u'_j \rangle}{\partial x_j} \quad (5.11)$$

where  $\langle \rangle$  denotes mean quantities (time averaged components and wave components) and a prime denotes turbulent fluctuations.

The Reynolds stress term,  $\partial \langle u'_i u'_j \rangle$  is modeled using a nonlinear eddy viscosity model,

$$\begin{aligned}
\langle u'_i u'_j \rangle &= \frac{2}{3} k \delta_{ij} - C_d \frac{k^2}{\varepsilon} \left( \frac{\partial \langle u_i \rangle}{\partial x_j} + \frac{\partial \langle u_j \rangle}{\partial x_i} \right) \\
&\quad - \frac{k^3}{\varepsilon^2} \left[ C_1 \left( \frac{\partial \langle u_i \rangle}{\partial x_l} \frac{\partial \langle u_l \rangle}{\partial x_j} + \frac{\partial \langle u_j \rangle}{\partial x_l} \frac{\partial \langle u_l \rangle}{\partial x_i} \right. \right. \\
&\quad \left. \left. - \frac{2}{3} \frac{\partial \langle u_l \rangle}{\partial x_k} \frac{\partial \langle u_k \rangle}{\partial x_l} \delta_{ij} \right) \right. \\
&\quad \left. + C_2 \left( \frac{\partial \langle u_i \rangle}{\partial x_k} \frac{\partial \langle u_j \rangle}{\partial x_k} - \frac{\partial \langle u_l \rangle}{\partial x_k} \frac{\partial \langle u_l \rangle}{\partial x_k} \delta_{ij} \right) \right. \\
&\quad \left. + C_3 \left( \frac{\partial \langle u_k \rangle}{\partial x_i} \frac{\partial \langle u_k \rangle}{\partial x_j} - \frac{\partial \langle u_l \rangle}{\partial x_k} \frac{\partial \langle u_l \rangle}{\partial x_k} \delta_{ij} \right) \right] \quad (5.12)
\end{aligned}$$

where  $k$  is the turbulent kinetic energy, and  $\varepsilon$  is the turbulence dissipation rate, and  $C_d, C_1, C_2, C_3$  are empirical coefficients.  $k$  and  $\varepsilon$  were obtained using the modified  $k - \varepsilon$  model,

$$\frac{\partial k}{\partial t} + \langle u_j \rangle \frac{\partial k}{\partial x_j} = \frac{\partial}{\partial x_j} \left[ \left( \frac{\nu_t}{\sigma_k} + \nu \right) \frac{\partial k}{\partial x_j} \right] - \langle u'_i u'_j \rangle \frac{\partial \langle u_i \rangle}{\partial x_j} - \varepsilon \quad (5.13)$$

$$\frac{\partial \varepsilon}{\partial t} + \langle u_j \rangle \frac{\partial \varepsilon}{\partial x_j} = \frac{\partial}{\partial x_j} \left[ \left( \frac{\nu_t}{\sigma_\varepsilon} + \nu \right) \frac{\partial \varepsilon}{\partial x_j} \right] + C_{1\varepsilon} \frac{\varepsilon}{k} \nu_t \left( \frac{\partial \langle u_i \rangle}{\partial x_j} + \frac{\partial \langle u_j \rangle}{\partial x_i} \right) \frac{\partial \langle u_i \rangle}{\partial x_j} - C_{2\varepsilon} \frac{\varepsilon^2}{k} \quad (5.14)$$

where  $\nu_t = C_d k^2 / \varepsilon$ . The coefficients in equations (5.11) and (5.12) were used as defined in Lin and Liu (1998). The free surface motion was predicted using the volume-of-fluid (VOF) method.

The model domain for COBRAS consisted of the entire wave flume. Since no wave absorption system existed on the wave maker in the actual wave flume, the waves were also generated using a wavemaker in the model. A variable grid size was introduced with coarser grids (5 cm  $\times$  0.6 cm) on the flat bottom section and a gradually decreasing grid size (2.5 cm  $\times$  0.6 cm) near the LDV measurement area. The grain size on the bottom was set to 2.2 mm. Stokes 2<sup>nd</sup> order waves were generated for 200 s and analyzed 100 s after wave generation in order to reduce transitional effects. Data for locations A-M were output from the model with the exception of location H2.

In the present model comparison, two different types of modified  $k - \varepsilon$  models were used to estimate the turbulent parameters: (1) a nonlinear eddy viscosity model in equation 5.10; (2) a renormalized group (RNG) method associated with a nonlinear model by allowing  $C_{2\varepsilon}$  in equation 5.12 to vary with the fluid strain rate (Yakhot *et al.*, 1992).

Figure 5.13 shows the example of the velocity vector field and TKE computed using COBRAS with the nonlinear eddy viscosity model. This figure clearly shows that the model simulate the first and second impinge points (the second panel and the fifth panel from the top). The water surface elevations at each cross-shore measurement location were modeled using COBRAS and shown in

Figure 5.14 to Figure 5.17. In Figure 5.14 and Figure 2.2, the waves at location A are smaller in both models when compared to the experimental data. This is because  $k - \varepsilon$  type models overpredict the turbulence level and predict lower breaking wave heights, as shown in the previous studies (Lin and Liu, 1998; Bradford, 2000). However, the model may be able to predict the hydrodynamics at the impinge point. The model seemed to simulate the impinge point at E, which is farther offshore than the data measured during this experiment. COBRAS well predicted the free surface elevations in the inner surf and swash zone. However, in Figure 5.14, the free surface elevations modeled using COBRAS with a nonlinear eddy viscosity model had phase lags from the measured data in the swash zone (I – L). This effect was decreased in the results simulated using COBRAS with a RNG model.

Figure 5.18 shows the spectral comparisons of the free surface elevations using COBRAS with the spectra estimated in the experiment. The results show that the low frequency oscillation effects in the model are small and predicted well. The cross-shore variation of wave heights and setup modeled by COBRAS were compared with those calculated from the measured data in Figure 5.19 (a). The model results with both turbulence closure models gave similar trends in wave height and setup but the wave height prediction at location A was slightly better using RNG method. On the other hand, in Figure 5.19 (b), the model using nonlinear eddy viscosity predicted slightly better at the impinge point.

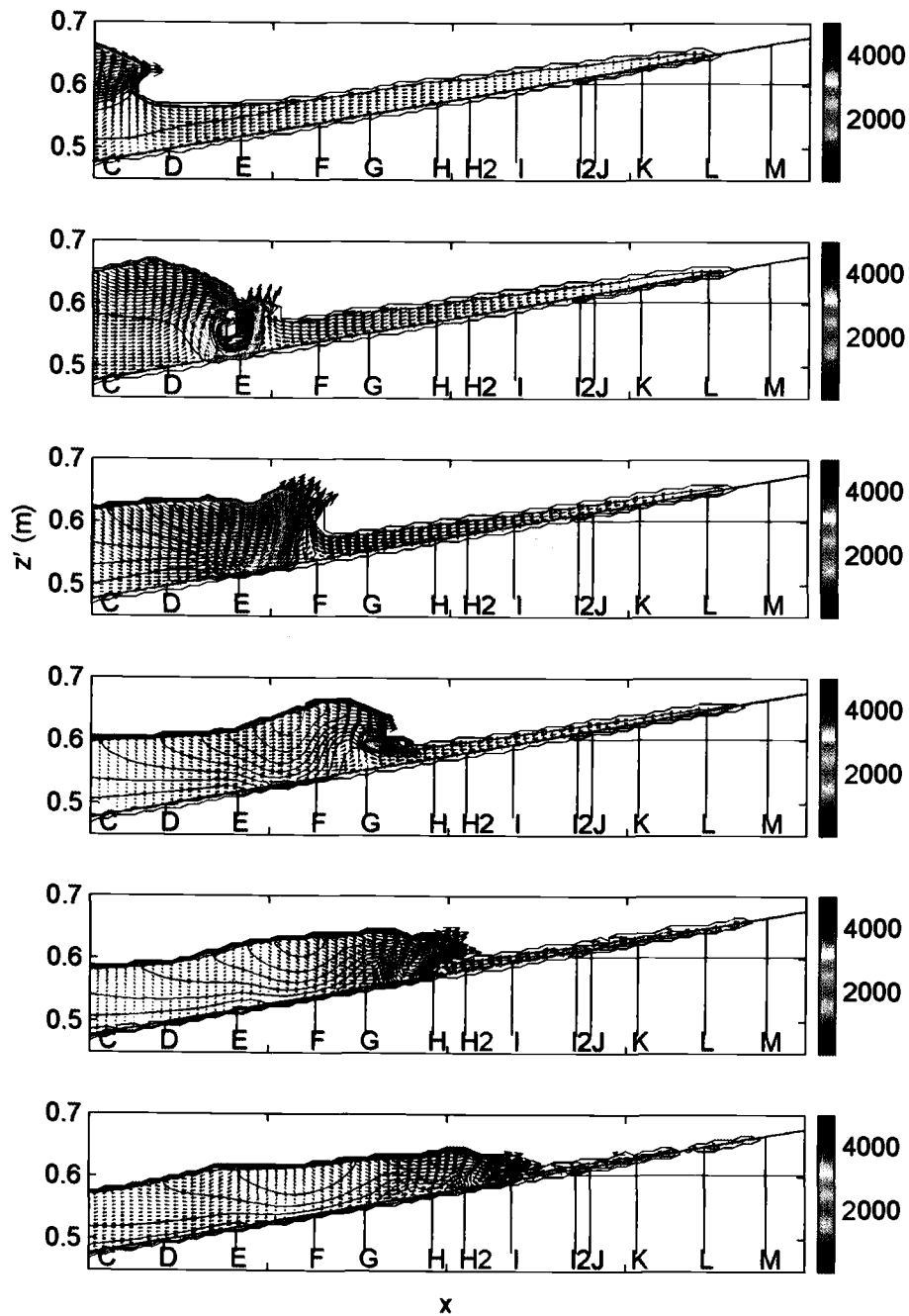


Figure 5.13 Simulation of vector field and TKE contour using COBRAS with the nonlinear eddy viscosity model at several time steps.

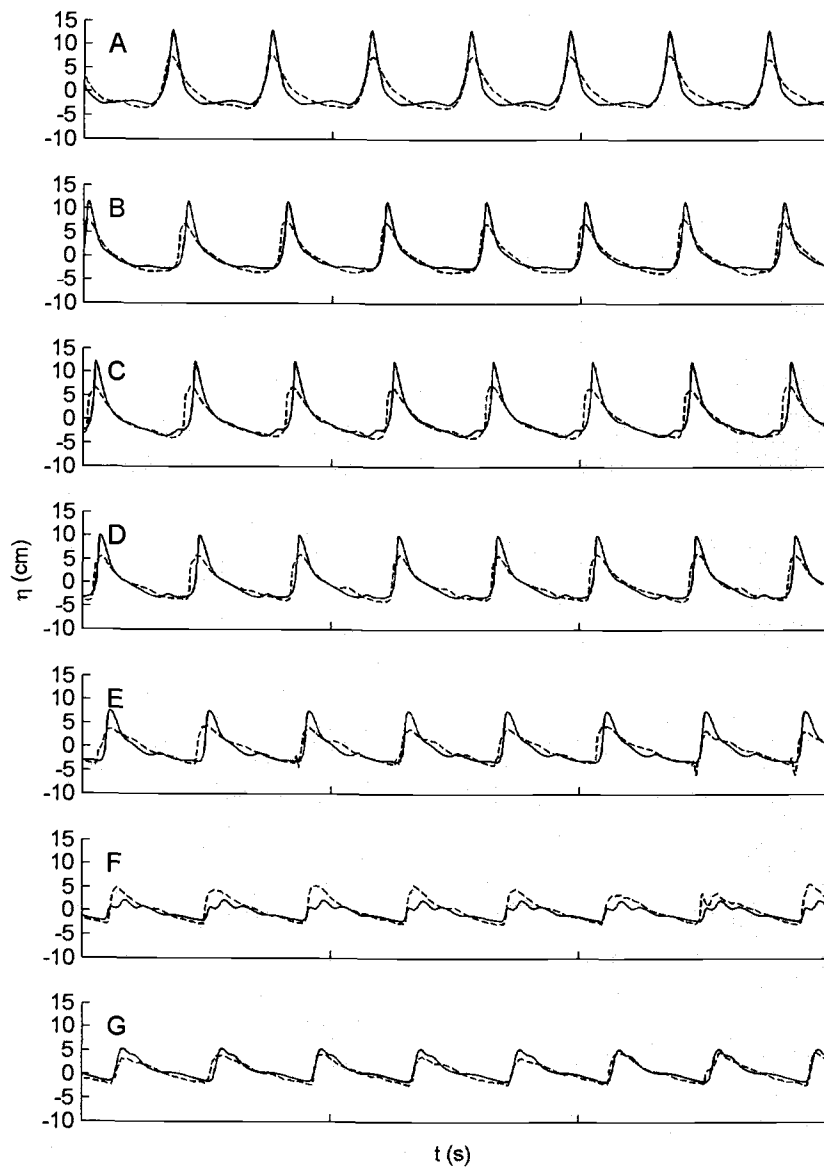


Figure 5.14 Comparison of the free surface elevations calculated using COBRAS (nonlinear eddy viscosity model) with the measured data from A to G. Solid lines are the measured data. Dashed lines are the simulated data.

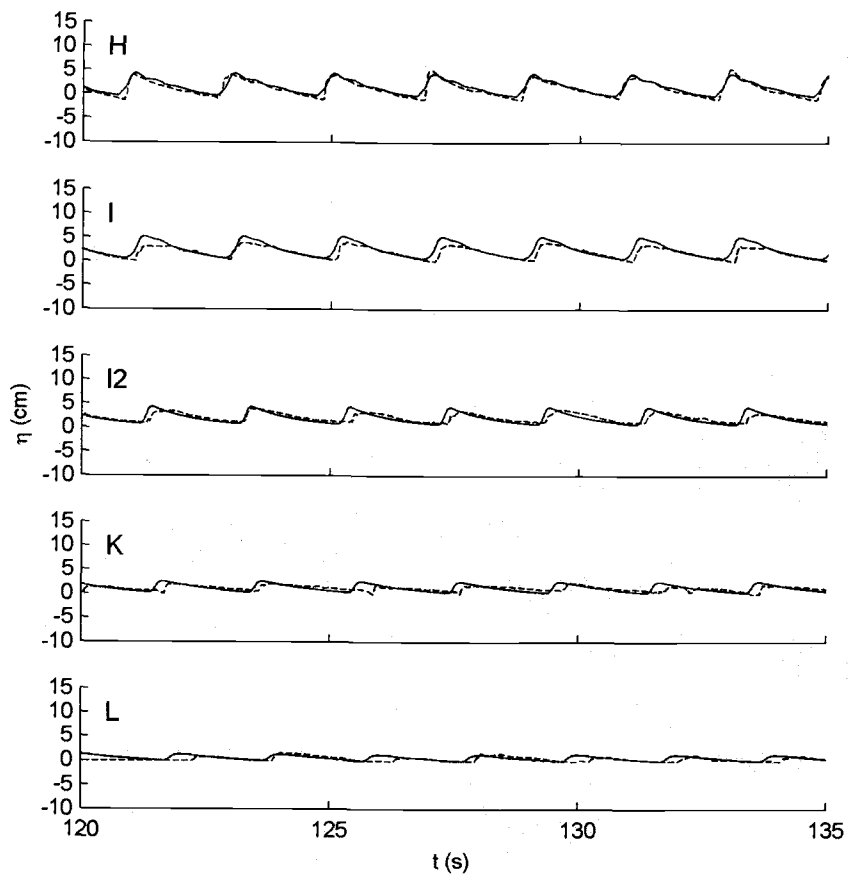


Figure 5.15 Comparison of the free surface elevations calculated using COBRAS (nonlinear eddy viscosity model) with the measured data from H to L. Solid lines are the measured data. Dashed lines are the simulated data.

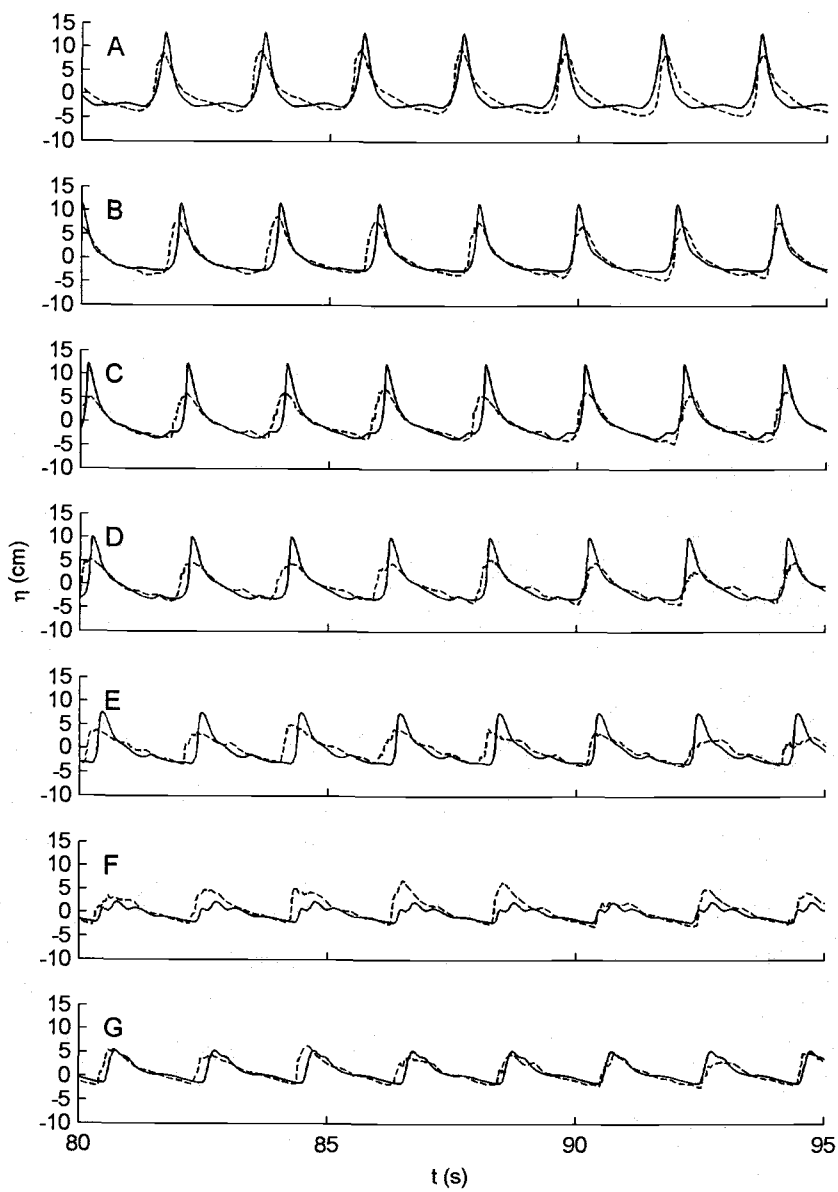


Figure 5.16 Comparison of the free surface elevations calculated using COBRAS (RNG model) with the measured data from A to G. Solid lines are the measured data. Dashed lines are the simulated data.

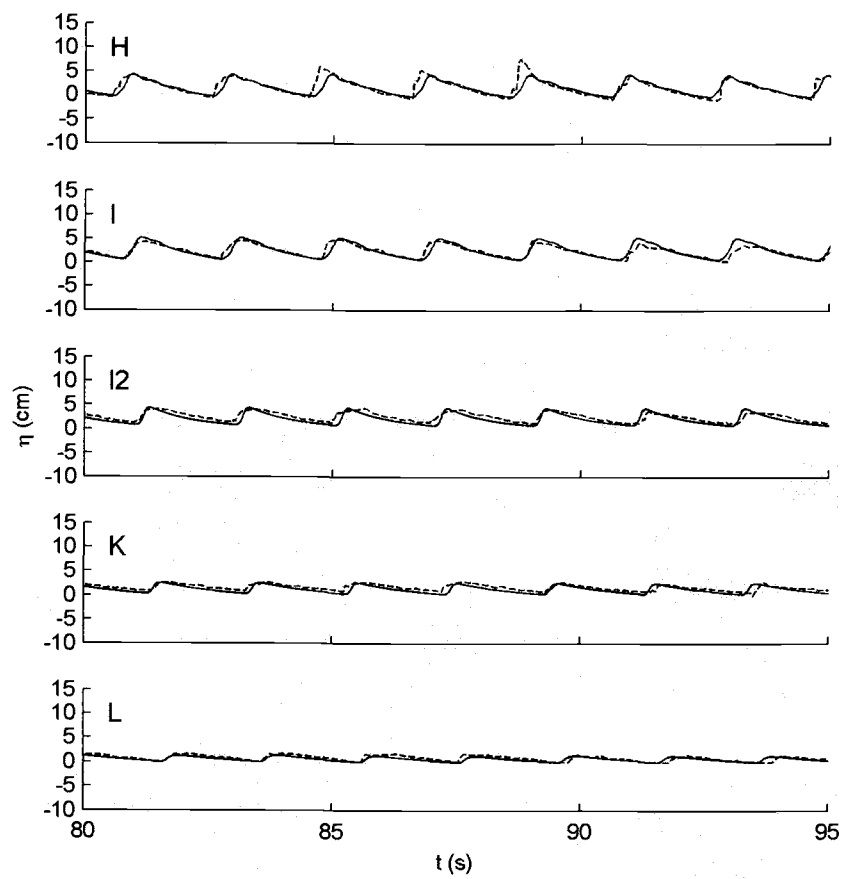


Figure 5.17 Comparison of the free surface elevations calculated using COBRAS (RNG model) with the measured data from H to L. Solid lines are the measured data. Dashed lines are the simulated data.

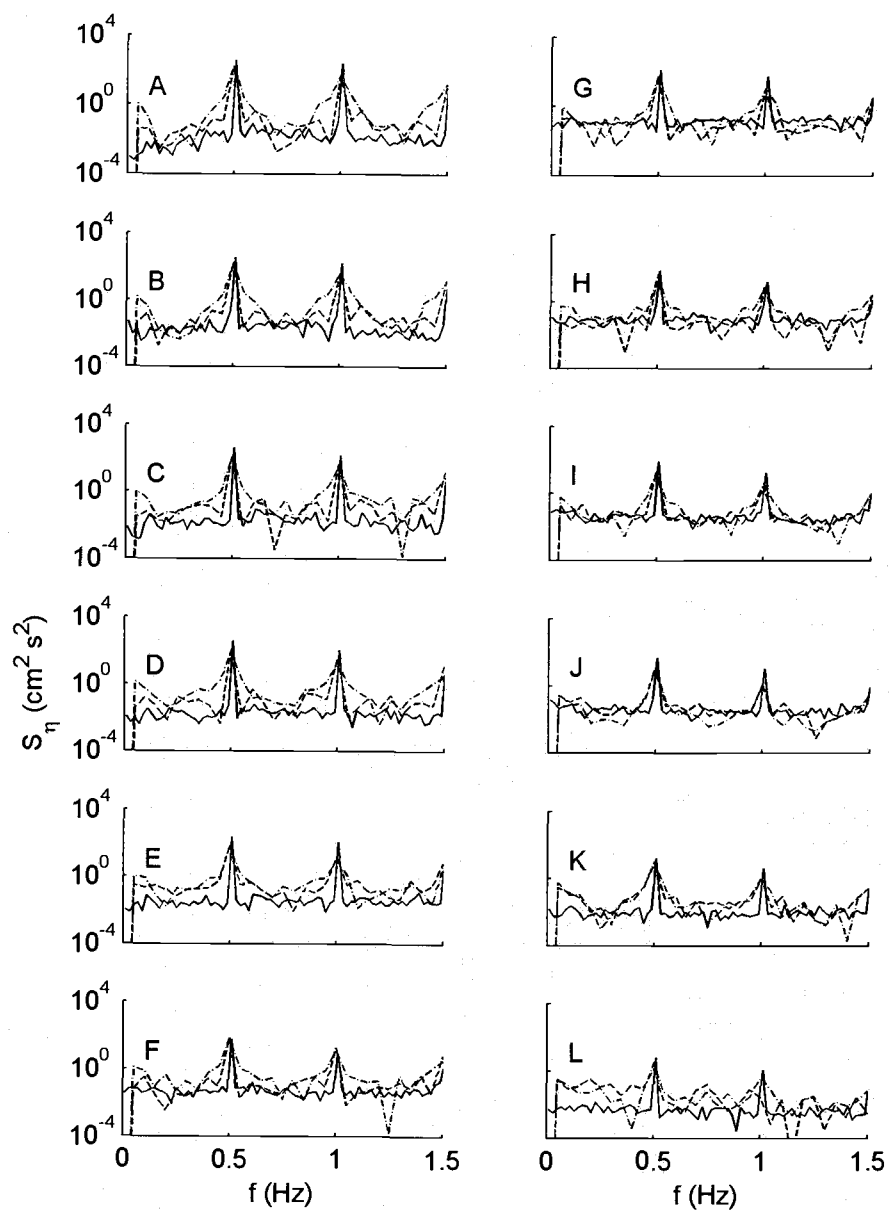


Figure 5.18 Comparison of the free surface elevation spectra with the experimental data. Solid lines are the spectra estimated from the experiment. Dashed lines are the COBRAS results using the nonlinear eddy viscosity model. Dash-dot lines are the COBRAS results using the RNG model.

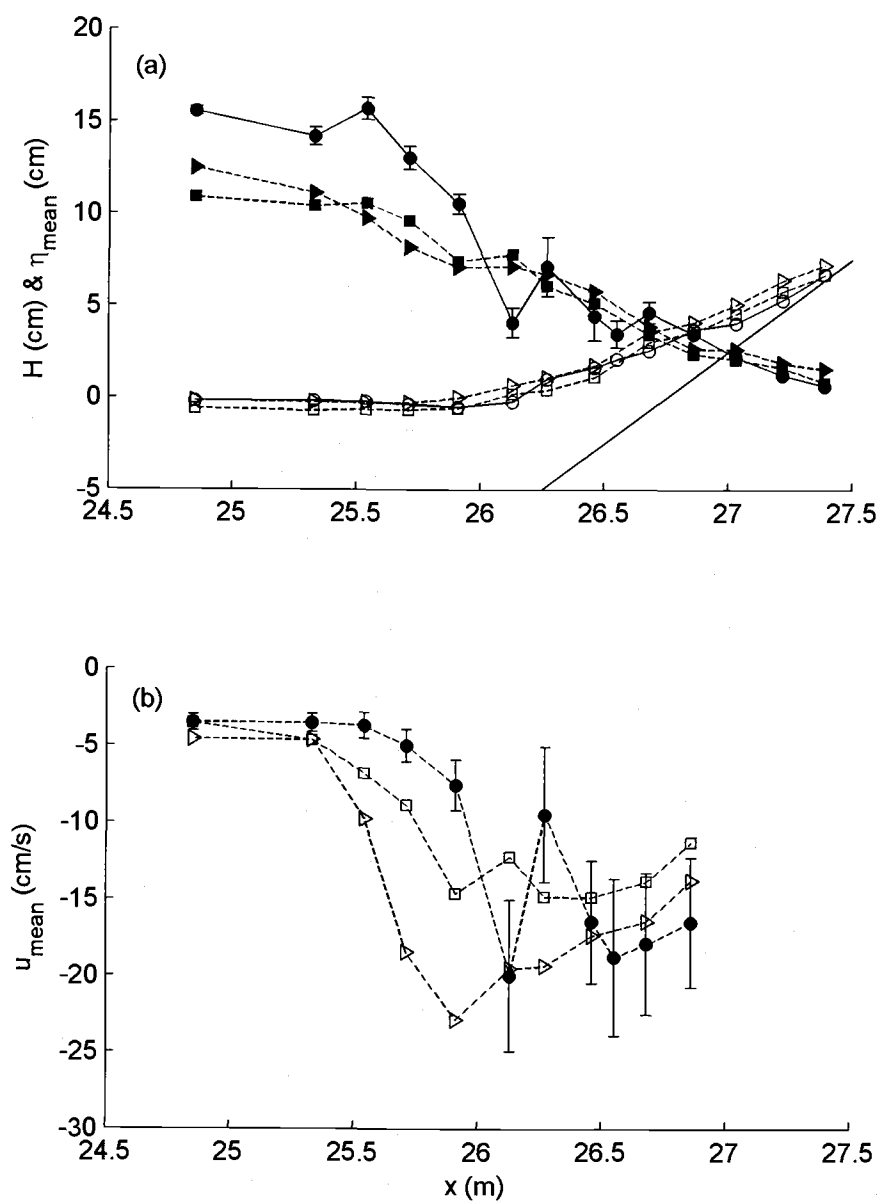


Figure 5.19 Comparison of the variation of the wave height (solid) (a) and setup (open) (b), and undertow (solid circles: the experimental data; open squares: nonlinear eddy viscosity model; open triangle: RNG model) near the bottom (c) calculated using COBRAS with the measured data. Circles are the experimental data. Squares are from the nonlinear eddy viscosity model. Triangles are from the RNG model.

Figure 5.20 shows the comparison of the skewness and asymmetry of the free surface and horizontal fluid velocities at each cross-shore location. The model underpredicted the skewness of the free surface elevations in the outer surf zone and wave breaking region, while the model accurately predicted it in the inner surf and swash zone. The skewness of the horizontal fluid velocity near the bottom was also underpredicted similar to the skewness of the free surface elevations.

Figure 5.21 and Figure 5.22 show the model comparisons of the vertical profiles of the maximum, minimum, and mean ensemble averaged horizontal fluid velocities ( $\langle u \rangle_{\max}$ ,  $\langle u \rangle_{\min}$ , and  $\langle u \rangle_{\text{mean}}$ ) at each cross-shore location. In these figures, both models predicted  $\langle u \rangle_{\min}$  and  $\langle u \rangle_{\text{mean}}$  with good agreement but the results using RNG model were slightly better in the swash zone. The estimates of  $\langle u \rangle_{\max}$  using both turbulence closure models were underpredicted, especially in the inner surf zone where the horizontal fluid velocities near the bottom were large. Moreover, the vertical structures of  $\langle u \rangle_{\max}$ ,  $\langle u \rangle_{\min}$ , and  $\langle u \rangle_{\text{mean}}$  near the bottom were not predicted well. Therefore, the finer vertical grid resolutions are recommended for better estimates of the boundary layer processes in the inner surf and swash zone.

The cross-shore variation of TKE estimated by the model was compared with the experimental estimates in Figure 5.23. The model results from both

turbulence closure models had a maximum TKE at E, while the maximum TKE from the experimental results was at F. Since the model predicted the impinge point at E, these results are reasonable when compared to the experimental results in this study. In this figure, TKE estimated using the nonlinear eddy viscosity model was much larger than the TKE estimated from the experimental data. The TKE estimates from the RNG method were much closer to the experimental estimates.

Table 5.1 shows the  $r^2$  values between the results estimated from the experiment and those computed using numerical models. In this table, most of the  $r^2$  values were higher in RBREAK2 and FUNWAVE1D than in COBRAS. This is because COBRAS predicted the wave breaking point further offshore than the experimental, RBREAK2 and FUNWAVE1D results. However, COBRAS qualitatively predicted the hydrodynamics at the impinge points better than the one-dimensional model.

Table 5.1  $r^2$  values between the experimental results and the numerical model results.

	RBREAK2	FUNWAVE1D	COBRAS (RNG)	COBRAS (NEV)
$H$	0.90	0.86	0.86	0.88
$\bar{\eta}$	0.94	0.83	0.85	0.85
$\langle u \rangle_{\text{mean}}$	0.49	0.00	0.23	0.48
$S(\eta)$	0.83	0.75	0.61	0.51
$A(\eta)$	0.57	0.18	0.00	0.29
$S(u)$	0.60	0.76	0.33	0.21
$A(u)$	0.47	0.50	0.48	0.50

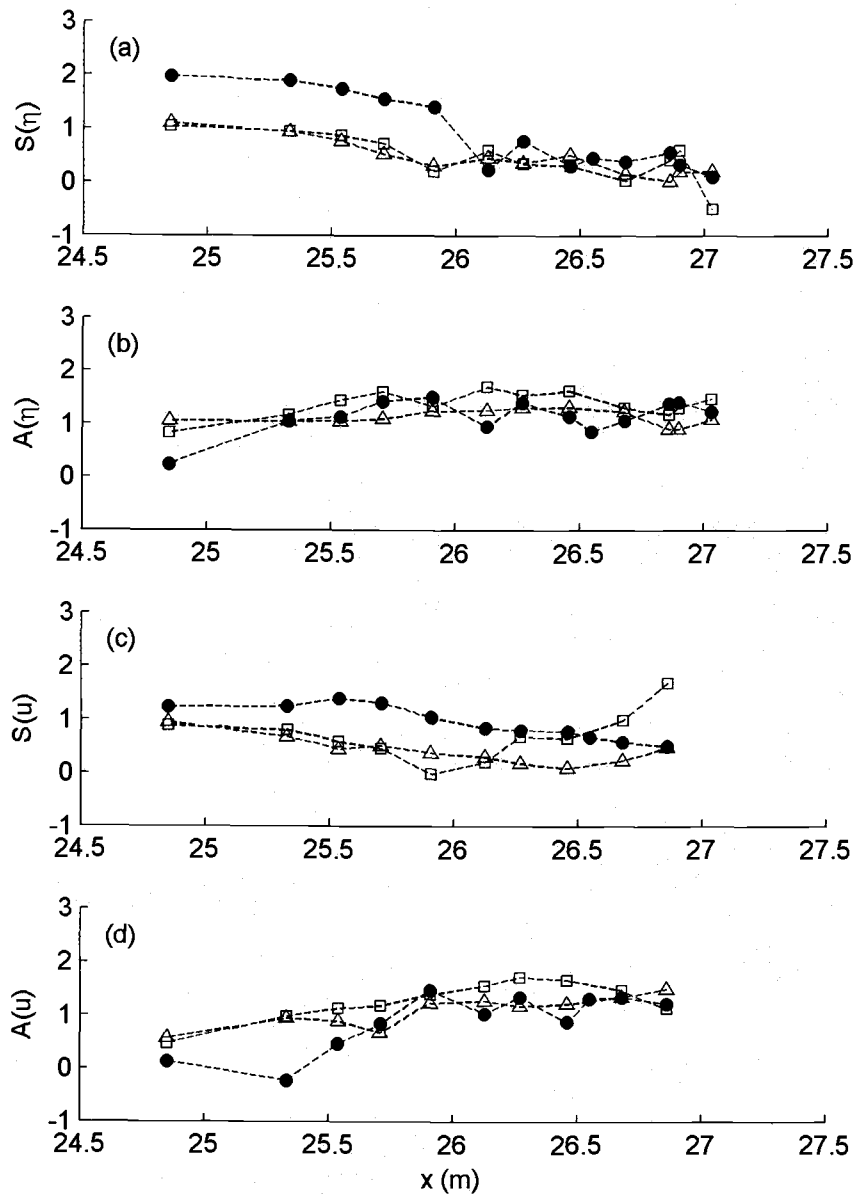


Figure 5.20 Comparison of the skewness and asymmetry of the free surface elevation and ensemble averaged horizontal fluid velocities near the bottom. Solid symbols are the measured data. Open symbols are the COBRAS results.  $S()$  denotes skewness and  $A()$  denotes asymmetry. Circles are the experimental results. Squares are from the nonlinear eddy viscosity model. Triangles are from the RNG model.

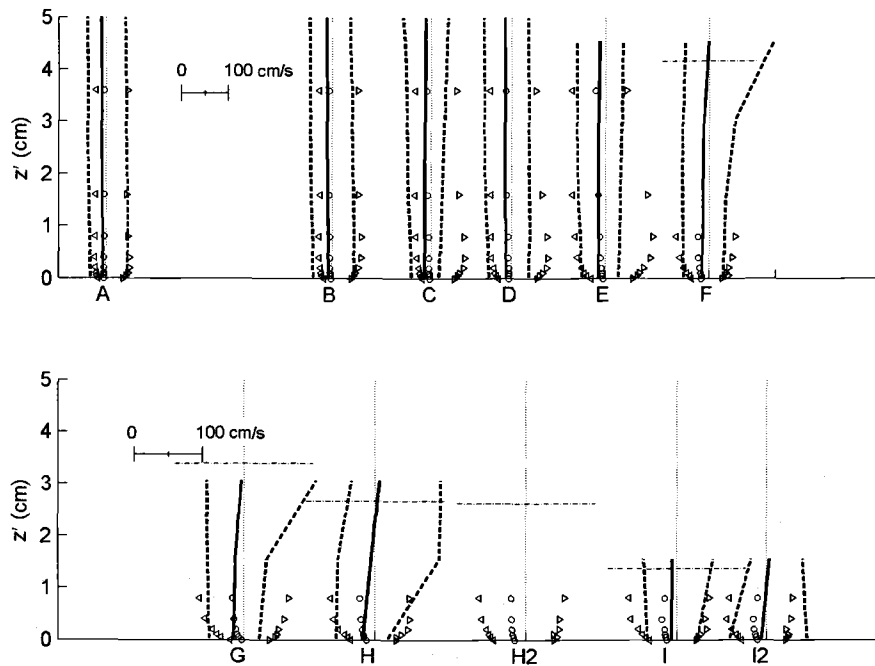


Figure 5.21 Comparison of the mean, maximum, and minimum ensemble averaged horizontal fluid velocities with the experimental data at each cross-shore location. Open symbols are the measured data. Solid and dashed lines are the COBREAS using the nonlinear eddy viscosity model results.

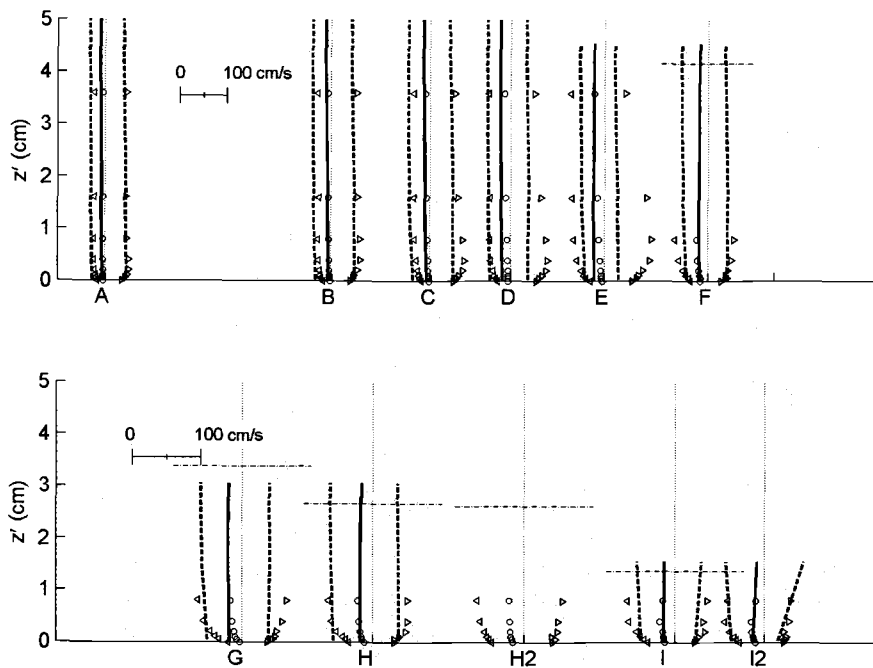


Figure 5.22 Comparison of the mean, maximum, and minimum ensemble averaged horizontal fluid velocities with the experimental data at each cross-shore location. Open symbols are the measured data. Solid and dashed lines are the COBREAS using the RNG model results.

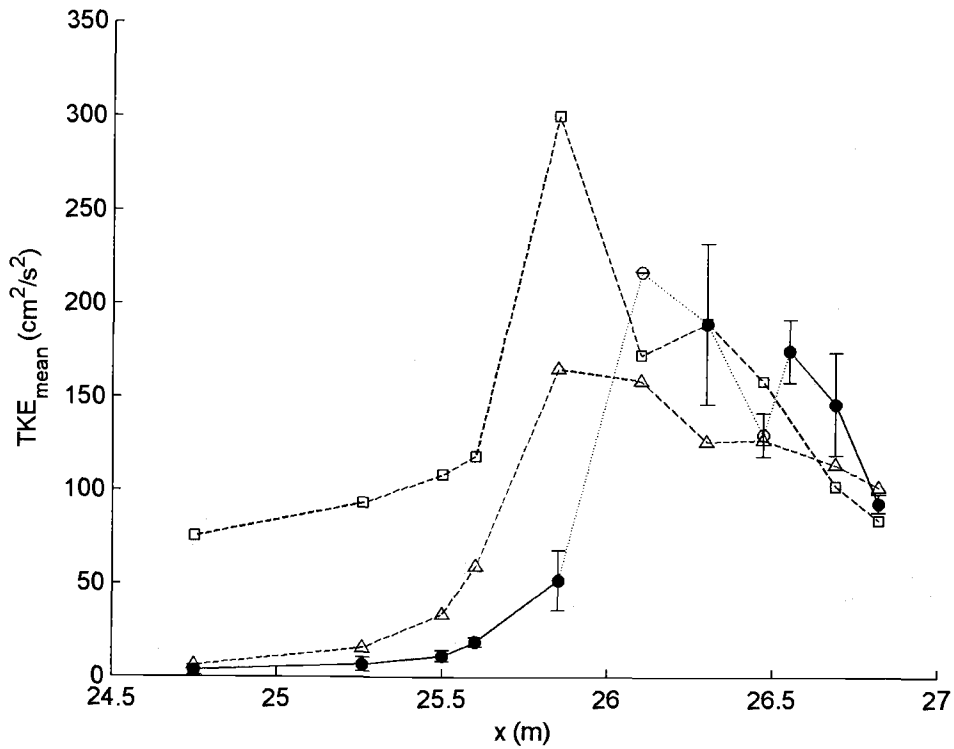


Figure 5.23 The cross-shore variation of the turbulent kinetic energy. Filled circles are the experimental data. Squares are the results with nonlinear eddy viscosity model). Triangles are the results with the RNG model.

## 5.4 Modified Input Conditions

In the previous sections, three models were employed to simulate the hydrodynamics in the inner surf and swash zone measured in the laboratory experiment. The models were initiated at different locations due to the model limitations. RBREAK2 was initiated near wave breaking location (A), whereas FUNWAVE1D and COBRAS were initiated at the flat bottom location far away from wave breaking. Therefore, it is difficult to say which model provides better predictions when compared to the experimental data.

In this section, each model was initiated from the same location using modified input conditions. Two parameters were adjusted: (1) only the incident wave height was used to drive the model (as opposed to the incident and reflected wave height); and (2) the input bathymetry was modified.

First, the estimate of the incident wave height was used as the input wave height in the numerical model because the measured wave height included both incident and reflected wave. This change should delay wave breaking.

Since only one wave gage was installed on the flat bottom section seaward of the surf zone, the separation of incident and reflected waves using the

separation method proposed by Goda and Suzuki (1976) could not be used.

Therefore, in this study, incident waves were separated using the surf similarity parameter-reflection coefficient ( $R$ ) curve in the Shore Protection Manual (2-118), as shown in Figure 5.24. In this curve (A), since  $H_i$  (incident wave height) and  $R$  are unknowns,  $H_i$  was estimated from equation (5.15) and equation (5.16) by empirically.

$$H_t = H_i + H_r = (1 + R)H_i \quad (5.15)$$

$$\xi = \frac{\tan \theta}{\sqrt{H_i/L_0}} \quad (5.16)$$

where,  $H_t$  is the total wave height,  $H_r$  is the reflected wave height,  $\xi$  is the surf similarity parameter,  $L_0$  is the deep water wave length, and  $R \cdot H_i = H_r$ . In this study,  $H_i$  and  $R$  were estimated to be 10.744 cm and 0.0592, respectively.

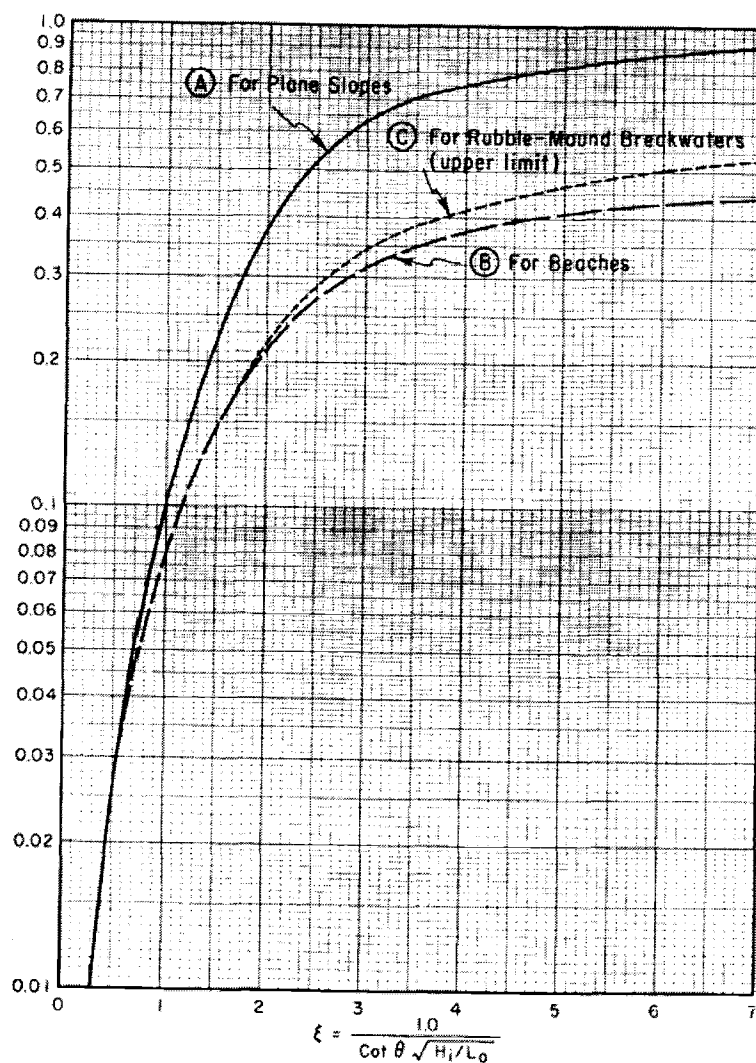


Figure 5.24 Wave reflection coefficients for slopes, beaches, and rubble-mound breakwaters as a function of the surf similarity parameter (Shore Protection Manual, 2-118).  $H_i$  is the incident wave height.  $L_0$  is the deep water wave length. The y axis is the reflection coefficient.

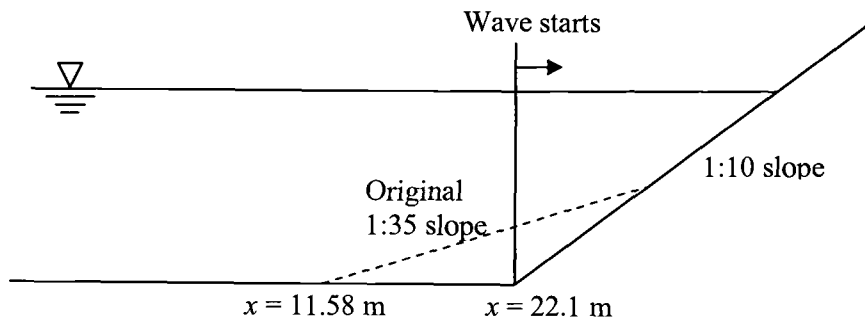


Figure 5.25 Sketch of the modified input conditions.

Additionally, the bathymetry was modified as shown in Figure 5.25. Since the accuracy of RBREAK2 decreases as the point of wave generation seaward of the breaking region, only a 1:10 beach was used, and the 1:35 beach was removed. Using these two modified inputs, the models were then initiated at the same location.

Each model discussed in the previous sections was tested using the modified input conditions: RBREAK2, FUNWAVE1D, COBRAS with the nonlinear eddy viscosity model, and COBRAS with the RNG model. Figure 5.26 (a) shows that all three models predicted similar wave heights at A, and each model, except FUNWAVE1D, predicted wave breaking seaward of the measured data. In Figure 5.26 (b) and (c), the model estimates of the setup and the undertow were not improved when compared to the results using the original input conditions. Moreover, in Figure 5.27, the skewness and the asymmetry of the free surface elevations and near bottom velocities were worse than the results using the

original input conditions. The estimates from RBREAK2 were particularly bad due to the characteristics of the nonlinear shallow water equations.

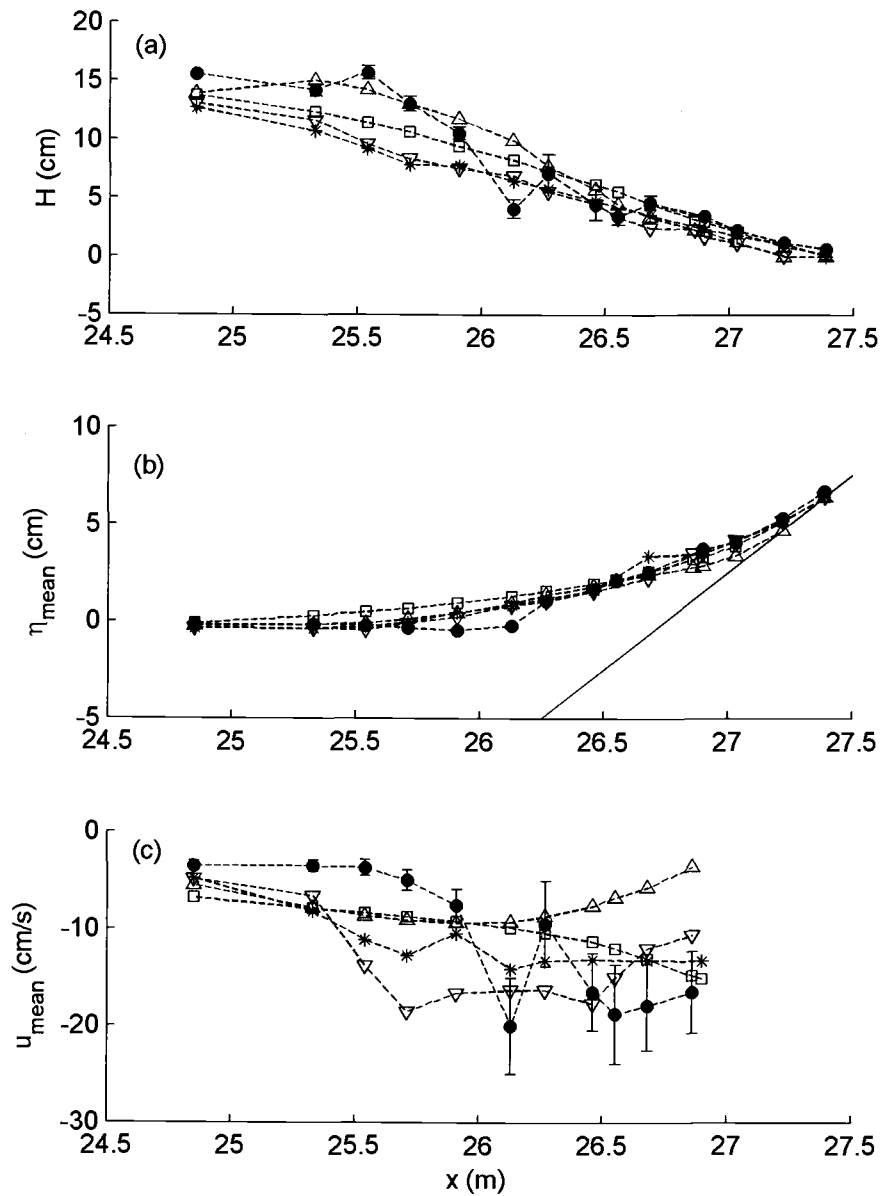


Figure 5.26 Comparison of the wave height variation (a), and setup (b), and undertow near the bottom (c) using the modified input conditions. Filled circles are the experimental data. Open squares are the RBREAK2 results. Triangles are the FUNWAVE1D results. Inverse triangles are the COBRAS results with the RNG model. Asterisks are the COBRAS results with the nonlinear eddy viscosity model.

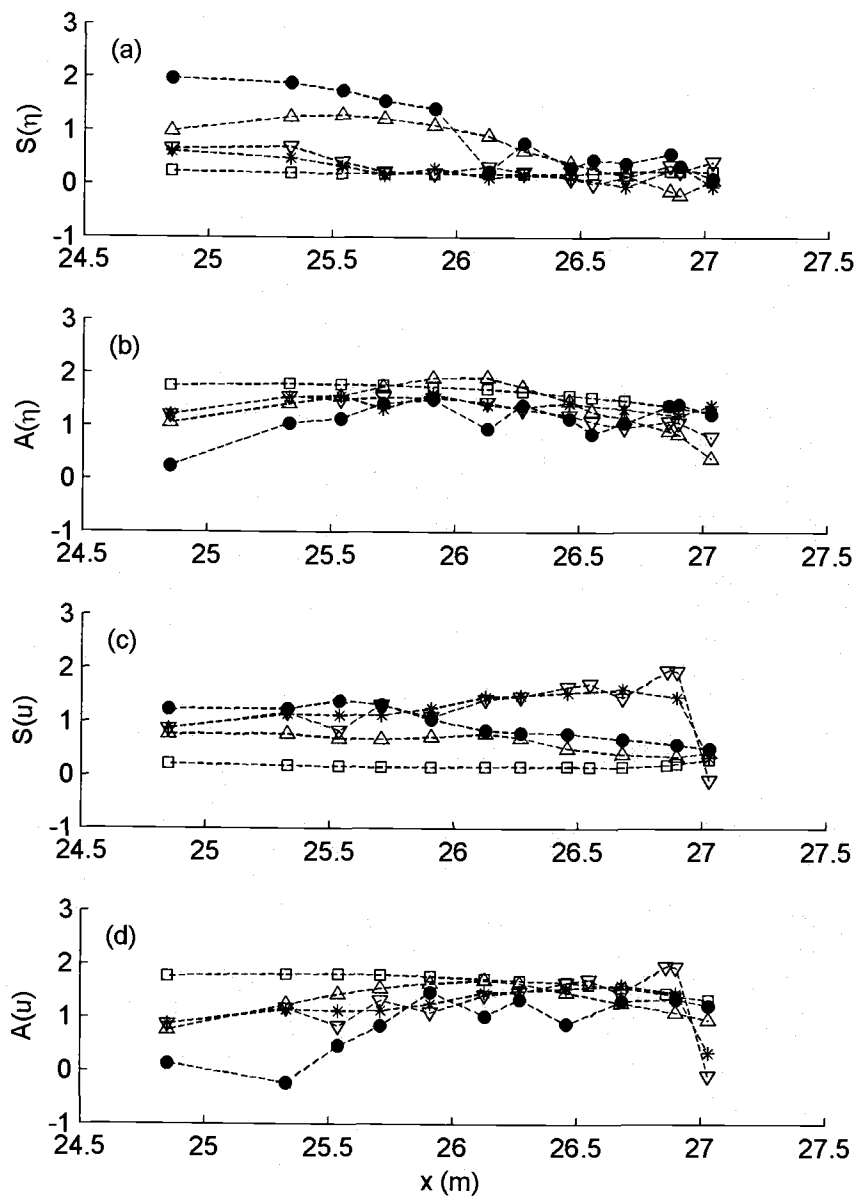


Figure 5.27 Comparison of the skewness and asymmetry of the free surface elevation and ensemble averaged horizontal fluid velocities near the bottom. Filled circles are the experimental data. Open squares are the RBREAK2 results. Triangles are the FUNWAVE1D results. Inverse triangles are the COBRAS results with the RNG model. Asterisks are the COBRAS results with the nonlinear eddy viscosity model.  $S()$  denotes skewness and  $A()$  denotes asymmetry.

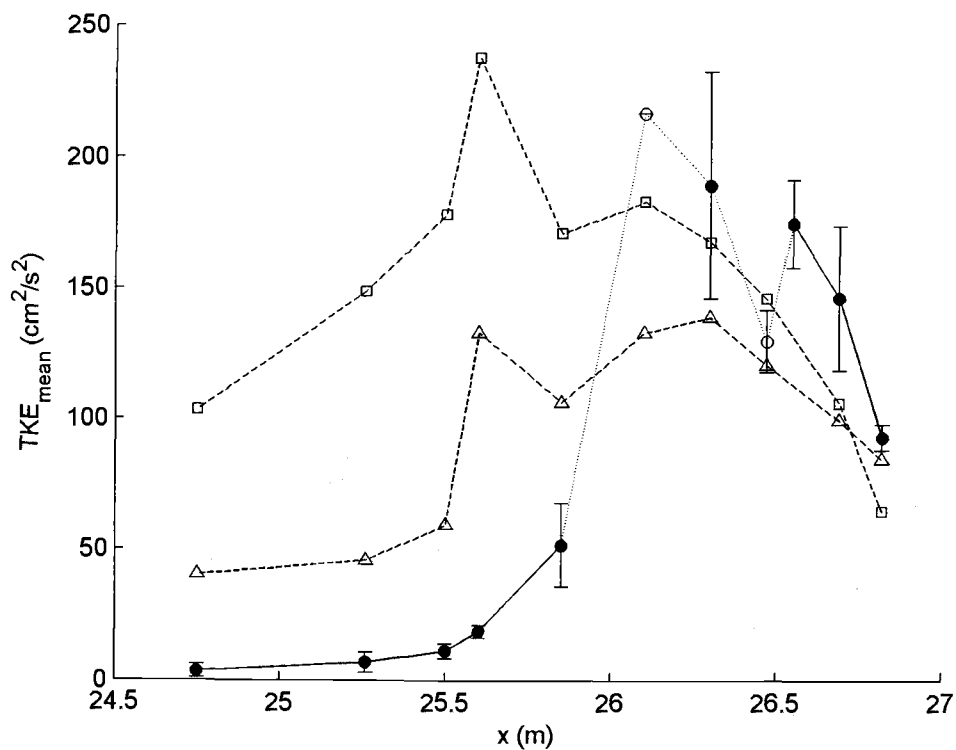


Figure 5.28 The cross-shore variation of the turbulent kinetic energy. Solid circles are the experimental data. Squares are the results from COBRAS using the nonlinear eddy viscosity model. Triangles are the results from COBRAS using the RNG model.

## 5.5 Discussion

In this dissertation, three numerical models were used to simulate the hydrodynamics of the inner surf and swash zone. The one-dimensional models seemed to predict the hydrodynamics slightly better than the two-dimensional model in terms of  $r^2$  values of Table 5.1. However, one of the advantages of two-dimensional model, COBRAS, is that the model can analyze the boundary layer structure and simulate the bottom shear stress. The model can also estimate turbulent quantities using a  $k - \varepsilon$  turbulence closure model. However, it is necessary to improve the turbulence closure model because  $k - \varepsilon$  models typically overpredict TKE when compared to the laboratory measurements. Bradford (2000) made a comparison of different types of  $k - \varepsilon$  models. The results showed that a commonly used  $k - \varepsilon$  model overpredicted the average turbulence level by a factor of two or three when compared to the experimental data reported by Ting and Kirby (1994). However, the RNG model slightly improved the predicted turbulence levels when compared to the prediction from the commonly used  $k - \varepsilon$  model. Larger wave heights were also computed using the RNG model because the model predicted lower turbulence levels than the commonly used  $k - \varepsilon$  model.

In this study, both of the one-dimensional models predicted the cross-shore variations of the wave heights, setup, skewness and asymmetry well. RBREAK2

performed better than FUNWAVE1D in the inner surf and swash zone for undertow, and neither model predicted the cross-shore variation of the undertow through the breaking region. However, COBRAS was able to predict the wave heights and undertow near the bottom at the impinge points. In terms of the hydrodynamics at the bottom boundary layer and TKE, COBRAS provided better prediction and the COBRAS results (TKE and undertow) using RNG model were slightly improved compared to the results using nonlinear eddy viscosity model. Therefore, higher complexity models can be useful to understand the hydrodynamics both at the bottom boundary layer and at the impinge points for strong plunging wave case.

Finally, LES models, as shown in Appendix D, may provide a better understanding of the hydrodynamics important to the inner surf and swash zone. In order to apply this model to the present experimental data set, the model should be run for a longer duration to remove any transitional effects and should simulate enough waves to obtain accurate ensemble averaged quantities. However, a large amount of computation time is required; therefore, one suggestion is to employ the differencing method proposed by Trowbridge (1998) to estimate turbulent quantities over a shorter duration.

## 6 Conclusions

In the present study, a laboratory experimental data set of free surface elevations and fluid velocities (cross-shore and vertical velocities) over a rough bottom was obtained using an LDV with a fine measurement resolution. This data set was used to calculate the ensemble averaged turbulent kinetic energy ( $\langle k \rangle$ ) and intensities ( $\langle u'^2 \rangle$  and  $\langle w'^2 \rangle$ ), and to further understand the hydrodynamics of the inner surf and swash zone. Using this data set, three numerical models were employed to compare numerical results with the data measured in this laboratory experiment.

According to the analysis of this study, the following conclusions are:

1. The ratio of  $\overline{u'^2}$  to  $\overline{w'^2}$  at  $z' > 1$  cm ranged from 1.30 to 1.69, which is close to prior observations of plane wake turbulence ( $\overline{u'^2} / \overline{w'^2} = 1.31$ ). Closer to the bed, the ratio was larger and on average 5.91, which is similar to typical values found in the inner region of a boundary layer ( $\overline{u'^2} / \overline{w'^2} = 6.20$ ).
2. At E (surf zone),  $\langle u \rangle$  near the bottom led in phase when compared to  $\langle u \rangle$  in the upper layer, and  $\langle u \rangle$  at the bore front exceeded the theoretical wave celerity ( $\langle u \rangle_{\max} / \sqrt{g(h + \eta_c)} = 1.09$ ). At F (impinge

point), due to the strong return flow, the largest speed was measured during the return flow ( $u_{\min} = -50.98$  cm/s) compared to the forward motion ( $u_{\max} = 40.09$  cm/s). This is due to the strong return flow and was contrary to the values observed at E and G.

3. At E (surf zone),  $\langle k \rangle$  had a peak just below trough level ( $z^* = 0.5$ ) with forward shift in the phase of the peak intensity at elevations approaching the bed. The energy was mostly dissipated after the passage of the crest.  $\langle u \rangle$  near the bottom is leading in phase with a sharp vertical gradient in the horizontal velocity, suggesting that boundary layer processes may be important in this region. However, at I2 (swash zone), the vertical gradient of  $\langle u \rangle$  was relatively small compared to E (surf zone). This can be explained by the affect that the strong downrush had on turbulent mixing.
4. The time-averaged estimate of  $\langle k \rangle$  was uniform over the vertical throughout the inner surf and swash zone.
5. RBREAK2 accurately predicted the wave height variation, setup and ensemble averaged horizontal fluid velocities including the maximum, minimum, and mean values at each cross-shore location. However, the low frequency oscillation and the asymmetry of the free surface and horizontal fluid velocities were overpredicted in the inner surf and swash zone.

6. FUNWAVE1D also agreed well with the measurements of the wave height and setup. However, the model did not predict undertow in the surf zone. A modification to the model introducing a surface roller may improve the undertow prediction.
7. COBRAS was able to predict the impinge point as well as the wave height, setup, and velocity components accurately. The time averaged TKE was overpredicted compared with that estimated by the experimental data in the surf zone but was predicted well in the swash zone. The RNG turbulence closure model provided slightly better results than the nonlinear eddy viscosity model. This two-dimensional model may be useful in simulating the boundary layer hydrodynamics and estimating the bottom shear stress.

Future work will include estimates of the production and dissipation of turbulence induced by wave breaking and bottom friction and a comparison of those results with several numerical models, specifically in the swash zone.

## **Bibliography**

Archetti, R., Brocchini, M., 2002. An integral swash zone model with friction: an experimental and numerical investigation. *Coast. Engrg.*, 44 (2), 89 – 110.

Sukumaran, A., 2000. Laboratory Measurements of the Temporal and Cross-shore Variation of the Wave-induced Bed Stress. Master's thesis of Civil Engrg. at Texas A&M University.

Bagnold, R. A. 1966. An approach to the sediment transport problem from general physics. *U. S. Geol. Surv.* 422-I, 11 – 137.

Bagnold, R. A., 1963. Beach and nearshore processes; Part 1. Mechanics of marine sedimentation. *The Sea: Ideas and Observations*, vol. 3. Interscience, New York, 507 – 528.

Battjes, J. A. 1974. Surf Similarity. *Proc. 14<sup>th</sup> Int. Conf. on Coast. Engrg.*, ASCE, New York, 466 – 480.

Beach, R. A., Sternberg, R. W., 1991. Infragravity driven suspended sediment transport in the swash, inner and outer-surf zone. *Proc. Coast. Sed. '91*. ASCE, 114 – 128.

Blackwelder, R. F., Kaplan, R. E., 1976. On the wall structure of the turbulent boundary layer. *J. Fluid Mech.*, 76 (1), 89 – 112.

Butt, T., Russell, P., Puleo, J., Miles, J., Masselink, G., 2004. The influence of bore turbulence on sediment transport in the swash and inner surf zones. *Cont. Shelf Res.*, 24, 757 – 771.

Butt, T., Russell, P., Turner, I., 2001. The influence of swash infiltration-exfiltration on beach face sediment transport: onshore or offshore? *Coastal Engrg.* 42, 35 – 52.

Butt, T., Russell, P., 1999. Suspended sediment transport mechanisms in high-energy swash. *Mar. Geol.*, 161, 361 – 375.

Christensen, E. D., Deigaard, R., 2001. Large eddy simulation of breaking waves. *Coast. Engrg.*, 42, 53 – 60.

Cox, D. T., Hobensack, W. A., Sukumaran, A., 2001. Bottom stress in the inner surf and swash zone. *Proc. 27<sup>th</sup> Int. Conf. Coast. Engrg.*, 108 – 119.

Cox, D.T., Kobayashi, N., 2000. Identification of Intense, Intermittent Coherent Motions under Shoaling and Breaking Waves. *J. Geophys. Res.-Oceans*, 105 (6), 14223 – 14236.

Cox, D. T., Kobayashi, N, Okayasu, A., 1996. Bottom shear stress in the surf zone. *J. Geophys. Res.-Oceans*, 101 (6), 14337 – 14348.

Cox, D. T., Kobayashi, N., Kreibel, D. L., 1994. Numerical model verification using SUPERTANK data in surf and swash zones. *Proc. Coastal Dynamics'94*. ASCE, pp. 248 – 262.

Cox, D. T., Shin. S., 2003. Laboratory measurements of void fraction and turbulence in the bore region of surf zone waves. *J. Engrg. Mech. ASCE.*, 129 (10), 1197 – 1205.

Cowen, E.A., Sou, I.M., Liu, P.L.F., Raubenheimer, B., 2003. Particle image velocimetry measurements within a laboratory-generated swash zone. *J. Engrg. Mech.*, 129 (10), 1119 – 1129.

Elfrink, B., Baldock, T., 2002. Hydrodynamics and sediment transport in the swash zone: a review and perspectives. *Coast. Engrg.*, 45, 149 – 167.

Elgar, S., Guza, R. T., 1985. Observations of bispectra of shoaling surface gravity waves. *J. Fluid Mech.*, 161, 425 – 448.

Goda, Y., Suzuki, Y., 1976. Estimation of incident and reflected waves in random wave experiments,” *Proc. 15<sup>th</sup> Int. Conf. Coastal Engrg.*, 828 – 845.

Holland, K.T., Puleo, J.A., Kooney, T.N., 2001. Quantification of swash flows using video-based particle image velocimetry. *Coast. Engrg.*, 44 (2), 65 – 77.

Hughes, M. G., Masselink, G., Brander, R. W., 1997. Flow velocity and sediment transport in the swash zone on a steep beach. *Mar. Geol.* 138, 91 – 103.

Kirby, J. T., Wei, G., Chen, W., Kennedy, A. B., Dalrymple, R. A., 1998.

FUNWAVE 1.0 Fully nonlinear Boussinesq wave model. Documentation and user’s manual, Tech. Rep. CACR-98-06, Center for Applied Coastal Research, Ocean Engineering Laboratory, Univ. Delaware.

Lin, P., Liu, P. L.-F., 1998a. A numerical study of breaking waves in the surf zone. *J. Fluid Mech.*, 359, 239 – 264.

Lin, P., Liu, P. L.-F., 1998b. Turbulent transport, vorticity dynamics, and solute mixing under plunging breaking waves in surf zone. *J. Geophys. Res.*, 103 (C8), 15677 – 15694.

Long, W., Hsu, T., Kirby, J. T., 2004. Modeling cross-shore sediment transport processes with a time domain Boussinesq model. *Proc. 29<sup>th</sup> Int. Conf. Coast. Engrg.*

Masselink, G., Hughes, M. G., 1998. Field investigation of sediment transport in the swash zone. *Cont. Shelf Res.* 18, 1179 – 1199.

Nadaoka, K., Hino, M., Koyano, Y., 1989. Structure of the turbulent flow field under breaking waves in the surf zone. *J. Fluid Mech.*, 204, 359 – 387.

Okayasu, A., Shibayama, T., Horikawa, K. 1988. Vertical variation of undertow in the surf zone. *Proc. 21<sup>st</sup> Int. Conf. Coast. Engrg., ASCE*, 478 – 491.

Osborne, P. D., Rooker, G., 1999. Sand re-suspension events in a high-energy infragravity swash zone. *J. Coast. Res.* 15, 74 – 86.

Petti, M., Longo, S., 2001. Turbulence experiments in the swash zone. *Coast. Engrg.*, 43 (1), 1 – 24.

Puleo, J. A., Holland, K. T., Slinn, D. N., Smith, E., and Webb, B. M., 2002. Numerical modeling of swash zone hydrodynamics. Int. Conf. Coast. Engrg, ASCE.

Puleo, J.A., Beach, R.A., Holman, R.A., Allen, J.S., 2000. Swash zone sediment suspension and transport and the importance of bore-generated turbulence. J. Geophys. Res.-Oceans, 105 (7), 17021 – 17044.

Raubenheimer, B., 2002. Observations and predictions of fluid velocities in the surf and swash zones. J. Geophys. Res.-Oceans, 107 (11), 3190 – 3196.

Raubenheimer, B., Elgar, S., Guza, R. T., 2004. Observations of swash zone velocities: A note on friction coefficients. J. Geophys. Res.-Oceans, 109.

Ryu, Y., Chang, K., Lim., H., 2005. Use of bubble image velocimetry for measurement of plunging wave impinging on structure and associated greenwater. Meas. Sci. Tech., 16, 1 – 9.

Schäffer, H. A., Madsen, P. A., and Deigaard, R., 1993. A Boussinesq model for waves breaking in shallow water. Coast. Engrg., 20, 185 – 202.

Scott, C. P., Cox, D. T., Maddux, T. B., Long, J. W., 2005. Large-scale laboratory observations of turbulence on a fixed barred beach. to be published in *Meas. Sci. and Tech.:* Special Issue on Water Wave Meas., IOP Pub., Inc.

Shin, S., Cox, D. T., 2005. Laboratory observations of inner surf and swash zone hydrodynamics on a steep beach. to be published in *Cont. Shelf Res.* (special issue for swash dynamics).

Suzuki, T., Okayasu, A., 2004. Numerical simulation of 3-D intermittent Sediment Suspension in the Surf Zone. *Proc. 29<sup>th</sup> Int. Conf. Coast. Engrg.*

Svendsen, I. A., 1987. Analysis of surf zone turbulence. *J. Geophys. Res.-Oceans*, 92 (5), 5115 – 5124.

Ting, F. C. K., Kirby, J. T., 1994. Observation of undertow and turbulence in a laboratory surf zone. *Coast. Engrg.*, 24, 51 – 80.

Trowbridge, J., 1998. On a technique for measurement of turbulent shear stress in the presence of surface waves, *J. Atmos. Oceanic Technol.*, 15, 290 – 298.

Turner, I. L., Masselink, G., 1998. Swash infiltration-exfiltration and sediment transport. *J. Geophys. Res.* 103, 30813 – 30824.

Wei, G., Kirby, J. T., Grilli, S. T., Subramanya, R., 1995. A fully nonlinear Boussinesq model for surface waves. Part 1. Highly nonlinear unsteady waves. *J. Fluid Mech.*, 294, 71 – 92.

Yakhot, V., Orszag, S. A., Thangam, S. Gatski, T. B., Speziale, C. G., 1992. Development of turbulence models for shear flows by a double expansion technique. *Phys. of Fluids A*, 4, 1510 – 1520.

Table A.1 Summary of elevations (cm from the bottom) for LV measurements (Sukumaran, 2000).

	A	B	C	D	E	F	G	H	H2	I	I2	K	L	M
1	0.0	0.0	0.0	0.0	0.0	0.0	0.0	0.0	0.0	0.0	0.0	0.0	0.0	0.0
2	0.5	0.5	0.5	0.5	0.5	0.5	0.5	0.5	0.5	0.5	0.5	0.5	0.5	0.5
3	1.0	1.0	1.0	1.0	1.0	1.0	1.0	1.0	1.0	1.0	1.0	1.0	1.0	1.0
4	2.0	2.0	2.0	2.0	2.0	2.0	2.0	2.0	2.0	2.0	2.0	2.0	2.0	
5	4.0	4.0	4.0	4.0	4.0	4.0	4.0	4.0	4.0	4.0	4.0	4.0	4.0	
6	8.0	8.0	8.0	8.0	8.0	8.0	8.0	8.0	8.0	8.0	8.0	8.0	8.0	
7	16.0	16.0	16.0	16.0	16.0	16.0	16.0	16.0	16.0	16.0	16.0	16.0		
8	36.0	36.0	36.0	36.0	36.0	26.0	18.0	21.0	21.0	21.0	21.0	18.0		
9	66.0	66.0	66.0	66.0	66.0	36.0	21.0	26.0	26.0	26.0	26.0	21.0		
10	96.0	96.0	96.0	96.0	96.0	46.0	26.4	31.0	31.0	31.0	31.0	26.0		
11	126.0	126.0	126.0	126.0	126.0	56.0	31.0	36.0	36.0	36.0	36.0			
12	156.0	156.0	156.0	156.0	156.0	66.0	36.0	41.0	41.0	41.0	41.0			
13	171.0	171.0	171.0	171.0	171.0	76.0	46.0	46.0	46.0	46.0				
14	186.0	186.0	186.0	186.0	186.0	86.0	56.0	51.0	51.0					
15	201.0	201.0	201.0	201.0			66.0	56.0						
16	216.0	216.0	216.0	216.0			76.0							
17	231.0	231.0	231.0											
18	246.0													

**Appendix B. The vertical profile of the ensemble averaged free surface elevations and the fluid velocities.**

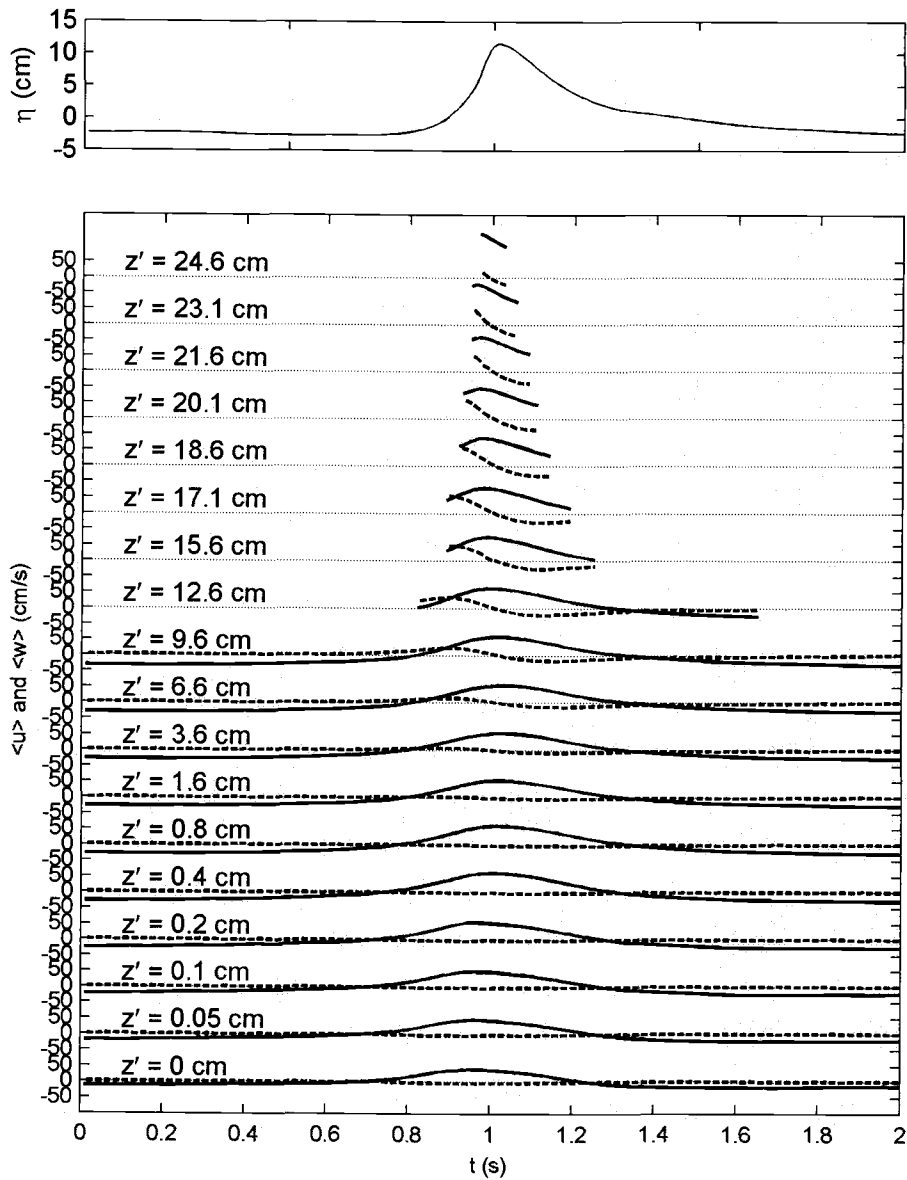


Figure B.1 The vertical profile of the ensemble averaged horizontal and vertical fluid particle velocities ( $\langle u \rangle$  and  $\langle w \rangle$ ) at B. Solid lines are  $\langle u \rangle$  and dashed lines are  $\langle w \rangle$ .

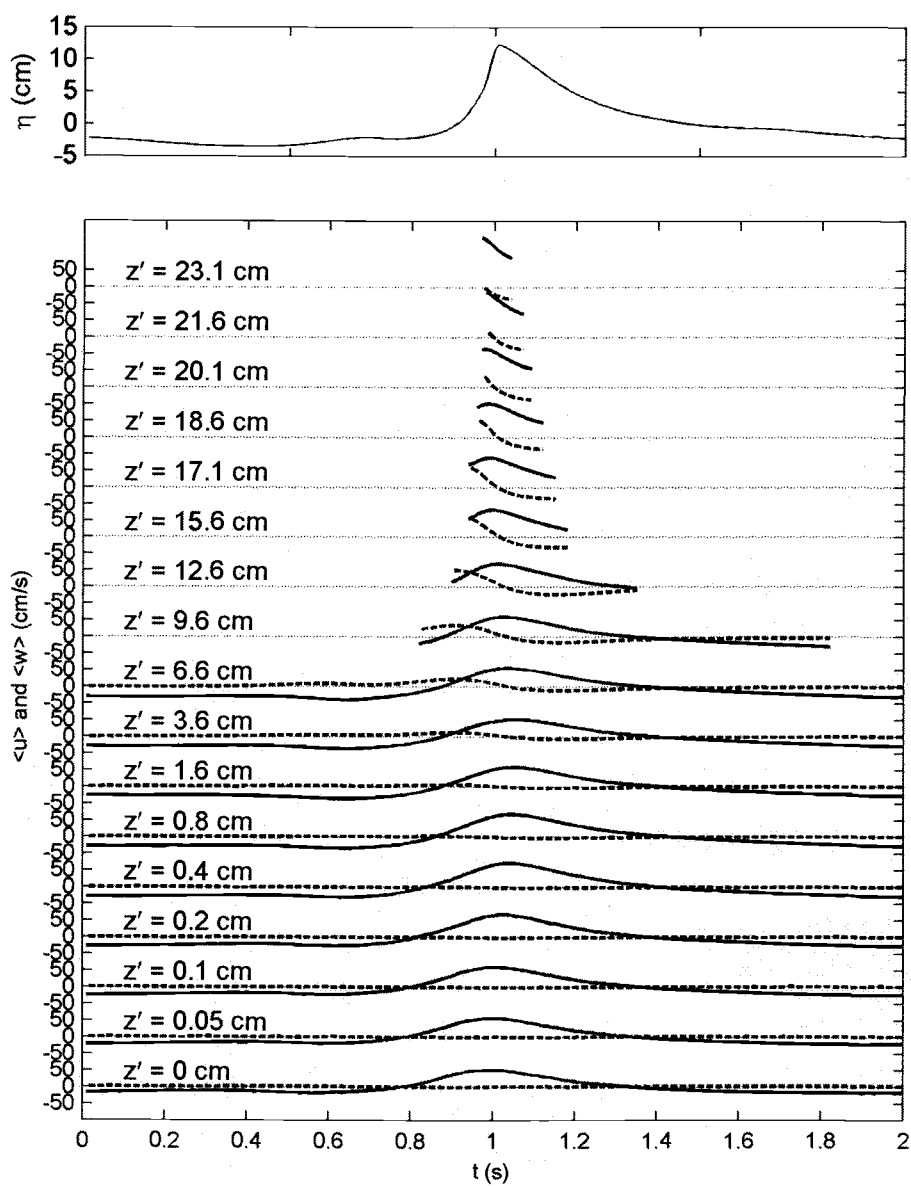


Figure B.2 The vertical profile of the ensemble averaged horizontal and vertical fluid particle velocities ( $\langle u \rangle$  and  $\langle w \rangle$ ) at C. Solid lines are  $\langle u \rangle$  and dashed lines are  $\langle w \rangle$ .

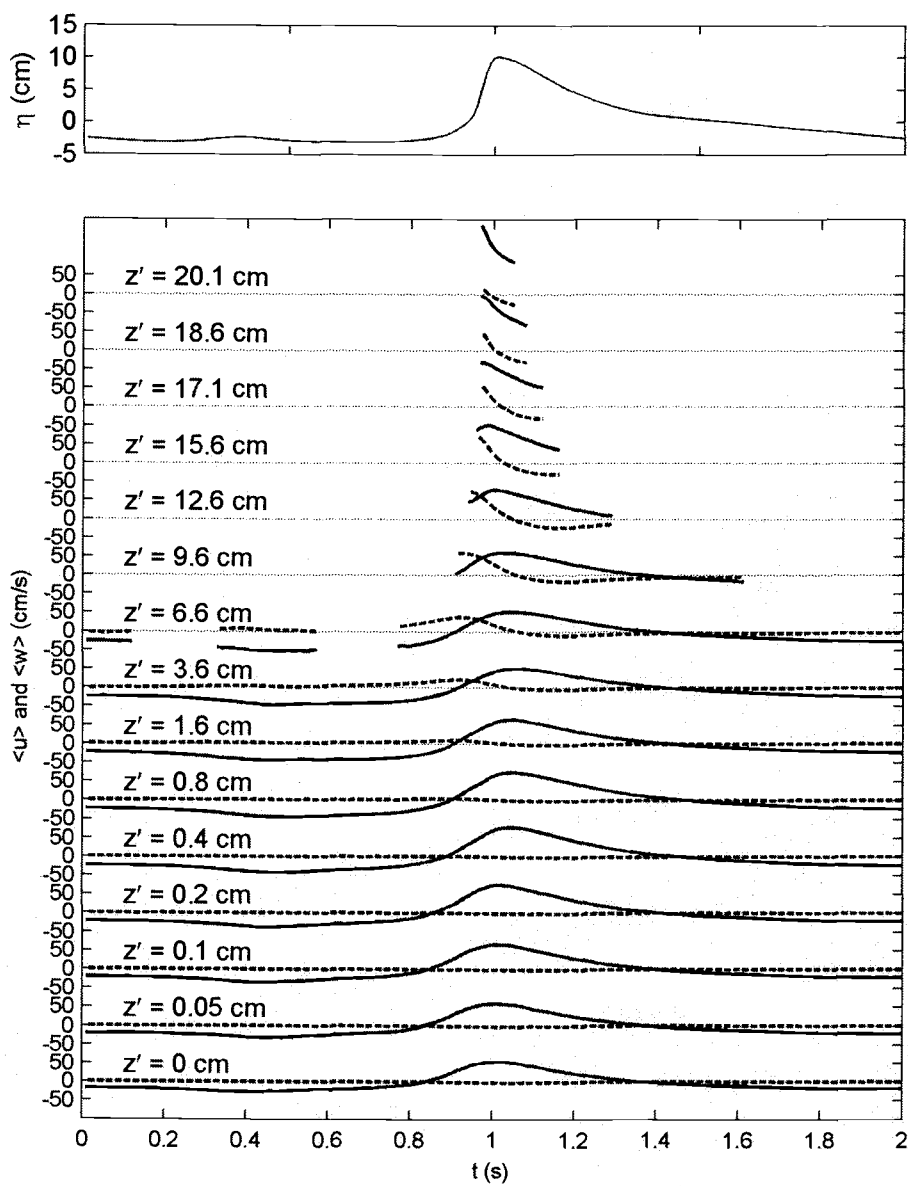


Figure B.3 The vertical profile of the ensemble averaged horizontal and vertical fluid particle velocities ( $\langle u \rangle$  and  $\langle w \rangle$ ) at D. Solid lines are  $\langle u \rangle$  and dashed lines are  $\langle w \rangle$ .

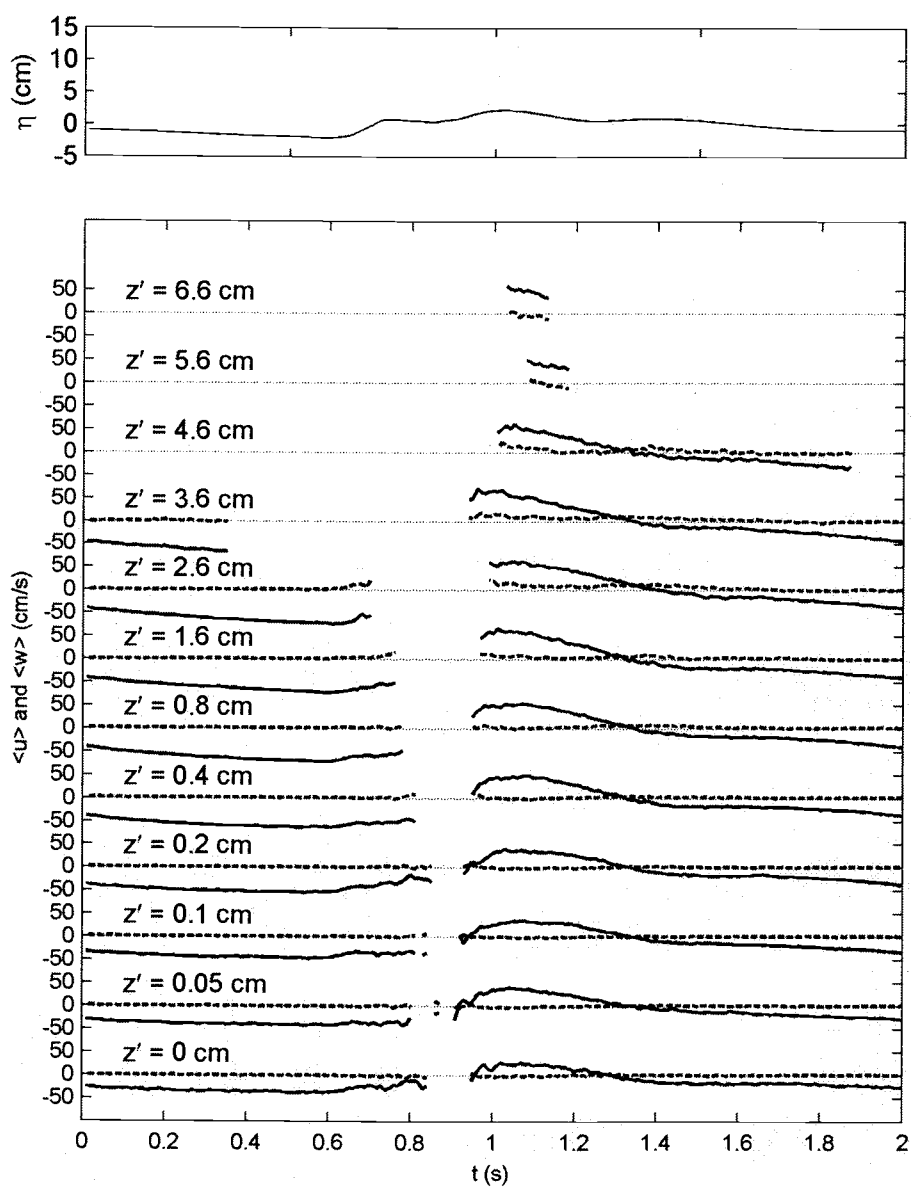


Figure B.4 The vertical profile of the ensemble averaged horizontal and vertical fluid particle velocities ( $\langle u \rangle$  and  $\langle w \rangle$ ) at F. Solid lines are  $\langle u \rangle$  and dashed lines are  $\langle w \rangle$ .

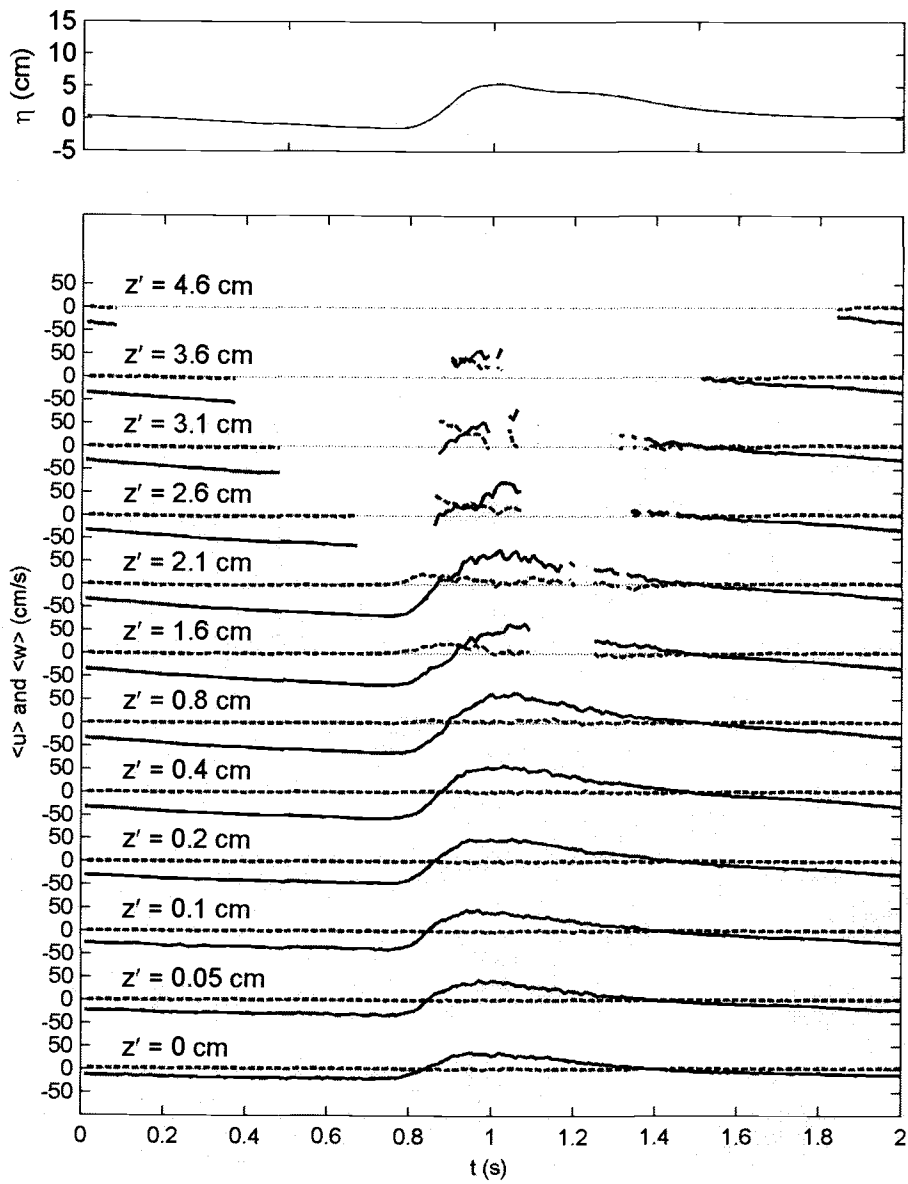


Figure B.5 The vertical profile of the ensemble averaged horizontal and vertical fluid particle velocities ( $\langle u \rangle$  and  $\langle w \rangle$ ) at G. Solid lines are  $\langle u \rangle$  and dashed lines are  $\langle w \rangle$ .

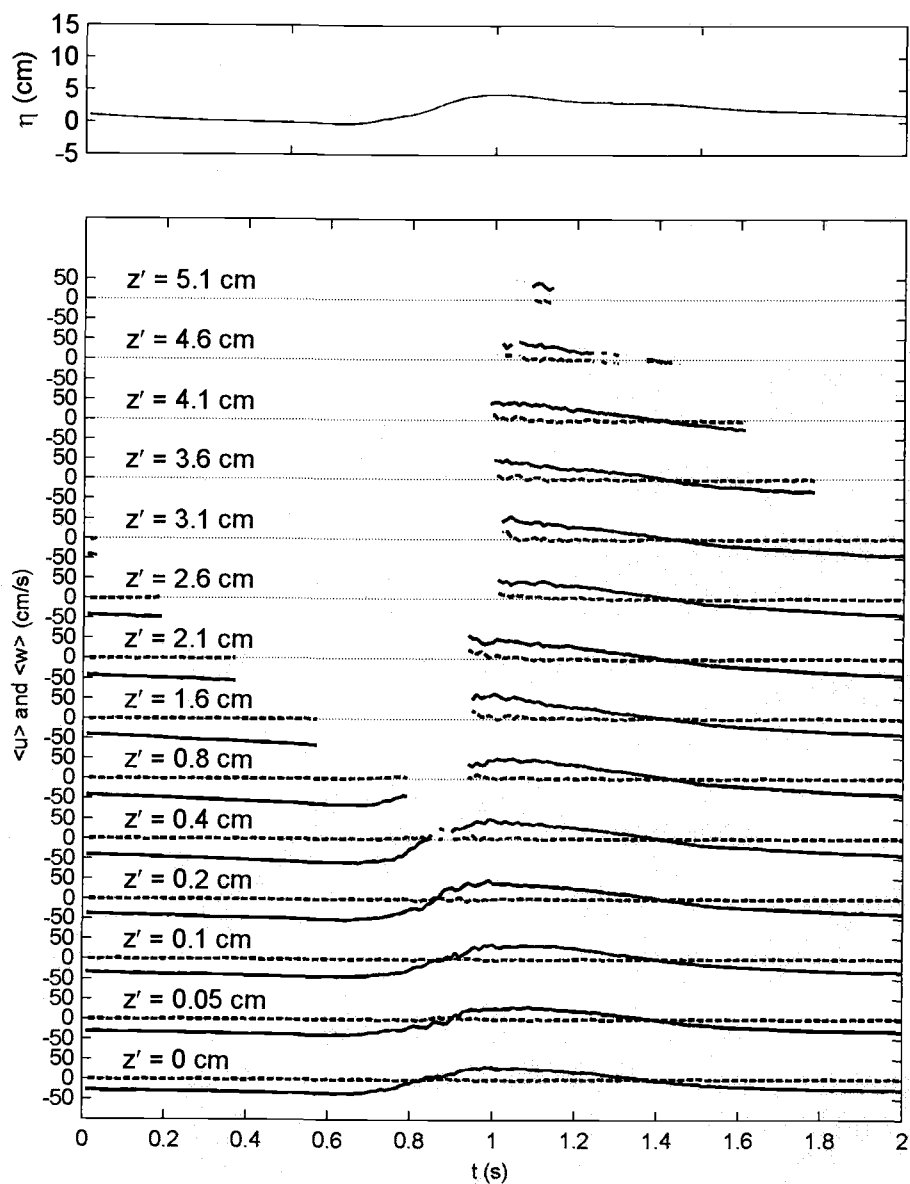


Figure B.6 The vertical profile of the ensemble averaged horizontal and vertical fluid particle velocities ( $\langle u \rangle$  and  $\langle w \rangle$ ) at H. Solid lines are  $\langle u \rangle$  and dashed lines are  $\langle w \rangle$ .

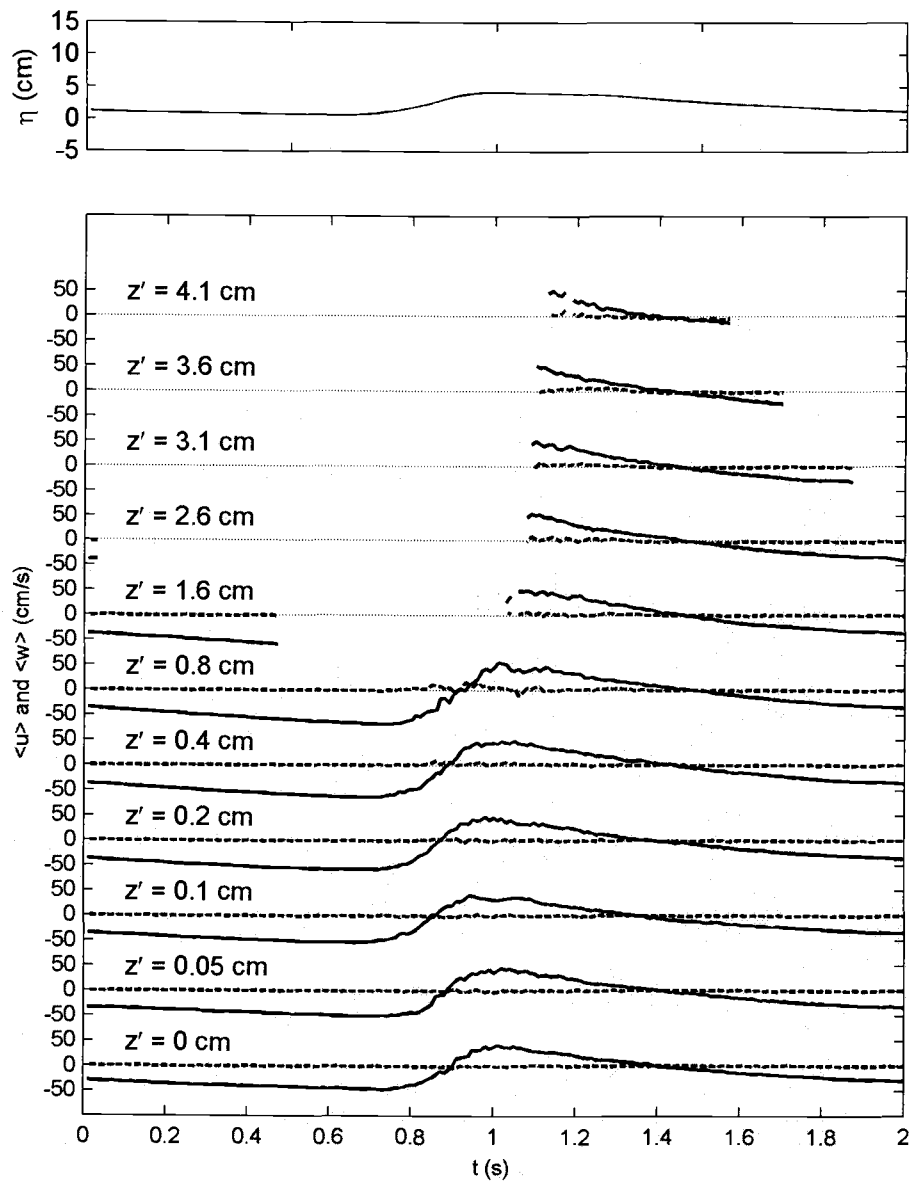


Figure B.7 The vertical profile of the ensemble averaged horizontal and vertical fluid particle velocities ( $\langle u \rangle$  and  $\langle w \rangle$ ) at H2. Solid lines are  $\langle u \rangle$  and dashed lines are  $\langle w \rangle$ .

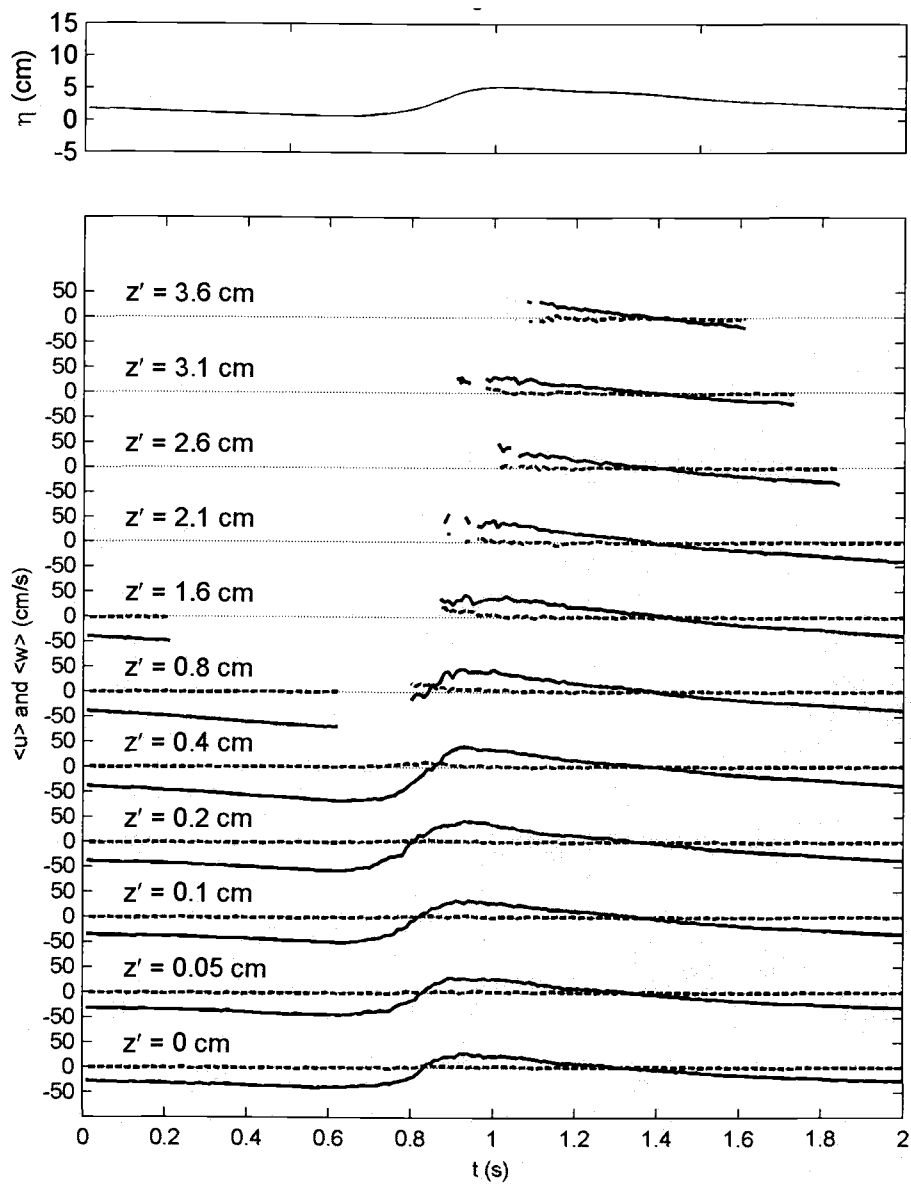


Figure B.8 The vertical profile of the ensemble averaged horizontal and vertical fluid particle velocities ( $\langle u \rangle$  and  $\langle w \rangle$ ) at I. Solid lines are  $\langle u \rangle$  and dashed lines are  $\langle w \rangle$ .

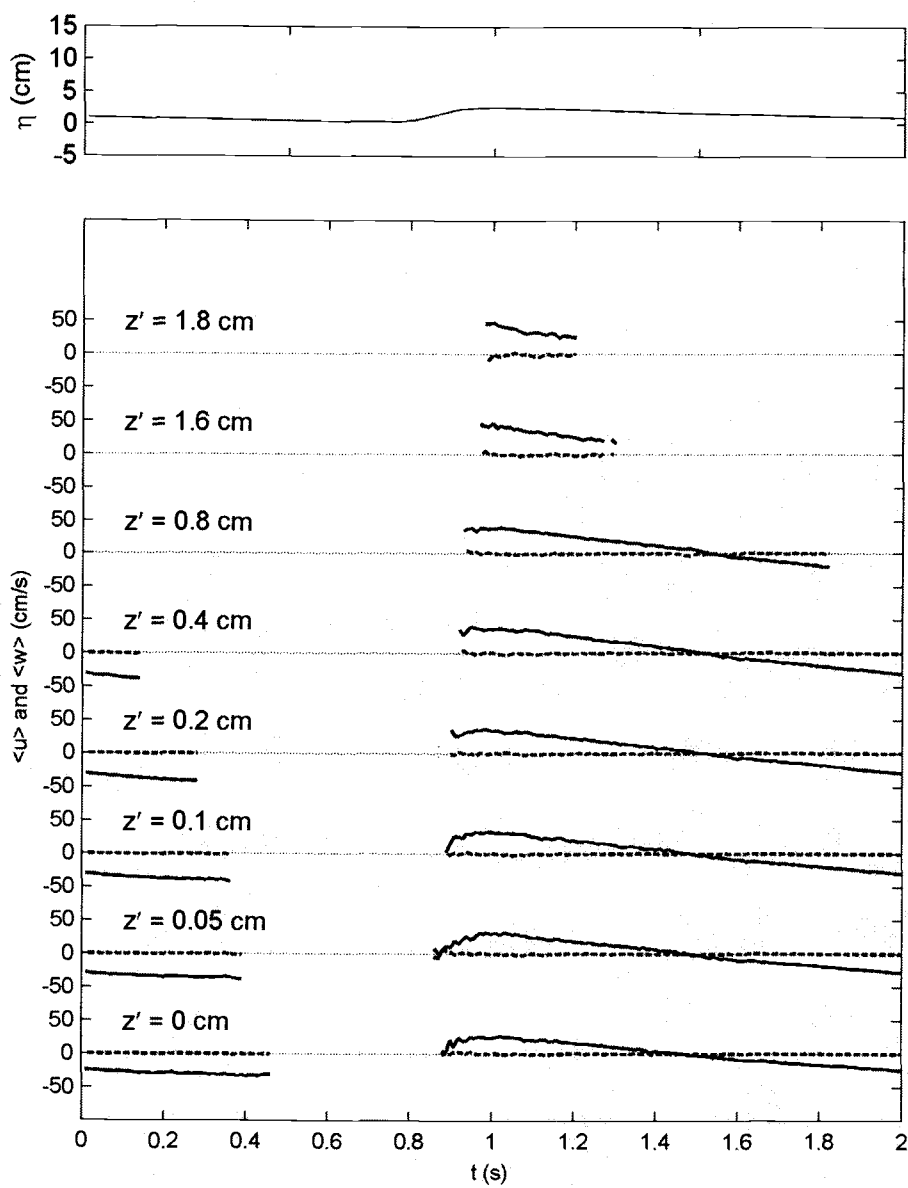


Figure B.9 The vertical profile of the ensemble averaged horizontal and vertical fluid particle velocities ( $\langle u \rangle$  and  $\langle w \rangle$ ) at K. Solid lines are  $\langle u \rangle$  and dashed lines are  $\langle w \rangle$ .

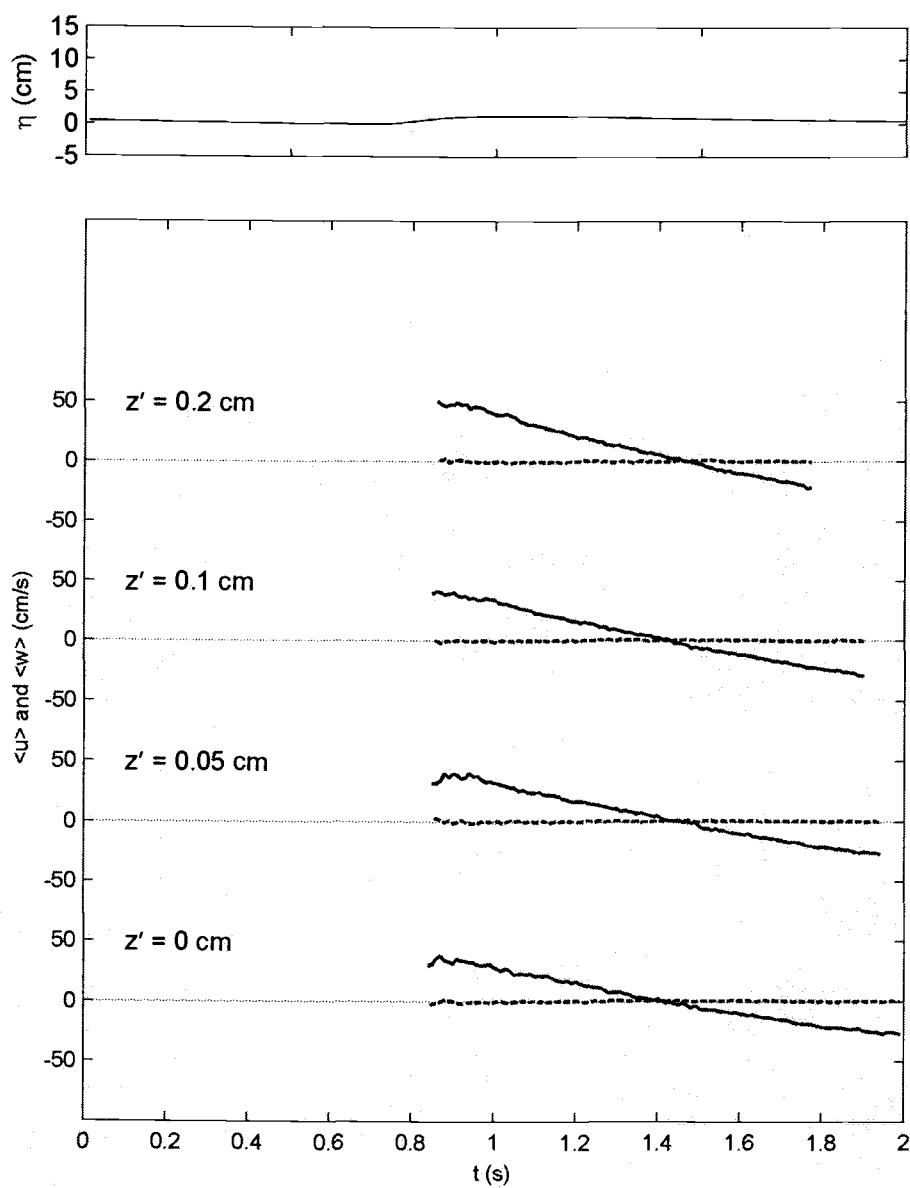


Figure B.10 The vertical profile of the ensemble averaged horizontal and vertical fluid particle velocities ( $\langle u \rangle$  and  $\langle w \rangle$ ) at L. Solid lines are  $\langle u \rangle$  and dashed lines are  $\langle w \rangle$ .

**Appendix C. A contour plot of ensemble averaged turbulent kinetic energy and wave induced horizontal velocities**

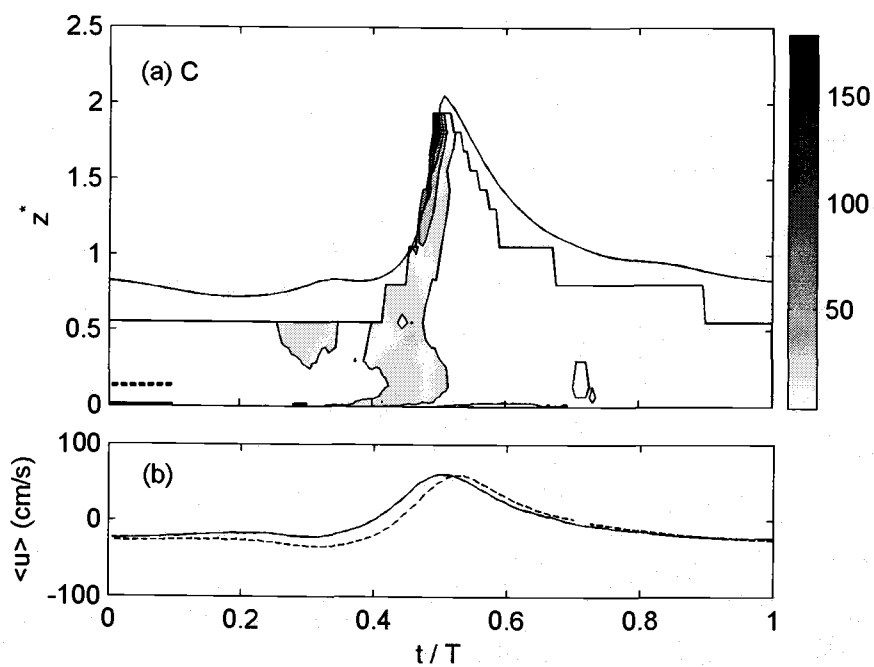


Figure C.1 A contour plot of ensemble averaged turbulent kinetic energy  $\langle k \rangle$  in  $\text{cm}^2/\text{s}^2$  (a) and wave induced horizontal velocities  $\langle u \rangle$  (b) at C. In (b), solid line is the wave velocity at  $z' = 0.10$  cm, shown by the heavy solid line in (a), and dashed line is at  $z' = 1.60$  cm, shown by the heavy dashed line in (a).

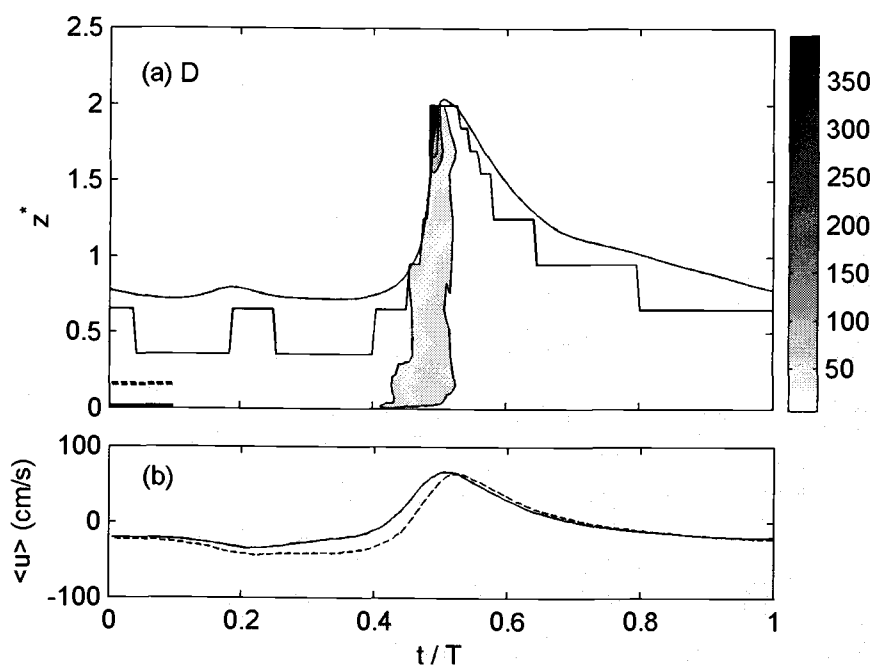


Figure C.2 A contour plot of ensemble averaged turbulent kinetic energy  $\langle k \rangle$  in  $\text{cm}^2/\text{s}^2$  (a) and wave induced horizontal velocities  $\langle u \rangle$  (b) at D. In (b), solid line is the wave velocity at  $z' = 0.10$  cm, shown by the heavy solid line in (a), and dashed line is at  $z' = 1.60$  cm, shown by the heavy dashed line in (a).

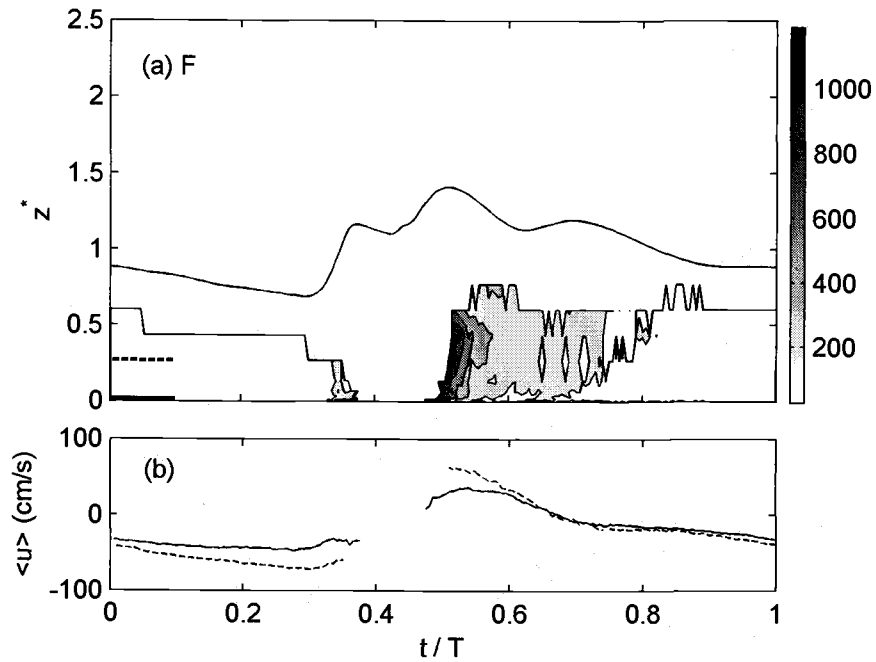


Figure C.3 A contour plot of ensemble averaged turbulent kinetic energy  $\langle k \rangle$  in  $\text{cm}^2/\text{s}^2$  (a) and wave induced horizontal velocities  $\langle u \rangle$  (b) at F. In (b), solid line is the wave velocity at  $z' = 0.10$  cm, shown by the heavy solid line in (a), and dashed line is at  $z' = 1.60$  cm, shown by the heavy dashed line in (a).

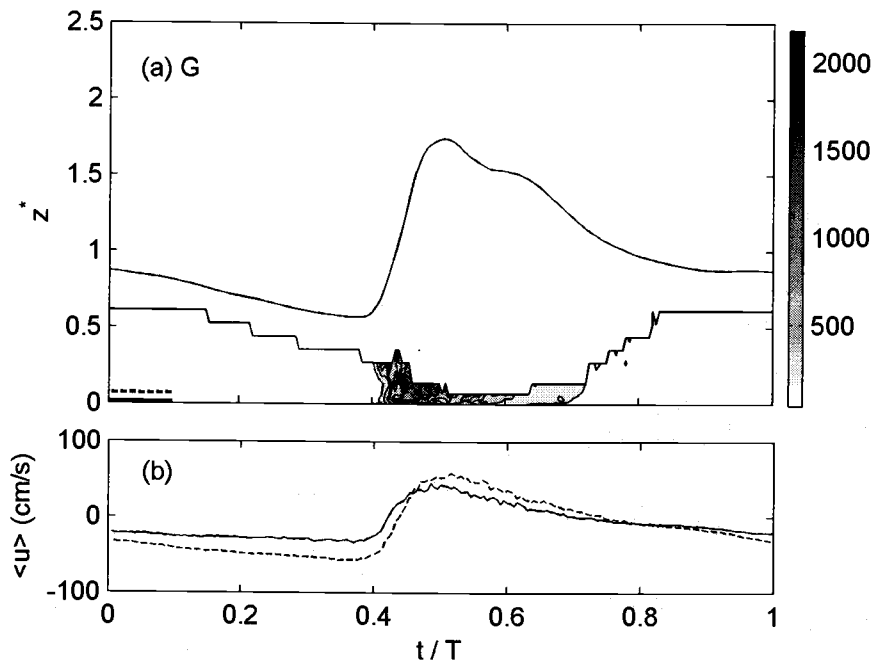


Figure C.4 A contour plot of ensemble averaged turbulent kinetic energy  $\langle k \rangle$  in  $\text{cm}^2/\text{s}^2$  (a) and wave induced horizontal velocities  $\langle u \rangle$  (b) at G. In (b), solid line is the wave velocity at  $z' = 0.10$  cm, shown by the solid line in (a), and dashed line is at  $z' = 0.4$  cm, shown by the dashed line in (a).

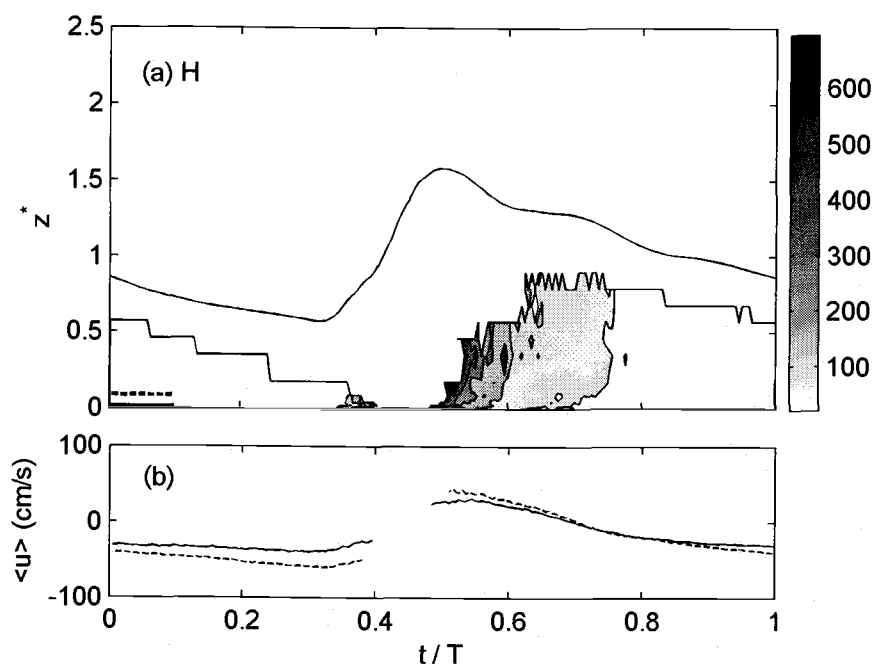


Figure C.5 A contour plot of ensemble averaged turbulent kinetic energy  $\langle k \rangle$  in  $\text{cm}^2/\text{s}^2$  (a) and wave induced horizontal velocities  $\langle u \rangle$  (b) at H. In (b), solid line is the wave velocity at  $z' = 0.10$  cm, shown by the heavy solid line in (a), and dashed line is at  $z' = 0.4$  cm, shown by the heavy dashed line in (a).

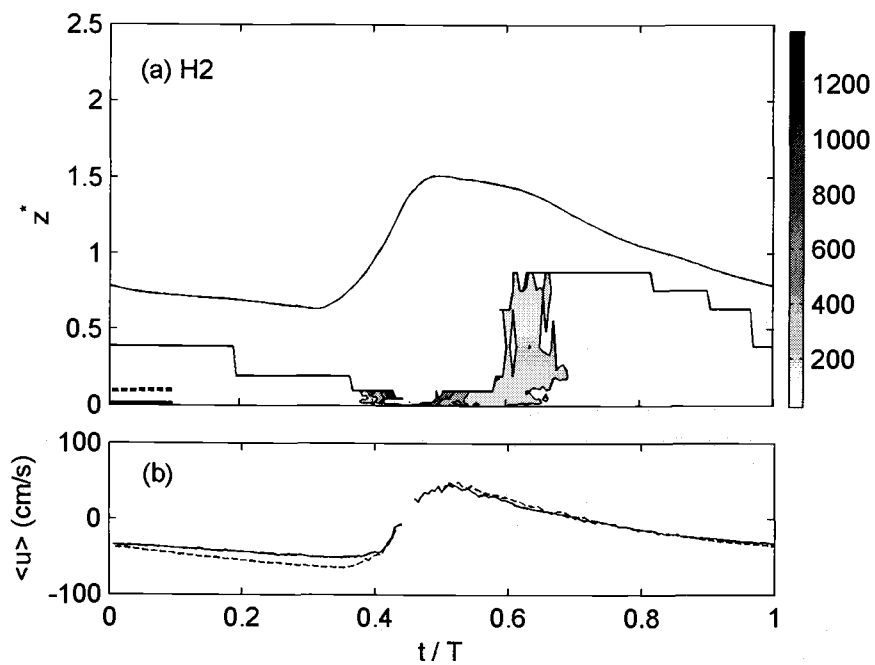


Figure C.6 A contour plot of ensemble averaged turbulent kinetic energy  $\langle k \rangle$  in  $\text{cm}^2/\text{s}^2$  (a) and wave induced horizontal velocities  $\langle u \rangle$  (b) at H2. In (b), solid line is the wave velocity at  $z^* = 0.10$  cm, shown by the heavy solid line in (a), and dashed line is at  $z^* = 0.4$  cm, shown by the heavy dashed line in (a).

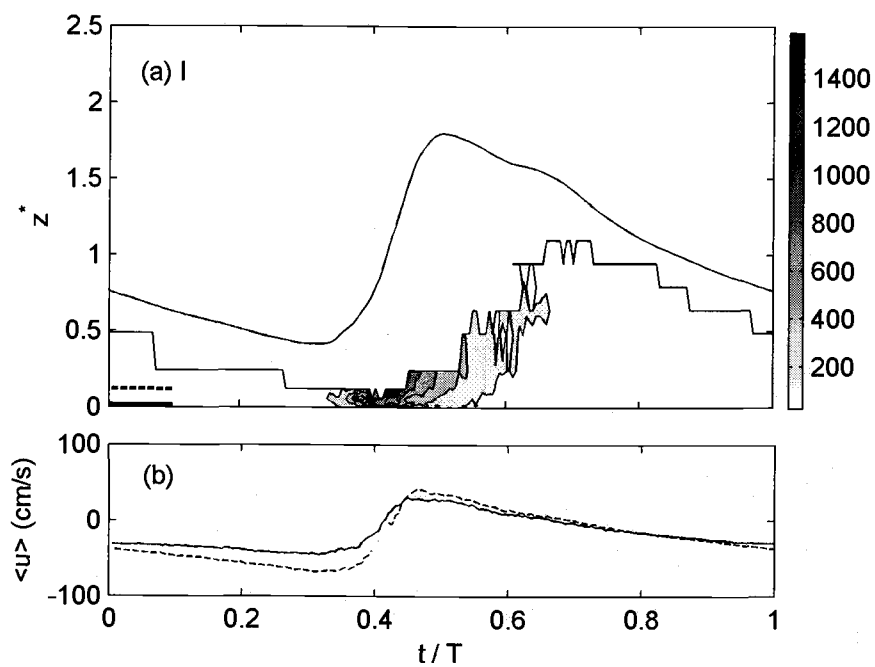


Figure C.7 A contour plot of ensemble averaged turbulent kinetic energy  $\langle k \rangle$  in  $\text{cm}^2/\text{s}^2$  (a) and wave induced horizontal velocities  $\langle u \rangle$  (b) at I. In (b), solid line is the wave velocity at  $z' = 0.10\text{ cm}$ , shown by the heavy solid line in (a), and dashed line is at  $z' = 0.4\text{ cm}$ , shown by the heavy dashed line in (a).

## **Appedix D. Three-Dimensional Model: Large Eddy Simulation**

A three-dimensional numerical model was also used to simulate the inner surf and swash zone hydrodynamics. This Large Eddy Simulation (LES) model was developed by Suzuki and Okayasu (2004) at Yokohama University. It is quite similar to a Direct Numerical Simulation (DNS), which solves the Navier-Stokes equations directly. Unfortunately, DNS requires a large amount of computational time for high Reynolds number flows, such as breaking waves. LES models also solve the Navier-Stokes equations directly for eddies larger than the grid size but it use a turbulence closure model to estimate the contribution from small-scale turbulence (smaller than the grid size). To simulate the breaking waves, boundary layer, and thin layer of the swash zone found in this experiment, which increases the computational time required to run the model. This indicates that the model should solve the governing equation directly for the larger scale turbulence than the fine grid size. The LES model developed by Okayasu uses a subgrid scale model (SGS) to simulate the small scale turbulence. The density function method was used to simulate the free surface elevation.

The governing equations in this model are the spatially averaged Navier-Stokes equations:

$$\frac{\partial \bar{u}_i}{\partial x_i} = 0 \quad (\text{D.1})$$

$$\frac{\partial \bar{u}_i}{\partial t} + \bar{u}_j \frac{\partial \bar{u}_i}{\partial x_j} = -\frac{1}{\rho} \frac{\partial \bar{p}}{\partial x_i} + \nu \frac{\partial^2 \bar{u}_i}{\partial x_j^2} - \frac{\partial}{\partial x_j} (\tau_{ij}) + g_i \quad (\text{D.2})$$

In equation 5.16, the SGS term is  $\partial \tau_{ij} / \partial x_j$ . This term is defined as

$\tau_{ij} = -2\nu_t \bar{D}_{ij}$  and  $\nu_t = (c_s \Delta)^2 |\bar{D}|$  (Smagorinsky's model), where  $c_s$  is the smagorinsky constant and  $D$  is the strain rate.

In the present study, this model was run only as a preliminary test, because the model is not yet fully calibrated. The model was initiated at location A with a model defined free surface elevation. The grid size was set to 1 cm × 1 cm and the time increment ( $dt$ ) was set to 0.00064 s per the model suggestion (15 times smaller than the grid size). The entire computational domain was tilted 5.7 degrees clock-wise in order to make the horizontal axis parallel to the bottom. Figure D.1 shows the vector field from the LES simulation. In this figure, the flow strongly rebounded at the impinge point (F).

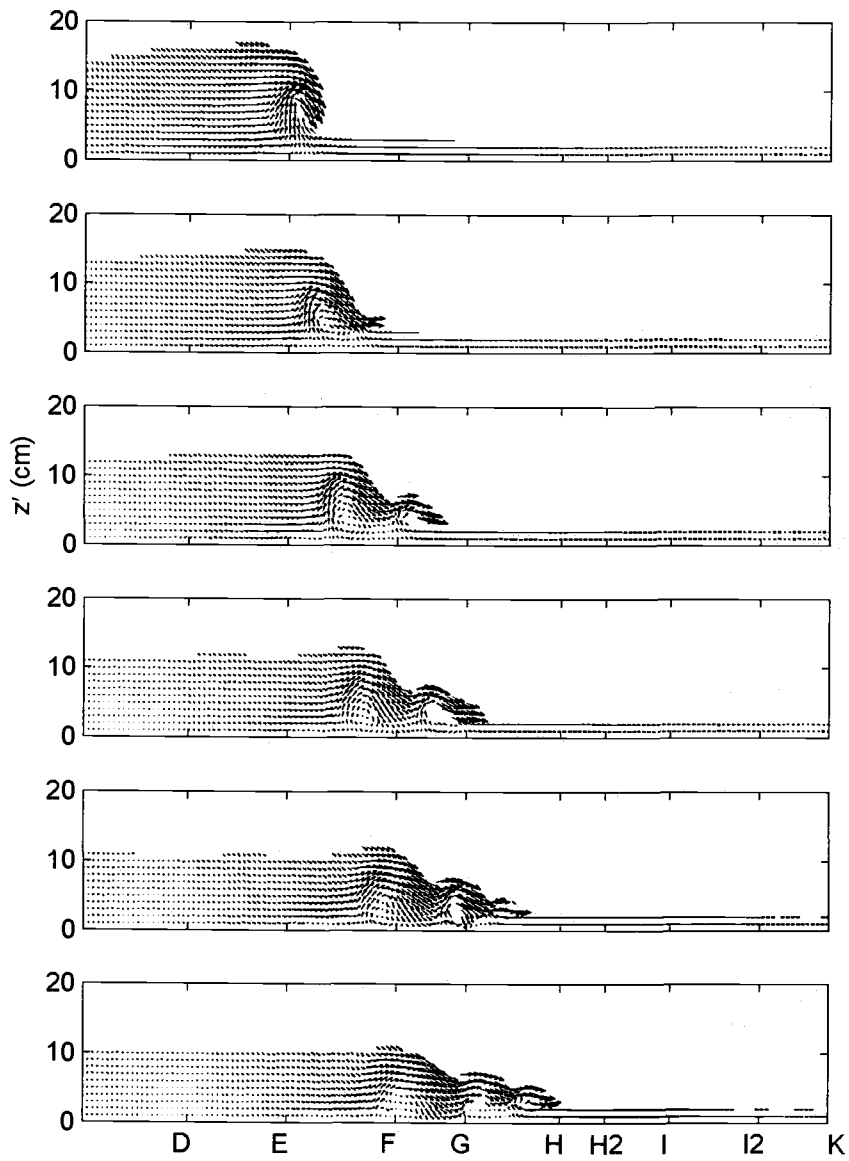


Figure D.1 Vector field simulated using the LES model (Yokohama Univ.) at several time steps.

## Appedix E. Numerical model inputs

### RBREAK2 using the original input

```

3          --> NLINES
-----
RUN RN3: SPECIFY TOTAL WAVE
-----
20          --> IJOB,ISTAB
1           --> ISYST
1           --> IBOT
1           --> INONCT
1           --> IENERG
3  0  WGT2   --> IWAVE,MSTAT,FINP2
1  1  200 100 --> ISAVA,MSAVA1,MSAVA2,NTIMES
1  15          --> ISAVB,NNODB
0  0          --> ISAVC,NNODC
00000  0      --> IREQ,IELEV,IV,IDUDT,ISNR,NNREQ
100          --> INITS
1           --> MULTIF
.003000     --> DELTA (NORMALIZED)
200.000000  --> TMAX (NORMALIZED)
100          --> NRATE
1           --> NDELR
1.000000    --> DELRP(1) (MILLIMETERS)
2.000000 2.000000 --> X1,X2
0.155700 2.000000 --> HREFP(METERS),TP(SECONDS)
1.000000 1.000000 --> KSREF,KSSEA
0.190000   --> DSEAP(METERS)
0.100000   --> TSLOPS
1           --> NBSEG
8.500000 0.100000 0.010000 --> WBSEG(1),TBSLOP(1),FWP(1)
1  63  91 113 139   --> NODB(1)-(2)-(3)-(4)-(5)
168 186 210 222 239 --> NODB(1)-(2)-(3)-(4)-(5)
262 268 285 309 331 --> NODB(1)-(2)-(3)-(4)-(5)

```

**FUNWAVE1D using the original input (funwave1d.data)**

```
$data1
ibe = 2
imch = 4
ianm = 0
a0 = 0.0569
h0 = 0.6
tpd = 2.0
dx = 0.04
dt = 0.01
mx = 1260
nt = 8192
itbgn = 1000
itend = 8000
itdel = 10
itscr = 100
itftr = 500
cbkv = 0.55
ck_bt = 0.01
delta = 0.002
slmda = 80.
isltb = 774
islte = 1260
$end
```

```
$data2
isrc = 744
swidth = .45
cspg = 10.0
cspg2 = 0.0
cspg3 = 0.0
ispg = 400 51
ngage = 17
ixg = 744 1082 1094 1099 1103
      1108 1114 1117 1122 1124
      1128 1132 1133 1136 1141
      1145 1150
itg = 2000 2010 2020 2030 2040 2050 2060 2070 2080 2090 2100 2110
$end
```

```
$data3
f1n = 'sw_depth.dat'
f2n = 'initw.data'
f3n = 'random1d.mk'
f4n = 'etats.out'
f5n = 'tmp.out'
f6n = 'etaxs.out'
f7n = 'etaxt.out'
f9n = 'eddy.out'
$end
```

```
$data4
itide = 0
tideco = 0 0.0 0.0
$end
```

**COBRAS using the original input.**

- kemodel =4 (the nonlinear eddy viscosity model)
- kemodel =6 (the RNG model)

```

$numparam
0.005,500.1,60.2,0.02 <==delt,twfin,prtdt,pltdt
0.3,1.0,6,1,1,1.0 <==alpha,beta,kl,kr,kt,kb,autot
0,0.3,300.0 <==npack,con,dmpdt
0.01,0 <==dtmax,div
1.0d-8,0.39 <==erriccg,fcvlim,nrestart
1.0e-02,.false. <==gfctn,frctn,conserve
3000,true. <==cray,itmxiccg,sym
$end
$fldparam
1.0e-06,0,0,0,-9.8,0,0,0.0 <==xnu,icyl,gx,gy,ui,vi
0.0d0, 1.0 <==utop,psat,rhof
0.,0.,0.,0.,0.,0.,0.,0. <==uinf(1:4),vinf(1:4)
0.0,0.0,0.0,0.0 <==pbc(1:4)
$end
$mesh
3,0,0,10,0,24.2,30.0,5.0,24.175,27.1,100,379,116,100,1,116
0.05,0.025,0.025
2,0,0,0.36,0.936,0.354,0.648,33,48,1,48
0.006,0.006
$end
$obstcl
2 <==nobstype
2
0., 0., -0.02857143, -1.0, 0., 0., 1., 0.
0., 0., 0.330857, 24.475, 1,0
0., 0., 0., 0.,0.,0.,0.,0.
0., 0., 0., 0.,0.,0.,0.,0.
2
0., 0., -0.1, 1.0, 0., 0., 1., 0.
0., 0., 2.07514, -24.4225, 1,0
0., 0., 0., 0.,0.,0.,0.,0.
0., 0., 0., 0.,0.,0.,0.,0.
$end
$fre surf
0 <==nfrsurf
$end
$wave parameter$
0.1138,0.6,4 <==aa,h0,ncenter
2.0,1
$output format$
0.0,100.0,1,814,1,132,1,1,1,1,0 <==ts,tf,ib,ie,jb,je,ix,iy,lout,nanim,nmean
17,6.0,11.32,20.0,24.851,25.331,25.541,25.711,25.911,26.131,26.271,26.461,26.681,26.861,26.901,27.031,27
.221,27.391,0.0,500.0,0.02
0.0,500.0,0.2 <==tstart_a,tfinish_a,predt_a
$porous material information$
0 <==npor
$turbulence model information$
4 <==kemodel
0.5,1e-6,1 <==ticf,eddycoef

```

\$boundary type\$  
0,0,0,1,0 <==nweakref,nopen,islip  
0.0022,2.0  
\$sponge layer\$  
0 <==nsponge  
\$free surface tracking method\$  
1 <==nfree  
\$pollutant transport parameter\$  
0  
\$restart controlling parameter\$  
0 <==nrs  
\$overtopping calculation\$  
0 <==0:no calculation

**RBREAK2 using the modified input**

```

3          --> NLINES
-----
RUN RN3: SPECIFY TOTAL WAVE
-----
20          --> IJOB,ISTAB
1           --> ISYST
1           --> IBOT
1           --> INONCT
1           --> IENERG
3  0  etaexp --> IWAVE,MSTAT,FINP2
1  1  200  100 --> ISAVA,MSAVA1,MSAVA2,NTIMES
1  15          --> ISAVB,NNODB
0  0          --> ISAVC,NNODC
00000  0      --> IREQ,IELEV,IV,IDUDT,ISNR,NNREQ
  200        --> INITS
    1        --> MULTIF
      .003000 --> DELTA (NORMALIZED)
    200.000000 --> TMAX (NORMALIZED)
    100        --> NRATE
      1        --> NDELRL
    1.000000   --> DELRP(1) (MILLIMETERS)
    2.000000  2.000000 --> X1,X2
    0.107440  2.000000 --> HREFP(METERS),TP(SECONDS)
    1.000000  1.000000 --> KSREF,KSSEA
    0.600000   --> DSEAP(METERS)
    0.100000   --> TSLOPS
      1        --> NBSEG
    8.500000  0.100000  0.010000 --> WBSEG(1),TBSLOP(1),FWP(1)
138 154 161 166 173 --> NODB(1)-(2)-(3)-(4)-(5)
180 185 191 194 199 --> NODB(1)-(2)-(3)-(4)-(5)
205 206 210 217 222 --> NODB(1)-(2)-(3)-(4)-(5)

```

**FUNWAVE1D using the modified input (funwave1d.data)**

```
$data1
ibe = 2
imch = 4
ianm = 0
a0 = 0.0569
h0 = 0.6
tpd = 2.0
dx = 0.04
dt = 0.01
mx = 1250
nt = 8192
itbgn = 1000
itend = 8000
itdel = 10
itscr = 100
itftr = 500
cbkv = 0.55
ck_bt = 0.01
delta = 0.002
slmda = 80.
isltb = 1000
islte = 1250
$end
```

```
$data2
isrc = 1000
swidth = 1.0
cspg = 10.0
cspg2 = 0.0
cspg3 = 0.0
ispg = 400 51
ngage = 21
ixg = 1000 1060 1070 1080 1090
      1102 1114 1119 1124 1129
      1134 1138 1142 1145 1148
      1152 1153 1157 1161 1166 1170
itg = 2000 2010 2020 2030 2040 2050 2060 2070 2080 2090 2100 2110
$end
```

```
$data3
f1n = 'sw_depth2.dat'
f2n = 'initw.data'
f3n = 'random1d.mk'
f4n = 'etats.out'
f5n = 'tmp.out'
f6n = 'etaxs.out'
f7n = 'etaxt.out'
f9n = 'eddy.out'
$end
```

```
$data4
itide = 0
tideco = 0 0.0 0.0
$end
```

**COBRAS using the modified input.**

- kemodel =4 (the nonlinear eddy viscosity model)

- kemodel =6 (the RNG model)

```

$numparam
0.005,200.1,60.2,0.02 <==delt,twfin,prtdt,pltdt
0.3,1.0,6,1,1,1,1.0 <==alpha,beta,kl,kr,kt,kb,autot
0,0.3,300.0 <==npack,con,dmpdt
0.01,0 <==dtmax,ivid
1.0e-8,0.39 <==erriccg,fcvlim,nrestart
1.0e-02,.false. <==gfctn,frctn,conserve
3000,.true. <==cray,itmxiccg,sym
$end
$fldparam
1.0e-06,0,0,0,-9.8,0,0,0.0 <==xnu,icyl,gx,gy,ui,vi
0.0d0, 1.0 <==utop,psat,rhof
0.,0.,0.,0.,0.,0.,0.,0. <==uinf(1:4),vinf(1:4)
0.0,0.0,0.0,0.0 <==pbc(1:4)
$end
$mesh
3,0.0,15.0,29.2,35.0,7.5,29.175,32.1,150,379,116,150,1,116
0.05,0.025,0.025
2,0.0,0.36,0.936,0.354,0.648,33,48,1,48
0.006,0.006
$end
$obstcl
1 <==nobstype
2
0., 0., -0.1, -1.0, 0., 0., 1.,0.
0., 0., 2.575, 35, 1,0
0., 0., 0., 0.,0.,0.,0.,0.
0., 0., 0., 0.,0.,0.,0.,0.
$end
$fre surf
0 <==nfrsurf
$end
$wave parameter$
0.10744,0.6,4 <==aa,h0,ncenter
2.0,1
$output format$
0.0,100.0,1,914,1,132,1,1,1,1,0 <==ts,tf,ib,ie,jb,je,ix,iy,lout,nanim,nmean
19,11.0,25.0,29.551,29.651,29.751,29.851,30.331,30.541,30.711,30.911,31.131,31.271,31.461,31.681,31.861,
31.901,32.031,32.221,32.391,0.0,200.0,0.02
0.0,200.0,0.2 <==tstart_a,tfinish_a,pre dt_a
$porous material information$
0 <==npor
$turbulence model information$
6 <==kemodel
0.5,1e-6,1 <==ticf,eddycoef
$boundary type$
0,0,0,1,0 <==nweakref,nopen,islip
0.0022,2.0
$sponge layer$
0 <==nsponge

```

\$free surface tracking method\$  
1 <==nfree  
\$pollutant transport parameter\$  
0  
\$restart controlling parameter\$  
0 <==nrs  
\$overtopping calculation\$  
0 <==0:no calculation